ABSTRACT

Title of Dissertation: ELECTROHYDRODYNAMICS (EHD) PUMPING OF LIQUID NITROGEN – APPLICATION TO SPOT CRYOGENIC COOLING OF SENSORS AND DETECTORS

Mihai Rada, Doctor of Philosophy, 2004

Dissertation directed by: Professor Michael M. Ohadi
Department of Mechanical Engineering

Superconducting electronics require cryogenic conditions as well as certain conventional electronic applications exhibit better performance at low temperatures. A cryogenic operating environment ensures increased operating speeds and improves the signal-to-noise ratio and the bandwidth of analog devices and sensors, while also ensuring reduced aging effect. Most of these applications require modest power dissipation capabilities while having stricter requirements on the spatial and temporal temperature variations. Controlled surface cooling techniques ensure more stable and uniform temporal and spatial temperature distributions that allow better signal-to-noise ratios for sensors and elimination of hot spots for processors. EHD pumping is a promising technique that could provide pumping and mass flow rate control along the cooled surface. In this work, an ion-drag EHD pump is used to provide the pumping power necessary to ensure the cooling requirements.

The present study contributes to two major areas which could provide significant improvement in electronics cooling applications. One direction concerns development of an EHD micropump, which could provide the pumping power for micro-cooling systems capable of providing more efficient and localized cooling. Using a 3M fluid, a micropump with a 50 μm gap between the emitter and collector and a saw-tooth emitter configuration at an applied voltage of about 250 V provided a pumping head of 650 Pa. For a more optimized design a combination of saw tooth emitters and a 3-D solder-bump structure should be used.

The other major contribution involves the application, for the first time, of the EHD pumping technique to cryogenic liquids. Successful implementation of these cooling techniques could provide on-demand and on-location pumping power which would allow tight cryogenic temperature control on the cooling surface of sensors, detectors and other cold electronics. Pumping heads of up to 1 Pa with mass flow rates of 0.8 g/s were achieved using liquid nitrogen. Although the pressure head results seem relatively small, the corresponding liquid nitrogen mass flow rate meets the targeted heat removal requirements specific to superconducting sensors and detectors.

ELECTROHYDRODYNAMICS (EHD) PUMPING OF LIQUID NITROGEN – APPLICATION TO SPOT CRYOGENIC COOLING OF SENSORS AND DETECTORS

by

Mihai Rada

Dissertation submitted to the Faculty of the Graduate School of The University of Maryland at College Park in partial fulfillment of the requirements for the degree of Doctor of Philosophy
2004

Advisory Committee:

Professor Michael M. Ohadi, Chair/Advisor
Associate Professor Jungho Kim
Professor Marino di Marzo
Associate Professor Gary Pertmer
Assistant Professor Elisabeth Smela

DEDICATION

To my wonderful parents and to my beautiful wife with love

ACKNOWLEDGEMENTS

I would like to express my indebtedness to my advisor, Dr. Michael Ohadi, for the unique opportunities he offered me, for his guidance, and support throughout the course of my studies. I would also like to thank Dr. Jeff Darabi, for his invaluable assistance and interaction during the EHD micropumping work and to Mario Martins and Jeff Didion from NASA GSFC for their valuable support and assistance during the experimental work performed on liquid nitrogen EHD pumping.

My thanks are due to the members of the advisory committee, Dr. Jungho Kim, Dr. Marino di Marzo, Dr. Gary Pertmer, and Dr. Elisabeth Smela for providing constructive suggestions and guidance.

I wish to thank my good friends and colleagues from Small and Smart Thermal Systems Laboratory.

I would like to acknowledge the support of the TRW Corp. which produced the micropumping devices presented in this work and especially thank Dr. John Lawler.

I would like to thank Bernie LaFrance and Tony McNair for their invaluable work and ideas put in building the EHD meso-pump loop.

I was honored to receive the friendship of the Thermal Engineering Branch group at NASA GSFC where during the years 2001-2002 I performed my cryogenic experimental work. My thanks go to Jim Dye, Pat Gonzalez, Dan Butler, George and Mark, Alice and Ron Rector.

I am also indebted to Alexandru Bologa with whom I had very fruitful discussions.

A special mention for my father whose dreams finally came true.

TABLE OF CONTENTS

LIST OF FIGURES

LIST OF TABLES

LIST OF ABBREVIATIONS

AD	analog – digital
CAD	computer aided design
DA	digital - analog
DC	direct current
EHD	electrohydrodynamic
IR	infra-red
HTS	high temperature semiconductors
LAr	liquid argon
LN2	liquid nitrogen
PTFE	polytetrafluoroethylene
r.m.s.	root mean square
SQUID	superconducting quantum interference device

NOMENCLATURE

A	non-dimensional parameter
A_c	collector area [m^2]
a	radius of the charged core [m]
C	charge injection level – non-dimensional parameter
d	electrode gap [m]
D	loop pipe diameter [m]
e	electron charge [C]
$\vec{E}$	electric field [V/m]
E_{val}	valence band energy level [eV]
F_V	characteristic field strength [V/m]
$\vec{f}_C$	Coulomb force density [N/m^3]
$\vec{f}_d$	dielectric force due to a permittivity gradient inside the medium [N/m^3]
$\vec{f}_e$	EHD body force [N/m^3]
g	gravitational constant [9.8 m/s^2]
h	hydrostatic height [m]
I	electric current [A]
$I_{L,}$ I_{liq}	liquid ionization energy [eV]
I_{gas}	gas ionization energy [eV]
$\vec{i}$	unit normal vector [m]
j	current density [A/m^2]
K	ion mobility [m^2/sV]
L	loop length [m]
$\dot{m}$	mass flow rate [kg/s]
M	mobility parameter – non-dimensional parameter
N	number density [$1/m^3$]
Ne	electric Nusselt number – non-dimensional parameter
p_1,p	hydrostatic pressure [Pa]
P_+	polarization energy [eV]
q	volume (or surface) charge density [C/m^3]
q_e and q_i	elastic and inelastic scattering cross-sections [m^2]
r_0, r_p	tip radius of curvature [m]
Re	Reynolds number
R_e	electric Reynolds number – non-dimensional parameter
t	time [s]
T	instability parameter – non-dimensional parameter
U	convective velocity [m/s]
U_s	threshold voltage [V]
$\vec{u}$	velocity field [m/s]
v_{th}	thermal velocity [m/s]
V	voltage [V]
w	velocity component perpendicular to the electrodes [m/s]
W	electron drift velocity [m/s]

W_f	velocity of free electrons [m/s]
W_s	slow electron velocity [m/s]
X	molar percentage of N_2 [mol%]
z_g	charge layer thickness [m]

Greek symbols

α_L	ionization coefficient [1/m]
ε	dielectric permittivity [F/m]
ε_0	vacuum electric permittivity [F/m]
ε_r	dielectric constant
ϕ	electric potential [V]
ρ	mass density [kg/m^3]
σ	electric conductivity [S]
η	dynamic viscosity [Ns/m^2]
ν	kinematic viscosity [m^2/s]
Φ	work function [eV]

Superscripts

*	non-dimensional quantities
_	reduced average value

Subscripts

0	initial value
c	critical value
e	electric
f	free electron
FN	Fowler – Nordheim
g	gas
l	liquid
s	saturation value
t	trapped (localized) electron
T	threshold value above which turbulent flow sets in
th	threshold value for which motion sets in
vac	vacuum
z	z direction

CHAPTER 1 INTRODUCTION

1.1 BACKGROUND

Superconducting electronics require cryogenic temperatures and certain conventional electronic applications exhibit better performance at low temperatures (ter Barke, 1996). A cryogenic operating environment ensures increased operating speeds and improves the signal-to-noise ratio and the bandwidth of analog devices and sensors, while also ensuring reduced aging effect (Holland, 1998). Cold electronic applications are found in computers, amplifiers, mixers, fast AD and DA converters, power cable systems, and transformers using high temperature superconducting (HTS) materials, IR detectors, and SQUID magnetometers. Most of these applications require modest power dissipation capabilities while having stricter requirements on the spatial and temporal temperature variations. Controlled surface cooling techniques ensure more stable and uniform temporal and spatial temperature distributions that allow better signal-to-noise ratios for sensors and elimination of hot spots for processors. EHD pumping is a promising technique that could provide mass flow rate control along the cooled surface. In this work, an ion-drag EHD pump is used to provide the pumping power necessary to deliver the cooling load.

The present study presents two research contributions in areas which could provide significant improvement in electronics cooling applications. The first direction concerns development of an EHD micropump, which could provide the pumping power for micro-cooling systems capable of providing more efficient and localized cooling. The second major contribution involves the application for the first time of the EHD pumping technique to cryogenic liquids. Some of the main advantages in applying EHD pumping

to a cryogenic cooling system are controllable mass flow rates, which allow better control of the cooling capacity, and smaller and mobile cooling devices with very low energy consumptions. Successful implementation of these cooling techniques could provide on-demand and on-location pumping power which would allow tight cryogenic temperature control on the cooling surface for sensors, processors and cold electronics.

In dielectric liquids, when a strong enough voltage is applied between two electrodes, usually called the emitter and collector, ions are generated in the region of highest electric field in the immediate vicinity of the emitter (Atten, 1996). These ions move under the Coulomb force's action towards the electrode with opposite polarity to the collector, dragging the neutral molecules and thus causing movement of the bulk fluid. This movement is basically a pumping action, called ion-drag pumping. Though this mechanism has been understood for a long time (Stuetzer, 1959 and Pickard, 1963), only in the recent decade has it generated considerable interest for real world applications. Among the advantages of an EHD pumping system are its lack of moving parts (no wear or contamination due to lubrication), its controllability (pumping output can be controlled by the voltage applied), and its small power requirement (on the order of milliwatts). A potential application for EHD pumping, explored in this study, is the pumping of cryogenic dielectric liquids, which are widely used for the cooling of cold electronic devices.

1.2 RESEARCH OBJECTIVES

The present work aims to characterize experimentally and to analyze the feasibility of the EHD pumping technique for cryogenic liquids. It presents also the feasibility study of an

EHD micropump by determining its characteristics and the main design features effect on its pumping performance. More specifically, the major objectives include:

- Investigating the feasibility of a novel ion-drag electrohydrodynamic (EHD) micropump and determining ways to improve EHD pumping capability of the micropump using different emitter designs which try to maximize the electric field gradients between the electrodes;
- Investigating the feasibility of applying the EHD pumping technique to cryogenic liquids by developing a new meso-scale EHD pump designed to provide cryogenic liquid pumping capability.
- Developing a numerical modeling and simulation to further understand and predict the pumping phenomenon, which will allow us to find ways to improve the pumping performance by better EHD pump design.

1.2.1 Microscale EHD Pumping

EHD micropumps have been investigated by a number of researchers over the past decade (Bart et al., 1990; Richter et al., 1991; Fuhr et al., 1992; Fuhr et al., 1994; Cho and Kim, 1995; and Ahn and Kim, 1997). Richter et al. (1991) proposed one of the first ion-drag EHD micropumps consisting of two parallel grids obtained from micromachined silicon substrates, anodically bonded. The grids were 3 mm × 3 mm in size, consisting of 70 or 140 μm through-holes in 380 μm thick silicon wafers. The results were promising, showing a maximum pressure of 2500 Pa with a maximum flow rate of 14 ml/min with ethanol at an applied voltage of 700 volts. Fuhr et al. (1992 and 1994) and Cho and Kim (1995) used a traveling electrical wave to drive the fluid along the pumping channel. Ahn and Kim (1997) proposed a microscale ion drag pump with planar electrodes with

electrode spacing of 100 μm and which at 100 V provided up to 250 Pa in static pumping tests.

This work provides a more in-depth understanding of the EHD micropumping mechanism and characteristics by analyzing a set of designs which try to maximize the pumping performance. The parametric study we have undertaken provides some solutions for the design of an optimum EHD micropump.

1.2.2 Meso-scale Cryogenic EHD Pumping

The need for a means of providing local and controllable pumping capability is felt in various special HTS applications such as sensors and transmission/reception equipment and in many other cold electronic devices. As mentioned earlier, EHD pumping is a pumping technique that provides local and controllable pumping capabilities with very low power consumption and noise.

The interest in developing EHD pumping applications has risen in the past few decades when a number of published papers treated the design and characteristics of EHD pumps which could be employed in cooling, flow management, or other pumping applications. All these solutions address the application of the EHD pumping technique, presenting pump designs and pumping performance characteristics using room temperature liquids. No previous work to our knowledge has explored the possibility of applying the EHD pumping technique to cryogenic liquids pumping. Still, the need for a cryogenic EHD pump exists, and hence the work presented here addresses this unexplored area.

1.3 SCOPE

Fundamentals of the EHD pumping mechanism and basic equations and characterizing parameters are presented in Chapter 2. Chapter 3 provides a comprehensive literature

review on the electric processes that take place when electric fields are applied to dielectric liquids; this review is followed by a particularization of the cryogenic liquid's characteristics and behavior. The design, fabrication, and experimental testing of the different novel EHD micropump designs are presented in Chapter 4. The design, fabrication, and testing of the vertical and loop configurations using room temperature liquids of a meso-scale EHD pump are covered in Chapter 5. The meso-scale pump tests with liquid nitrogen, including the test facility and procedure, experimental results, and analysis are presented in Chapter 6. Chapter 7 deals with the numerical simulations of the cryogenic EHD pump. The results of a parametric study undertaken to allow determinations of an optimum cryogenic EHD pump design are presented also in Chapter 7. Chapter 8 compiles the numerical and the experimental results, comparing and analyzing them. The determination of a pumping curve for liquid nitrogen using the proposed system is presented, which represents a useful tool for designing a cryogenic cooling system using the proposed EHD pump. The last chapter presents the conclusions and recommended future work.

CHAPTER 2 FUNDAMENTALS OF ION-DRAG ELECTROHYDRODYNAMIC (EHD) PUMPING

2.1 INTRODUCTION

Electrohydrodynamic (EHD) pumping is a new and promising technique that has demonstrated potential for significantly reducing the volume-to-pumping-capability ratio of heat/mass transfer devices while providing on-line/on-demand control for the heat/mass transfer. The main objective of this chapter is to present the fundamentals of ion-drag EHD pumping and to review previous work in this field. EHD pumping has applications in enhancement of momentum and energy exchange in the single-phase and phase-change processes of significance to the energy conversion, refrigeration, power, and process industries. In this chapter, the fundamental equations governing the EHD body force are first introduced followed by a summary of the EHD pumping characteristics. Next, a representative literature review provides an analysis of the recent research and developments in EHD pumping.

2.2 ION-DRAG EHD PUMPING FUNDAMENTALS

Electrohydrodynamics is a particular domain of the electrodynamics of moving media concerned with the action of electric forces on dielectric media. The dielectric fluids exhibit very low electrical conductivity and thus can sustain very high fields with small currents and thus negligible power consumption and/or induced magnetic fields.

Disregarding the polarization forces, there are two types of forces that can produce motion in a fluid medium upon applying an electric field (Atten (1996)): the Coulomb

force, which acts on the volume (or surface) charge q, under the electric field $\vec{E}$ and is given by:

$$\vec{f}_C = q\vec{E} \tag{2.1}$$

and the dielectric force due to a permittivity gradient $\nabla\varepsilon$ inside the medium expressed as:

$$\vec{f}_d = -(E^2/2)\nabla\varepsilon \tag{2.2}$$

which appears at the liquid-gas interfaces.

Between these two forces, the more important one in ion-drag EHD pumping is the Coulomb force, which acts on the charges generated in a fluid by one of the following means: bulk charge due to weak conductivity of the dielectric fluid (conduction current), ion injection at the electrodes by electrochemical reactions at low field intensities, or electronic charge generation at high fields or by field enhanced dissociation (injection current). Gradients of conductivity (in general due to temperature) could also produce space charges. The most important charge generation process in liquids is the charge injection at the electrode/liquid interface. The ions generated at the electrodes are of the same polarity as the electrode. In liquids of high enough resistivity, the injection current dominates over the conduction current. In gases, the process by which charges are released in the fluid under high electric fields is known as the corona effect and occurs at the sharp tip of the electrodes. For liquids in the electrode regions where the curvature is very high (as on a needle tip, blade, or thin wire), the electric field can reach values high enough to produce, in most of the cases, an electronic injection rather than an electrochemical ion generation.

Let us consider a parallel plates electrode system. At the electroquasistatics (Melcher, 1981) limit when the magnetic field is ignored, the Maxwell equations are:

$$\nabla \times \vec{E} = 0$$
$$\nabla \cdot \vec{E} = \frac{q}{\varepsilon} \tag{2.3}$$
$$\frac{\partial q}{\partial t} + \nabla \cdot \vec{j} = 0$$

where $\vec{E}$ is the electric field, q and $\vec{j}$ are the charge density and current density, and ε is the fluid permittivity. The above equations are formulated with the assumption that the ohmic current is larger than the displacement current, and they state the following: the electric field intensity is irrotational and thus can be derived from the gradient of a scalar function, which is the electric potential ($\vec{E} = \nabla\phi$). The divergence of the electric field is due to the charges present in the control volume, and charge is conserved in the control volume. Neglecting diffusion, a constitutive law for the current density for unipolar injection in a perfectly insulating liquid (thus its conductivity $\sigma = 0$) is given by:

$$\vec{j} = qK\vec{E} + q\vec{u} \tag{2.4}$$

where K is the ion mobility and $\vec{u}$ the velocity field.

The two components in the current density expression are the conduction current density, $Kq\vec{E}$, due to the ion drift with respect to the fluid, and the convective term, $q\vec{u}$, due to the charge transport due to the fluid velocity.

The Navier-Stokes equations for an incompressible and isothermal fluid are:

$$\nabla \cdot \vec{u} = 0$$
$$\rho\left(\frac{\partial \vec{u}}{\partial t} + \vec{u} \cdot \nabla \vec{u}\right) = -\nabla p_1 + \eta \nabla^2 \vec{u} - qg\vec{i}_z + \vec{f}_e \tag{2.5}$$

where ρ is the fluid mass density, p_1 is the pressure, η the dynamic viscosity, $\vec{i}_z$ the vertical unit vector and $\vec{f}_e$ the density of electric force which has the expression (Melcher 1981):

$$\vec{f}_e = q\vec{E} - \frac{E^2}{2}\nabla\varepsilon + \nabla\left(\frac{E^2}{2}\rho\frac{\partial\varepsilon}{\partial\rho}\right) \tag{2.6}$$

For an isothermal and homogeneous fluid, $\nabla\varepsilon = 0$; then, the second term vanishes.

Including all the gravitational and electrostriction effects in the pressure term we obtain:

$$\rho\left(\frac{\partial\vec{u}}{\partial t} + \vec{u}\cdot\nabla\vec{u}\right) = -\nabla p + \eta\nabla^2\vec{u} + q\vec{E} \tag{2.7}$$

A common non-dimensionalization equation uses the electrode gap d, the applied voltage V, the ion mobility K and the electric permittivity ε. Thus we have:

- non-dimensional electric potential: $\phi^* = \frac{\phi}{V}$
- non-dimensional velocity: $V^* = \frac{KV}{d}$
- non-dimensional pressure: $p^* = \frac{\rho K^2 V^2}{d^2}$
- non-dimensional time: $t^* = \frac{d^2}{KV}$
- non-dimensional charge density: $q^* = \frac{\varepsilon V}{d^2}$
- non-dimensional current density: $j^* = \frac{K\varepsilon V^2}{d^3}$

The non-dimensional EHD flow system is given by:

$$\begin{aligned}
&\vec{E}^* = -\nabla\phi^* \\
&\nabla\vec{E}^* = q^* \\
&\frac{\partial q^*}{\partial t^*} + \nabla\vec{j}^* = 0 \\
&\nabla\cdot\vec{u}^* = 0 \\
&R_e\left(\frac{\partial\vec{u}^*}{\partial t^*} + \vec{u}^*\cdot\nabla\vec{u}^*\right) = -R_e\nabla p^* + \nabla^2\vec{u}^* + Tq^*\vec{E}^* \\
&\vec{j}^* = q^*(\vec{E}^* + \vec{u}^*)
\end{aligned} \tag{2.8}$$

The following non-dimensional parameters are introduced:

- electric Reynolds number: $R_e = \frac{KV}{\nu}$
- instability parameter: $T = \frac{\varepsilon V}{K\eta}$
- mobility parameter: $M = \frac{(\varepsilon/\rho)^{1/2}}{K}$

The parallel plate EHD flow problem is similar to a horizontal heated plate natural convection problem. The electric Reynolds number is the correspondent of the Reynolds number from the heat transfer problem but formed using the typical ion drift mobility. The parameter T characterizes the instability of the flow and represents the ratio of the driving Coulomb force and the damping viscous force. Also for liquids, T ~ V, since according to Walden's rule (Schmidt, 1997), $K\eta$ ~ constant. Above a certain value of T the EHD flow sets in. The mobility parameter M formed from the ratio of the hydrodynamic mobility over the true mobility plays the role of a Prandtl number, giving us: $T = M^2 R_e$.

The typical boundary conditions for the EHD flow system consist of imposing the electric potential on the electrodes and the charge density q_0 on the emitter for the electrical problem and the non-slip condition for the flow problem. Usually a uniform emitter charge density is assumed.

Thus we have $\phi = V;\ q = q_0;\ \vec{u} = 0$ on the emitter and $\phi = 0;\ \vec{u} = 0$ on the collector.

Let us introduce a non-dimensional number to characterize the charge injection level:

$$C = \frac{q_0 d^2}{\varepsilon V} \tag{2.9}$$

where d is the electrode gap.

2.2.1 Parallel Plane Geometry

The study of EHD electroconvection in a plane parallel configuration allows us to understand better the characteristics of EHD pumping. This section presents a discussion on the different current and flow characteristics possible to obtain in an EHD pumping system.

Depending on the charge injection level characterized by C, two regimes are reported by Lacroix (1975) for the planar geometry electroconvection. One is characterized by $C<<1$ when the processes occurring at the metal/liquid interface limit the amount of charge injected. This case corresponds to a weak injection, and a very weak distortion of the electric field is observed. The weak injection limit is characterized as $T_c C^2 = 220.7$ where T_c is the critical value of T, which has a value $T_c \sim 100$ (experimental) to 161 (theoretical) (Atten 1996). In the other case, the charge injection is limited only by the ability of the system to transport it, meaning that the current depends on the convective velocity. In this case $C>>1$, and as C tends to infinity, T_c tends to 161. This regime is called space charge limited injection and is usually characterized by the current being proportional to the square of the voltage: $I \sim V^2$.

Lacroix and Atten (1975) analyzed the influence of induced motion on unipolar charge transport. They studied the conditions under which instability sets in - that is, when the liquid cannot remain at rest - and the influence of induced motion on charge transport. They used the non-dimensional number T to characterize the instability. When T exceeds certain value instability occurs. They used the case of stationary state space-charge limited unipolar injection in a parallel plates cell. When the fluid was stationary the Coulomb force was uniform. The electric Nusselt number Ne (analogous to Nusselt

number in a heated horizontal plate) was defined as the ratio of the effective current I to the space-charge limited current (SCLC) I_0 which would set in if there were no motion. It was found that the Ne has a saturation value at high voltages.

Assuming that diffusion is negligible and that the liquid is a perfect insulator, two states can be distinguished: viscosity dominated flow and a fully developed turbulent regime.

For the first case, when low voltages are used a quasi-cellular laminar motion is observed. In the space between the electrodes two regions are identified: a layer close to the injector where the drift transport dominates and the core region where the convective transport is dominant. Let us introduce a number A as:

$$A = \frac{\max|w| \cdot d}{K \cdot V} \tag{2.10}$$

where w is the velocity component perpendicular to the electrodes and d is the electrode gap. Based on a force balance, A ~ T such that Ne ~ $T^{1/2}$. Since Ne=1 for $T<T_c$ (the critical T below which no motion set in), it can be obtained that Ne ~ $(T/T_c)^{1/2}$ for $T>T_c$.

For high voltages, a boundary layer with a strong gradient of mean charge of thickness z_g is obtained. Far from the metal/liquid interface a core of weak mean charge gradient is observed. Based on an energy balance the root mean square (r.m.s.) value of the reduced fluid velocity $w' = (\overline{w^2})^{1/2}$ varies as $M\bar{E}(z_g)$ where $M = (\varepsilon/\rho)^{1/2}/K$, with ρ the density of the fluid and $\bar{E}$ the mean reduced value of E.

Ne can be expressed as:

$$Ne \sim \bar{q}(1-\bar{q}/2)(1+\beta M^{1/2}) \tag{2.11}$$

For a maximum charge dissipation, it can be assumed that $\bar{q}=1$, and β is a constant of order 1. Thus, if M is high enough Ne no longer depends on the voltage, which predicts a

saturation of the Ne and r.m.s. of the reduced fluid velocity at high enough voltages. The transition region marks the change from the viscous flow to a non-linear one. Using the analogy with the heat transfer problem, we get T_c=90 for a R_e = 10 which is the critical Re in the heat transfer problem.

Lacroix (1975) identified experimentally three stages of charge transport. For applied voltages lower than a critical value V_c (V_c=50V for pyralene 1460 with ε = 5.9, η=10cp at 20 °C) the current varies as $I \sim V^2/d^3$, and no motion is detected. For voltages above V_c, I varies as $I \sim V^{5/2}/d^3$, and a stable quasi-laminar flow is obtained with a velocity characterized by the non-dimensional parameter $A = T/T_c = V/V_c$. For applied voltages above V_T (threshold voltage) (V_T = 1000V for pyralene 1460), $I \sim V^2/d^3$ and a turbulent motion is obtained in the parallel plane geometry. The T_c has been confirmed experimentally for 8 different liquids to be between 80 and 90. The saturation value for the electric Nusselt number is $Ne_s = \sqrt{M/3}$.

A limiting value for M=3 is obtained from the limiting value of T_c. Based on this limiting value two types of fluids can be distinguished.

Fluids with low permittivity and viscosity, for which M<3, among which are the gases and a few liquids, exhibit an induced fluid velocity lower than the ionic velocity, and thus the convection has a negligible effect on the charge transfer and the electric field distribution. As the voltage exceeds the critical value, these fluids are expected to pass to the turbulent regime for a parallel plates configuration.

The other classes of fluid consist of most of the fluids for which M>3. The induced motion plays the major role in charge transport, and the convective velocity takes values

higher than the ionic one. For these fluids the motion strongly affects the charge and field distributions that exist at rest.

These considerations allow us to conclude that in the numerical simulations decoupling the electric and flow problem, in the case of liquids, could be a valid assumption.

2.2.2 Asymmetric Geometry

For asymmetric geometries (point-plane, blade-plane, etc.), moderate or strong injections arise from the high field locations. The charge distribution on the injector has a strong character of non-uniformity, producing highly non-uniform charge density distributions in the bulk. In this case the flow organizes in plumes starting from the tip to the plane. For a liquid with a high enough M value, the ion drift is lower than the liquid velocity, and the ions are entrained by the flow they produce. For this case the charge is concentrated inside the plume, instead of covering the whole available volume as in the space charge limit assumption, and thus this assumption cannot be used.

Atten (1997) presents a comprehensive analysis of the EHD plumes in a point-plane geometry. In gases the drift velocity induced by the electric field on the charges is much higher than the gas velocity (electric wind), and the charge trajectory follows the field lines. For gases the charge is distributed in a large, almost hemispherical volume in the region between the tip and the plane. In liquids, in a point plane geometry the region in the immediate vicinity of the tip injects ions into the liquid. In the neighborhood of the tip, the Coulomb forces produce velocities much higher than the ion drift velocity with respect to the fluid, due to the action of the strong electric field on the injected charges. Thus, the charge distribution in the region between the electrodes will take a plume shape. The plume is formed in a narrow region around the electrode axis. The current is

found (Atten, 1997) to vary as $I \sim (V - V_{th})^2$ where V is the applied voltage and V_{th} is the threshold voltage for which motion sets in. For transformer oil ($\varepsilon = 2.15$) $V_{th} = 7$ kV, which yields a threshold electric field of about E_{th} 480MV/mm. It is found that this threshold voltage / field varies slightly with the electrode gap d, since it depends very strongly on the tip radius of curvature r_0 according to $E_{th} = \frac{2V_{th}}{r_0 \log(4d/r_0)}$ (Coelho 1971).

In liquids, as in gases, the field on the needle tip is nearly constant as the voltage is increased because the injection law $q = f(E)$ is such that df/dE is very high for $E > E_{th}$.

The mean charge density can be estimated using $I \sim 2\pi r_0^2 K q_0 E_{th}$. For typical I values of 10^{-8} to 10^{-7} A and for the transformer oil under $E_{th} \sim 400$ MV/mm, charge densities of 250-2500 C/m^3 are obtained. These values are very big and support the fact that the Coulomb forces are dominant in the region close to the tip.

The ion velocity is given by

$$\vec{v}_{ion} = K\vec{E} + \vec{U} \qquad (2.12)$$

where the K is the ion mobility, E the electric field, and U the convective velocity. The convective component is dominant inside the plume, while in the immediate vicinity of the tip (closer than 1μm) the ion drift velocity is dominant. Typical Re values of about 400 inside the plume were obtained in experiments. An order of magnitude estimate was done by Atten (1997) for the radius of the charged core *a* when a voltage of 30 kV was applied across a gap of 30 mm in a typical viscous liquid ($\nu \sim 25\times10^{-6}$ m^2/s) which presents a mobility of $K \sim 10^{-9}$ m^2/Vs and shows a current of $I \sim 10^{-7}$ A. The value for *a* was about 75 μm, the velocity inside the plume was 2 m/s, and the plume radius was 400 μm for a typical point to plane geometry.

2.2.3 Summary

Ion-drag pumping relies on the Coulomb force action on the charges injected in the working fluid. The force acting on the charged particles is proportional to the charge density and the strength of the electric field in the region between the electrodes. There are different methods to obtain charged molecules inside the fluid but the most used is ion injection. Ion injection occurs in regions of strong electric field, which are obtained in the needle-shape regions of the emitter. Thus, an ion-drag pump design should have an emitter that provides points as ion injection sites.

A set of three non-dimensional parameters is defined in the literature and is used to describe the EHD ion-drag pumping. R_e is the electric Reynolds number representing the ratio of the electric momentum to the viscous one. R_e characterizes the efficiency of the electric momentum transfer to the fluid. T is the instability parameter and for a space charge limited regime, which is desirable in the case of cryogenic EHD pumping, it tends to a value of about 161 in parallel plates geometry. For an asymmetric geometry, a limit for T exists also which shows that the current and the pumping head are bounded despite increases in the applied voltage. To obtain ion injection in the fluid, the electric field strength should reach values of 300-400 MV/mm, which are possible to obtain in asymmetric geometries with tip radius of curvature of the order of 10-100 μm.

2.3 LITERATURE REVIEW

2.3.1 Meso-scale EHD Pumping

Steutzer published in 1959 “a theory of pressure buildup under unipolar ion conduction.” He derived theoretical relations for the EHD pumping pressure head for parallel plane, cylindrical, and spherical geometries. He showed that the pressure head is proportional to

the electric field strength and the electric permittivity of the fluid corrected by a shape factor to account for the geometrical configuration. Also, he showed that the pressure head is proportional to the current flowing between the two electrodes. For the simplest model, which is plane parallel geometry, we have:

$\frac{dp}{dx} = \rho E$ and using the current density as $j = \rho K E$ we get:

$\frac{dp}{dx} = \frac{j}{K} = \frac{IA_c}{K}$. From which by integration across the gap we get:

$$\Delta P = \frac{I \cdot d}{K A_c}. \tag{2.13}$$

Steutzer showed that by eliminating the charge density between the current density and the Poisson's equation and doing some manipulations we get:

$$\Delta P = \frac{9}{8} \varepsilon E^2 \tag{2.14}$$

where E is the average electric field between the electrodes, ε is the permittivity of the fluid, I is the current flowing between the electrodes, K the charge mobility, d the gap, and A_c the collector area. Steutzer performed a series of experiments to prove the theoretical estimation of the pressure head, using tip emitters and different collector shapes. The maximum pressure head of about 2000 Pa was obtained with castor oil in a tip-to-cylinder geometry.

In his master's thesis, J. E. Bryan (1990) designed different emitter and collector configurations for ion-drag pumping and tested them with different fluids. He used a 10-stage EHD pump. He showed that as more electrodes pairs are powered the pumping performance is improved. He tested dodecylbenzine, Conoco O. S. 260-P industrial oil, kerosene, and Texaco 0600 oil. The best performance was obtained with the

dodecylbenzine at about 20 kV, when a velocity of 15cm/s and a current of 70 μA were obtained.

J. A. Castaneda and J. Seyed Yagoobi (1991) developed an ion drag pump for transformer cooling using R-11. They used thirteen electrode pairs, each pair consisting of two 20-gauge tin-copper wire circles press-fitted in the loop wall. The electrode gap was 8 mm and the stage spacing was 15 mm. They used positive voltage on the emitter. They demonstrated a pressure generation of 40 Pa at 28 kV with a current of 14 μA. The velocity in these conditions was 22 cm/s.

Coletti (1996) presented the results for a series of tests for positive and negative polarity EHD pumping of castor oil, silicone oil, and dodecylbenzine. Their pump design consisted of two-plane parallel electrodes placed inside a 30 mm diameter PMMA case. The emitter was made of a circular, drilled brass, 3 mm thick and 29.5 mm diameter disk, while the collector consisted of a mesh made with 170 μm stainless steel wire. The pumping results showed similar results for the two polarities. The pumping performance was shown to increase with the electrode gap (which varied between 1.5 – 3.5 mm) as the maximum applied voltage was increased. A maximum pressure of about 450 Pa was reached with castor oil at 37 kV, 800 Pa with silicone oil at 37 kV, and about 50 Pa with dodecylbenzine at 22 kV with a gap of 3.5 mm.

Zhakin and Lunev (1999) considered a two-dimensional EHD pumped loop and presented an analytic and numeric solution for the EHD flow. They have used the integral balance method to find the analytic expression of the volumetric flow rate, pressure generation, and efficiency. Based on their estimates, pressure heads of about 300 Pa could be reached using the transformer oil and about 600 Pa using dodecylbenzine,

Sunthene 306, or Conoco. The model did not account for the EHD generated turbulence around the emitter. They found that turbulence decreases the efficiency of EHD pumping. To account for the turbulence, a numerical model was considered. Using this model they showed that the ratio between the channel height and the electrode gap presents a limit value ($h/l = 0.3$), under which the turbulence is eliminated.

Malakhov (1999) has analyzed the reliability of the EHD pumps. He used a two-stage grid type EHD pump to perform operating lifetime tests. He considered the effect of atmospheric impurities and temperature on the operating parameters using kerosene. He concluded that for an initial period, which is in the order of thousands of hours, the operating parameters (pressure head and current) were stable. The effect of the impurities was accounted for by opening the system to the environment. Malakhov concludes that presence of additional impurities from the atmosphere accelerates the sedimentation processes occurring on the electrodes, and also that the fluid properties' variations are accelerated by the exposure to impurities. Variations of the operating conditions are also explained by the presence of electric breakdowns of the fluid. They may produce a temporarily increase of the pumping performance. Malakhov found that electrical discharges and breakdowns could occur continuously during several hours. Once they stopped, the time necessary for the system to reach the initial state was usually 100 to 1000 times higher than the discharges/breakdown period. The liquid temperature was observed to vary synchronously with the operating parameters, which is explained by the density of the volumetric charge and the rate of the electrochemical reaction's dependence on the temperature.

Asano and Yatsuzuka (1999) presented a fundamental study of EHD pumping with needle-cylinder electrodes. They used a silicone fluid and negative polarity (since positive polarity showed no EHD effect) in a parametric test on an EHD pump which had needle emitters and cylindrical holes collector. The maximum static pumping performance was about 300 mm height (2800 Pa). Their design consisted of a 7 μm diameter wire emitter and a tapered hole collector.

Ostapenko and Stishkov (1999) looked into the kinematics and dynamics of EHD flows. They used optical, electronic, and hydrodynamic means to investigate the EHD flow in an experimental cell containing two electrodes with different geometries. The electrodes were made of two copper cylindrical rods whose radius varied from 0.05-20 mm. The electrodes were immersed in a transformed castor oil solution with 10% buthanol. The experiments showed that the thermo-gravitational induced motion has a strength comparable to the one imposed by the EHD effect. They observed that initially, before applying any voltage, weak flows were present in the experimental cell, which were caused by density gradient driven motion. As voltage was applied between the electrodes with a value less than a critical value, the intensity of these flows decreased until they disappeared. If the voltage became higher that the threshold one, an EHD flow pattern was obtained. The kinematics of the flow was analyzed also. At low voltages motion was observed only in the vicinity of the electrodes, but it extended to the whole gap as the voltage was increased. They concluded that mainly laminar flow patterns are encountered, since the typical Reynolds number is around 7. Analyzing the R_e (electrical Reynolds number) variation with the applied voltage, they found a limiting value of about $R_e = 20$, which determines a developed flow region. The fact that the electric Reynolds

number was higher than 1 showed that the velocity of the EHD flow is usually higher than the ion-drift velocity. A smaller electrode radius showed higher R_e numbers. They concluded that the velocity of the EHD flow is proportional to the electrical potential in the liquid layers near the electrodes but is not proportional with the electric field strength. The charge generation rate depends on the electric field strength at the emitter tip, which determines the velocity of the EHD flow.

Their experimental data shows that, in the region between electrodes, Coulomb electric force is almost homogeneous and is weakly dependent on the radius of curvature of the electrode. Typical values of charge generation layer thickness are 10^{-5} cm at voltages of about 1 kV, which yields an electric field strength on the order of 1 GV/mm. The electric field distribution inside the gap is quasi-uniform and has values between 0.1-1 MV/mm. The energy necessary for the dissociation of molecules (formation of pair of ions) is much more than the ionization energy, and the surface ionization of molecules by accepting electrons requires less energy than by release of electrons.

Ohyama, Watson and Chang (2000) and Ueda, Ohyama, Watson and Chang (2001) developed a new type of EHD pump called AW type EHD pump. This pump consists of a wire electrode placed in air above the liquid surface. The liquid (mineral oil) is stored in a tank with a plate wall, which is used as collector. The plate is inclined at an angle of 30 degrees with respect to the horizontal direction. The charges injected by the corona source in the air penetrate the gas–liquid interface and are attracted at the collector. The pumping action causes the liquid to rise along the inclined plate (collector) and to flow over it. Using positive and negative DC voltages of 20-35 kV, volumetric flow rates of

100 ml/min were reached, which correspond to Reynolds numbers of up to 1. The pumping current was in the range of 1 to 16 mA.

2.3.2 Microscale EHD Pumping

Some interesting attempts to build microscale EHD pumps have been made in recent years. In the following, a few of the most representative ones are presented.

Bart et al. (1990) developed a microfabricated EHD pump using a traveling wave. The electrodes were obtained using LPCVD of polycrystalline silicone over an insulating silicone nitride layer. Every third electrode was connected to the same vertical conductor to form two three-phase electrode systems. Silicone oil was used as the working fluid, and a 200 V peak-to-peak voltage was applied as a traveling wave with frequencies of about 1 Hz. A maximum surface velocity of 9 mm/s was reached for the liquid conductivity of about 5×10^{-8} S/m with a fluid depth of 20 μm.

Richter et al. (1991) proposed a microscale pump and a flow measurement device using EHD. He used anisotropic etching to pattern each grid electrode on a silicone substrate. Then, he anodically bonded the substrates to form a pumping stage with electrode spacings between 10-60 μm. The electrodes were gold-coated on opposing surfaces, and ethanol was used as the working fluid. A DC voltage between 0-300 V was applied. At ~ 10 V pumping action was observed. A maximum pressure head of about 1200 Pa was observed at 300 V with the grid electrodes 60 μm apart. Richter also presented a possible flow meter application of the EHD device by correlating the measured current to the liquid flow rate.

Ahn and Kim (1997) fabricated and tested a planar ion-drag micropump. They used 20-130 V DC positive polarity to pump ethyl alcohol. The pump was bi-directional. The

electrodes consisted of 30 stages of striped pairs. The electrode gap was 100 μm and the stage gap 200 μm. The channel width was 3 mm, and the height ~ 100 μm. The electrodes were coated with gold. The maximum mass flow rate demonstrated was about 50 μl/min. The maximum pressure of 225 Pa was obtained at 100 V with a current of around 3 mA.

2.4 ION-DRAG EHD PUMPING RESULTS OVERVIEW

Table 2.1 presents an overview of the EHD pumping data collected from the papers discussed above. The grayed cells represent actual data obtained from the reference while the clear cells are calculated values. The table presents the following electrical and flow parameters:

- *fluid properties*: viscosity and density, electric permittivity, conductivity, and charge mobility;
- *geometric parameters*: tip radius and loop radius, electrode gap, and flow cross-section;
- *electric parameters*: voltage, current, and electric field intensity;
- *flow parameters*: pressure head, velocity, mass flow rate, and volumetric flow rate;
- *non-dimensional parameters*: Reynolds number, electric Reynolds number, the instability parameter (T), mobility (M), and pumping efficiency;
- *system/tests specifications*: loop or static tests, polarity used, working liquid, and type of geometry used in the experiments.

The table is organized in groups of data: the first group (1-4) represents results obtained from theoretical estimations, the second group (5-11) contains static test results, the third

group (12-20) represents loop test results, and the last group contains microscale EHD pumping results.

Static tests are used to determine the maximum pressure head generated by a pump, although they do not provide any information about the mass flow rate. The dynamic (loop) tests provide both pressure head and mass flow rate data, but they are dependent on the loop dynamic pressure losses (given by the loop geometry), thus providing information specific to the tested system.

Typical fluids have viscosities of $3x10^{-7}$ m^2/s with densities of 800-900 kg/m^3, ion mobilities between $7x10^{-10}$ to $1x10^{-8}$ m^2/Vs, and conductivities of 30-1000 nS/m.

The presented references for static tests show that typical EHD pumping voltages range between 17-37 kV at gaps of 3-10 mm, providing pressure heads between 200-2800 Pa. The typical current levels were tens of μA down to nA. For the characteristic non-dimensional numbers, we have the following typical values: electric Reynolds ranges between 0.2-100, $T \sim 3.5\times10^{14} - 7.7\times10^{15}$, $M \sim 2.5\times10^{5} - 1.2\times10^{7}$.

For loop tests, typical voltages of 19-35 kV provide average electric fields of 1-6 MV/m and currents of 3-70 μA. The loop EHD pumping provides pressures from a few Pascals to hundreds of Pascals at mass flow rates ranging from 2-500 g/s, which give Reynolds numbers of 2-1300. The EHD non-dimensional parameters yield values as follows: $R_e \sim$ 1-500, $T \sim 2.5\text{-}3\times10^{15}$ and $M \sim 2\times10^{6}$ - 7×10^{7}.

The microscale tests show pressure heads up to 1200 Pa and volumetric flow rates up to 8.33 ml/s. The electric Reynolds number is between 0.5-3, while T is of the order of 10^{14} and $M \sim 10^{7}$.

Table 2.1 The EHD pumping data overview

No	Reference	Dyn Visc μ [Ns/m^2]	Density ρ [kg/m^3]	Kin Visc ν [m^2/s]	Tip Radius r [μm]	Loop Radius r_l [mm]	Cross Sect. A [m^2]	Charge Mobility K [m^2/Vs]	Electric Field E [MV/m]	Voltage V [V]	Conduct. σ [nS/m]	Current I [A]	Vel. v [m/s]	Relative Electric Permittivity κ
1	Zhakin	7.30E-03	830	8.80E-06		3.5		2.74E-09	0.4	30000				2.5
2	Zhakin	1.53E-01	885	1.73E-04		3.5		1.31E-10	0.4	30000				2.5
3	Zhakin	1.81E-02	906	2.00E-05		3.5		1.10E-09	0.4	30000				2.5
4	Zhakin	5.04E-03	855	5.90E-06		3.5		3.96E-09	0.4	30000				2.2
5	Steutzer	9.50E-01	960	9.90E-04	500	0.5	7.85E-07	2.70E-07	17.0	17000				4.5
6	Coletti	4.62E-02	962	4.80E-05		30	2.83E-03	4.33E-10	10.6	37000				2.3
7	Coletti	9.56E-01	956	1.00E-03		30	2.83E-03	2.09E-11	10.6	37000				4.2
8	Coletti	5.04E-03	855	5.90E-06		30	2.83E-03	3.96E-09	7.1	25000				2.2
9	Asano	4.81E-02	962	5.00E-05	7	13	5.31E-04	4.16E-10	10.0	30000				2.3
10	Ostapenk	1.77E-02	885	2.00E-05	30			1.00E-08	2.5	25000	1.05E+02	2.63E-05		2.5
11	Malakhov	1.74E-03	805	2.16E-06	1000	50	7.85E-03	1.15E-08	6.0	19200	3.26E+02	1.50E-05		2.2
12	Malakhov	1.74E-03	805	2.16E-06	1000	50	7.85E-03	1.15E-08	6.0	19200	3.26E+02	2.00E-05		2.2
13	Krawinkel	2.93E-04	780	3.76E-07				6.80E-08	3.0	2400	5.00E+03	1.92E-09	7.8	21.0
14	Kojevnikov	7.90E-03	885	8.93E-06		1.2	4.52E-06	2.53E-09	1.0	30000	5.00E+01	3.00E-06	2.1	2.5
15	Ohyama	2.85E-02	850	3.35E-05	500	0.5000	2.00E-04	7.02E-10	0.3	35000	5.65E+00	2.30E-05	0.075	
16	Castaneda Yagoobi	4.27E-04	1453	2.94E-07	810	25	1.96E-03	4.68E-08	3.1	25000	8.00E+02	1.20E-05	0.22	
17	Bryan Thesis	8.09E-02	829	9.75E-05		35	3.85E-03	2.47E-10	0.8	20000	1.46E+02	7.00E-05	0.16	2.2
18	Bryan Thesis	2.91E-02	819	3.55E-05		35	3.85E-03	6.88E-10	1.1	27000	9.26E+01	6.00E-05	0.14	2.2
19	Bryan Thesis	1.74E-03	805	2.16E-06		35	3.85E-03	1.15E-08	1.0	23000	2.72E+01	1.50E-05	0.04	2.2
20	Bryan Thesis	1.21E-02	861	1.40E-05		35	3.85E-03	1.65E-09	0.9	22000	1.14E+02	6.00E-05	0.08	2.2
21	Bart	2.70E-03	860	3.14E-06		0.01	1.00E-08	7.41E-09	20.0	200	1.00E+03	2.00E-09	0.009	2.3
22	Richter	1.20E-03	790	1.52E-06			2.53E-05	1.70E-08	5.0	300	1.40E+02	2.52E-09		25.8
23	Ahn	1.20E-03	790	1.52E-06				1.70E-08	0.6	120	1.40E+02	3.50E-03		25.8

Table 2.1 The EHD pumping data overview (cont.)

No.	Pres. Drop DP [Pa]	Mass flow rate m_dot kg/s	Volumetric Flow Q_dot m^3/s	Gap d [mm]	Reynolds Re	Electric Reynolds R	Instability Param T	Mobility Param M	Eff η %	Liquid	Polarity	Obs.
1	290			80			3.75E+15	7.40E-02	81.0	Transformer oil		Plane parallel
2	662			80			3.75E+15	1.07E+00	34.0	Conoco		Plane parallel
3	643			80			3.75E+15	2.07E+00	56.0	Sunthene 306		Plane parallel
4	662			80			3.36E+15	3.07E+00	83.0	Dodecylbenzine		Plane parallel
5	1600			1		4.64	2.98E+11	2.54E+05		Castor oil	Negative	Needle to ring
6	800			3.5		0.33	4.16E+15	1.12E+08		Silicone oil	Negative	Plane parallel
7	500			3.5		0.001	7.77E+15	3.17E+09		Castor oil	Negative	Plane parallel
8	200			3.5		16.80	2.76E+15	1.28E+07		Dodecylbenzine	Negative	Plane parallel
9	2828			3		0.25	3.38E+15	1.16E+08		Silicone oil	Negative	Needle to cylinder
10				10		20.00	3.53E+14	5.31E+06		Transformer oil + 10% buthanol		Parallel wires
11	719			3.2		102.60	2.11E+15	4.54E+06		Kerosene		Wire grid
12	160			3.2		102.60	2.11E+15	4.54E+06		Kerosene		Wire Grid
13				0.8		434.46	2.53E+15	2.41E+06		Acetone		
14	860	1.06E-02	1.20E-05	2	564	8.50	3.75E+15	2.24E+07		Transformer oil + butyl alcohol		Parallel wires
15		2.83E-03	3.33E-06	117	2	1.00				Mineral oil Fisher #19	Negative	AW type EHD pump
16	28	6.28E-01	4.32E-04	8	37415	3981.16				R11	Positive	Needle to ring (13 stages)
17	78	5.11E-01	6.16E-04	24	115	0.05	2.24E+15	6.12E+11	2.5	Dodecylbenzine		Needle to ring (13 stages)
18	59	4.41E-01	5.39E-04	24	276	0.52	2.99E+15	7.56E+07	7.0	Conoco O.S. 260-P		Needle to ring (13 stages)
19	5	1.24E-01	1.54E-04	24	1299	122.90	2.53E+15	4.54E+06	0.1	Kerosene		Needle to ring (13 stages)
20	20	2.65E-01	3.08E-04	24	399	2.59	2.37E+15	3.03E+07	1.5	Texaco 0600		Needle to ring (13 stages)
21		7.74E-08	9.00E-11	0.01	0.029	0.47	2.25E+13	6.91E+06		Silicone oil - Dow Corning 200	AC - 1Hz	Stripes
22	1200			0.0001		3.36	3.79E+14	1.06E+07		Ethanol		Parallel grids
23	100	6.58E-04	8.33E-07	0.0002		1.34	1.52E+14	1.06E+07		Ethyl alcohol	Positive	Stripes

CHAPTER 3 FUNDAMENTAL PHYSICAL PHENOMENA OF APPLYING AN ELECTRIC FIELD TO DIELECTRIC LIQUIDS

3.1 INTRODUCTION

The study of the properties of electrical charges in dielectric liquids has two main applications (Atrazhev, 1991). The first is a practical one concerning the insulating properties of dielectric liquids, since they are employed as insulators in power transformers, transmission cables and others, and the second is a more fundamental one concerning the study of charge carrier generation, transport, and annihilation in liquids. In general, the physical and chemical properties of non-polar liquids, which are mainly liquefied rare gases, liquefied molecular gases, and hydrocarbons, are somewhat similar. They do not have any permanent dipole, and their relative dielectric constant is between 1.05 for helium to about 2.28 for benzene (Schmidt, 1997). Their ionization energies are between 9 and 21 eV and generally exhibit low, fluctuating conductivities depending on the electrode conditions and fluid impurities. In most of these liquids the thermally activated charge carriers produce an immeasurably small concentration of charges, which means that these liquids in their pure state are perfect insulators. Part of the conduction currents observed, is due to the impurities and to cosmic radiation-generated charges.

This chapter presents a literature review of the fundamental electronic phenomena taking place in liquids which are important for the study of the EHD pumping. The fundamentals on the charge generation and behavior in liquids are presented pointing out the characteristics of liquid nitrogen which is the cryogenic liquid of interest in the present work.

3.2 CHARGE GENERATION IN LIQUIDS

Ion-drag EHD pumping relies on the presence of free charges within the liquid. Two categories of charge generation processes can be identified with applying an electric field to a dielectric liquid. One is related to the bulk liquid processes, and another concerns the metal/liquid interface (Lewis, 1994). Within an insulating liquid, charges will arise in the bulk by dissociative ionization of liquid molecules according to a general scheme represented as:

$M \leftrightarrow C^+A^- \leftrightarrow C^+ + A^-$

where C^+A^- is an ion pair complex of a molecule M and C^+ and A^- are the separated cation and anion. Usually when only an electron is split off this will form an anion A^- with another liquid molecule. In this case, a stability criterion should be respected; that is, the electronic energy of the cation state C^+ should be higher than the anion A^- (Lewis, 1994). Still, in the bulk of the liquid the net charge will remain zero even if dissociative processes take place in the liquid, since the number of ion pairs will be equal. A net charge within a liquid under electrical stress can be obtained by charge injection at the electrodes.

Liquid nitrogen molecule dissociation is very weak due to its strong covalent bond. Thus the main charge generation mechanism for liquid nitrogen is due to the electrons injected at the metal/liquid interface.

An electron injected at the electrode can have an energy higher than the conduction band lower limit (given by V_0) (see Figure 3.1) thus being a free electron or become a localized (or attached) electron occupying a free energy level in the valence band of the

molecule. To understand the mechanism governing this behavior a small introduction in liquid electronics is necessary.

The liquid electronic states arise from their individual molecular (or atomic) states. For liquids, similarly to solids, the electronic energy band model can be used (Schmidt, 1991). Upon condensation a shift of the valence band and the formation of a conduction band is observed (Figure 3.1); these bands are separated by energies somewhat higher than 5 eV for non-polar liquids. The ionization energy for liquids (I_l) is defined, as the energy necessary to create an electron/hole pair from a liquid molecule. The energy necessary to extract an electron from the conduction band to vacuum is denoted by V_0 (Schmidt (1991)). In order to determine V_0 for liquids, a method which estimates the shift in the work function of a metal in the liquid (Φ_{liq}) with respect to vacuum (Φ_{vac}) is used, so $V_0 = \Phi_{liq} - \Phi_{vac}$. For some liquids V_0 is positive, which means that energy has to be provided to an electron in vacuum to enter the liquid, or negative, meaning that the electron must receive some energy to leave the liquid. For organic liquids V_0 ranges from –0.7eV for tetramethyl tin to +0.5eV for cyclohexane (Lewis, 1994). Helium has a value of +1.05eV, while the rare gases Ar, Kr or Xe range between –0.2eV to –0.67eV. An energy of V_0 = 0.35eV must be provided to the liquid nitrogen molecule to extract an electron from its conduction band (Lewis, 1994). This energy can be provided by an electric field or by photoexcitation such that ions can be generated.

Within the bulk of the liquid a free charge (electron or hole) is surrounded usually by a "bubble" of molecules, which organize themselves such that they neutralize locally its electric field. This reorganization of molecules is called a polaron, and the energy required to obtain it is the polarization energy (P).

3.2.1 Liquid/Metal Interface Phenomena

At the metal liquid interface, when no voltage is applied, a chemical and electrical equilibrium is reached upon formation of a series of charge layers (Lewis, 1994). The first layer consists of a cloud of electrons extending beyond the positive metal cores of the electrode (Figure 3.2). A layer of ions and molecules of liquid will be absorbed into this cloud, forming an inner Helmholtz layer. The outer Helmholtz layer extends in the region where ions will start to acquire a polarization sheath (polaron) similar to the one that they would have in the bulk. Beyond the outer Helmholtz layer a diffuse layer called Gouy-Chapman space charge layer is formed, which depends on the charge density in the bulk, and which for insulating liquids could be in the order of 10^{-7}m.

Within these layers electric fields of 10^9 V/m develop. These important electric field barriers should be overcome by a charge that tries to travel from or to the metal when no external electric field is applied.

As presented in Figure 3.3, the energetic levels at the liquid and metal interface, before being in physical contact, consist of the Fermi level (E_f) on the metal side, the localized electron and hole energy levels ($E_-(0)$ and $E_+(0)$) and the Fermi level of the bulk liquid $1/2(E_+(0)+ E_-(0))$ on the liquid side. At the interface the difference between the two Fermi levels of the liquid and metal equals the energy of the charge layers formed at the interface. The work function of most of the metals, which is equal to E_f, is between 4-5 eV. The $1/2(E_+(0)+ E_-(0))$ is likely to be larger than this for the liquids of interest, and thus a negative charge on the liquid side of the interface is most likely.

3.2.2 Low Electric Field Effects

When a potential difference is applied between the anode and cathode, the negative ions and electrons will be repelled, and positive ions and holes will be drawn in towards the cathode from the liquid bulk. At the same time, electron injection into the liquid will be encouraged, which will ultimately neutralize the positive charges accumulated at the cathode. A similar process will take place at the anode. During these "redox" reactions charge accumulation at the electrodes builds up a voltage barrier Φ at the electrode/liquid interface. In order for a charge to reach the metal surface, energies high enough to go through this potential barrier are required. At no applied voltage, the maximum of the potential barrier is located at a distance of 0.5 nm from the metal surface, when voltage is applied the maximum will have lower values and will move closer to the metal surface. At fields high enough the maximum can be within atomic distances from the metal surface such that the effects of the double layer will be removed (Lewis, 1994) thus electron injection is more important at higher electric field.

Electrons injected at the cathode will either reduce the incoming positive ions or holes or will produce a negative ion. For most liquids V_0 (bottom of the conduction band) is in the range –0.7 to 0.5 eV, and E_f (Fermi level in metals) is typically –4.5 eV so that a large potential difference must be generated by the double layer and the applied field to allow tunneling from a state close to E_f to a state in the conduction band to produce an ion (Lewis, 1994). On the other hand, neutralization of positive holes and ions should be more facile since the band of their empty states is expected to be much lower than the E_f. These considerations show that the positive charges present in the vicinity of the emitter

are more probable to be neutralized than negative ions to be generated at low field. Thus, ion-drag EHD pumping at low field is expected to be weak, if any.

The practical conditions, though, could be much different from the above theoretical considerations. The metal work functions can have deviations of up to 1eV from their average values. Also, insulating oxide and other tarnish layers could cover the metal surface. The presence of these layers can inhibit the electron transfer, but they also might enhance it (Lewis, 1994).

As Lewis (1994) explained in weak applied fields the localized electrons and holes drift as ions with their accompanying polarization shells (as mentioned earlier called polarons). If sufficient energy is gained, for example from a stronger external electric field, the electrons or holes can escape from their polaron becoming quasi-free, thus exhibiting higher mobilities than their trapped state. The probability of a quasi-free electron or hole to be trapped again depends on the collision energy exchanged with the other liquid molecules, thermal fluctuations in the energies of the bands and their localized states, and the kinetic energy imparted by drift motion in an applied field. The mobility of a quasi-free electron is determined by the scattering collisions in which the energy gained from the applied field is lost to the vibrational modes of the liquid molecules.

Thus, in their transit through the liquid the holes or the electrons can be in trapped or quasi-free states. Their overall mobility depends on the quasi-free and localized charges' mobility within the liquid and on the quasi-free time (t_f) and localized time (t_t) for the charges in their travel from one electrode to the other.

As Lewis (1994) shows, high fields affect the mobility of the localized and quasi-free states as well as their lifetimes. In fields up to 10^7 V/m two trends are evident in the drift velocity change with the field strength. Some liquids present a sub-linear variation of the drift velocity with the field strength showing saturation at high fields and thus a decrease in the mobility with the electric field. Other liquids show a super-linear variation, which means an increase in the mobility with the electric field. A possible explanation of this behavior is that for the first group of liquids the electrons are injected in a localized state and by gaining energy they become quasi-free and reach the collector in a delocalized form. For the other group of liquids the electrons are injected in a quasi-free form and will become localized. Injection in a localized state might be expected from a liquid with a positive V_0 (like liquid nitrogen) rather than a delocalized state injection for liquids with negative V_0. These considerations support the fact that moderate to high electric field can produce liquid nitrogen ions.

At high fields the potential barrier localizing the electrons will be lowered, and thus a lower t_t will be expected and an effective mobility closer to the quasi-free electrons mobility should be expected. Initially the quasi-free electron energy is limited by the various collisions involving vibrational modes or microscopic density fluctuations so that velocities lower then thermal velocity v_{th} are obtained. As electric field increases and the energy losses through collisions become less efficient, velocities higher than v_{th} could be reached, and thus molecular dissociations, electronic excitations or ionization will appear. As the field is further increased an avalanche of electrons will be generated by a repeated cycle of electron acceleration to ionization energies. The electronic processes at these field intensities will present current pulses and will be accompanied by light emissions

indicating the presence of "hot" electrons, which in liquid nitrogen have been experimentally observed (Frayssines, 2002 and Kadowaki, 2002).

3.2.3 Charge Mobility

A method to prove the existence of ions inside a liquid, of relevance for this work, in liquid nitrogen, is based on analysis of the charge mobility. This is why a small introduction in charge mobility studies is needed. The charge carrier's mobility is an important dielectric liquid electrical parameter which can provide us with information regarding the type of charges present in the liquid. A good information source in this field is the work of Schmidt (1997) which is used here. Different methods for detecting charges in dielectric liquids and measuring their mobility have been proposed. First, an external means of charge generation should be used. Usually electrons, holes, and ions are produced by photon or particle ionization of the liquid. Homopolar charges are induced by injection from one electrode or from the vapor space above the liquid. In all charge mobility experiments the injected charge density is small enough such that it does not affect the electric field distribution inside the cell. Also, relatively small electric fields are used such that the electrohydrodynamic motion between the electrodes is small enough to be negligible. Two main charge detection methods are used: conduction and optical absorption.

Electron mobility measurements for dielectric liquids provide two groups of values. Liquids such as helium or neon present low electron mobility values in the order of 10^{-2} to 10^{-3} cm^2/Vs, while for heavier rare gases liquids (like argon, krypton and xenon) mobilities of 100-1000 cm^2/Vs have been reported. These results are due to the different states of the electrons in these dielectric liquids. Low mobility liquids exhibit localized

electrons, while in the high mobility liquids the electrons are free. Some liquids exhibit both behaviors. A fast current signal inside the test cell shows the presence of fast charge carriers like free electrons, followed by a slow signal indicating the presence of attached electrons. Generally, it can be considered that a drift mobility >> 1 cm^2/Vs indicates delocalized electrons, while mobilities << $1cm^2/Vs$ are obtained for localized charge carriers. For electron mobilities that are close to 1 it is assumed that the electron spends a comparable amount of time in both localized and delocalized states. The delocalized electrons travel in the conduction band, and at high values of the electric field (E) their mobility decreases as $E^{-1/2}$ at first and then in the case of liquefied rare gases at still higher E as E^1 (Schmidt, 1999). At these electric field values the electrons are no longer in thermal equilibrium with their atoms, and they are heated by the electric field to energies of several eV above the thermal energy level, allowing them to reach velocities high enough to produce collisional ionization. In these cases electron multiplication is possible, and Trichel like pulses are reported.

Positive hole mobilities are much lower than $1cm^2/Vs$. The measurement of hole mobility is even more difficult than the electron mobility because impurities requirements are even stricter.

Positive and negative ions have been reported in non-polar dielectric liquids. Negative ions are formed by electron attachment to the liquid molecule or to molecules of impurities. Some of the very common impurities are oxygen from air or water molecules as well as dust particles. In most cases the mobility of negative ions is higher by a factor of two than the mobility of the positive ions. Liquid nitrogen is reported to have charge

mobility significantly lower than 1 cm^2/Vs, which allows us to conclude that one of the main charge transport mechanisms in liquid nitrogen is by localized electrons.

3.2.4 High Electric Field Effects

Under high electric fields electrons free or attached are generated (Schmidt, 1991) by electron injection from the metal to the liquid. For pure liquids near very sharp tips where high electric fields are located, electron injection currents following the Fowler-Nordheim dependence ($I \sim V^2$) (Halpern, 1969) on the applied voltage have been observed. The current flow through the liquid is dominated by the interface phenomena at these high fields.

A mechanism of current pulses and light emission for the negative polarity was observed experimentally at high electric fields. These mechanisms can be explained by the existence of electron avalanches (Arii, 1984). The existence of electron multiplication (Townsend mechanism) only in the close vicinity of the tip was found (Hernandez-Avila, 1994). The electrons emitted from the cathode form avalanches, which produce a rapidly growing current. The electrons move outward and attach, forming negative ions, which have lower mobility than the electrons. As a result, a space charge develops, which produces a lowering of the cathode field. The discharge stops when the space charge has drifted towards the anode. Then a new cycle starts. This explains the mechanism of current pulses encountered in experiments. The magnitude of the pulses remains the same while the frequency increases with the voltage.

3.3 LIQUID STATE ELECTRONICS OF CRYOGENIC LIQUIDS

Ion and electron properties of cryogenic liquids have been relatively extensively studied mainly for two reasons. One is the interest in cryogenic fluids, as electrical insulators. In

this case their pre-breakdown and breakdown characteristics (high electric field strength) are studied. The second interest is fundamental research, which focuses on the electronic states of liquids where ion mobilities (at low voltages in most of the cases) are estimated to explain the electronic properties of liquids.

When studying the electrical conduction properties of liquids the charge carrier mobility is usually measured. The ion mobility can provide information about the insulation properties of the liquid, its breakdown strength, and its conduction mechanisms. Two main electrical properties of liquid nitrogen which are charge mobility and dielectric constant need to be determined in order to be able to perform numerical simulation of liquid nitrogen EHD pumping.

Different authors have studied the electrical properties of cryogenic liquids. Gee et al. (1985) have studied ion and electron mobilities at low fields in cryogenic liquids, including nitrogen. They used high purity nitrogen (99.995%), and to further eliminate any impurities they used a special treatment. A parallel stainless steel plate (3.2 mm gap) arrangement was used, and the ions in the test cell were generated using an X-rays source. The cation and the anion mobilities were determined by the time of flight method, which measures the velocity of the charge carrier in passing through the test cell gap. They observed a fast component in the current pulse, which was due to the electrons, and a slow component, which was due to the ions. The nitrogen cation mobility was independent of the electric field over the range between 0.05 and 2.4 MV/m. In liquid nitrogen the existence of stable anions was reported. The electron in liquid nitrogen was not simply localized in a bubble (polaron) like in liquid helium but rather was attached to the nitrogen molecule to form a van der Waals dimmer ($[N_2]_2^-$). The anion was not stable

above 120K. The ion mobilities of liquids increased with the temperature. For liquid nitrogen, similar to some other cryogenic liquids, the product between the ion mobility and liquid viscosity was constant for a relatively wide temperature range between 75-110K at its vapor pressure. The LN_2 negative ion mobility at 77K and normal pressure was found to be about 0.12 cm^2/Vs, and the cation mobility was 1.7 times smaller.

Ramanan et al. (1987) have studied the electron thermalization distances and the free ion yields in LN_2 at different temperatures. They reported also that the electrons were captured to form anions. The LN_2 ion mobilities were measured using a time of flight method, and they found $\mu_- = 2.5\times10^{-3} cm^2/Vs$ and $\mu_+ = 1.4\times10^{-3} cm^2/Vs$. These mobilities were independent of field strength in the range 0.3-6 MV/m.

Loveland R. J. et al. (1972) studied the charge transport in diatomic molecular solids and liquids such as N_2, O_2 and CO. The rare gases (Ar, Xe, Kr) solids were found before to have conduction properties similar to the wide-band semiconductors, which means their solid state had mobilities as high as 4000 cm^2/Vs. The diatomic solids of N_2, O_2 and CO have different solid phases and their solid-state ion mobilities have been found to be much lower. In the experiments very small gaps between a wire and a plane were used in the order of tens of micron (20-100μm). The ion mobility results showed an increase of the ion mobility with the temperature and a constant product of viscosity and ion mobility between 65-80K at saturation pressure, as expected. Two types of carriers are detected in the current pulses. For liquids ionic transport was assumed as the main charge transport mechanism. The electrode spacing in most of the liquid experiments was higher than 50 μm. When the gap was lower than 30μm double transit pulse of positive and negative ions were observed in LN_2. The negative ions mobility was found to be about 1.5×10^{-3}

cm^2/Vs at 77K and 1.2×10^{-3} cm^2/Vs for the positive ions under and electric fields of 10MV/m.

Murooka et al. (1982) did some optical studies on the hopping-transport mechanism of excess electrons in liquid nitrogen. They discuss the two conduction mechanisms in liquids, which are ionic and electronic. The electronic conduction mechanism is divided in quasi-free electrons and trapped electrons. Using optical observations, they photographed electrical negative discharges in liquid nitrogen in a point-to-plane electrode configuration for a gap of 3mm at 1 atmosphere and 77K. They observed a maple leaf like disturbance propagation in the gap. A charge carrier mobility of 0.14-0.6 cm^2/Vs and an estimated velocity of $1.9\text{-}8.5\times10^4$ cm/s for the disturbance were reported for a high voltage of 42-44 kV. These mobilities are much higher (two orders of magnitude) than the electron mobility in liquid nitrogen (1.7×10^{-3} cm^2/Vs), and they assume that this happened because the charge density affected the electric field distribution. A hopping-transport mechanism was assumed for the charge transport. This mechanism consists of an electron attachment and release in its travel between the electrodes. Based on this theory, the low field ion mobility independent of electric field is between 1-2 cm^2/Vs, while for high fields it has an exponential increase with the electric field.

Kimura (1994) studied the electron drift mobility in mixtures of liquids. A mixture of up to 60mol% of N_2 in Argon was studied around 84K at an applied electric field strength between 0.5-4.5 MV/cm. The current signals had two components: a fast one, which was attributed to the delocalized electrons, and a slow one, which could be due to the

electrons attached to the LN2 molecule. The temperature, electric field, and molar percentage effect on the charge velocity are presented.

The fast electron velocity, at low molar percentages of N_2 (< 10mol %) and at low fields (<1 MV/m), for which the mean electron energy was smaller than the vibrational energies of N_2, agreed with the LAr values. For fields higher than 1MV/m the electron velocity became larger. As the molar percentage of N_2 (X) increased to 10 mol% for high fields, the velocity of free electrons (W_f) was still higher than in pure LAr. At a further increase in X, W_f decreased gradually at high electric field (E) and rapidly at low E.

The slow electron velocity (W_s) increased linearly with E and also increased with X and temperature. This behavior sustains the theory of electron attachment to the LN2 molecule. Initially, at low N_2 concentrations and electron energies the electrons exhibited the high mobility of the free electrons found in LAr, but as the molar fraction increased and the electron energy, obtained from the external field increased, the electrons were trapped by the LN2 molecules.

3.4 HIGH FIELD PHENOMENA IN CRYOGENIC LIQUIDS

To study the insulating properties of the cryogenic liquids, high field phenomena have also been studied. Various authors have researched the cryogenic liquids' conduction, pre-breakdown, and breakdown mechanisms at high electric fields.

Atrazhev et al. (1991) modeled the impact ionization and the electric breakdown strength for atomic and molecular liquids. They assumed that the electric breakdown of the high electron mobility liquids (atomic liquids like Ar, Kr or Xe) is determined by the ionization electron avalanche development. From the fact that the DC and laser induced breakdown strengths of these liquids are lower than the corresponding low density gas

breakdown extrapolated values, they concluded that in liquids, inelastic electron energy losses are absent due to the inexistence of excited atomic energy states. For low electron mobility molecular liquids the electrical breakdown for a long pulse duration occurred via the "bubble" mechanism (very localized boiling), but for lower pulse durations or gaps the mechanism was dominated by the electron avalanches. They defined an ionization coefficient for liquids similarly to the Townsend ionization coefficient for gases. An expression for the ionization coefficient for the atomic and molecular liquids was proposed, and a breakdown voltage expression was derived.

For atomic high electron mobility liquid the ionization coefficient is given by:

$$\alpha_L = \frac{2.8e}{I_L W}\left[\frac{I_L \delta}{m}\right]^{0.5}\left[\frac{E_{e1}}{E}\right]^{1.75}\exp\left[-\left(\frac{E_{e1}}{E}\right)^2\right] \qquad (3.1)$$

where $E_{e1} = 0.87e^{-1}\delta^{0.5} q_e I_L N$

and e is the electron charge, I_L the conduction band bottom energy level, W the electron drift velocity, δ = 2m/M is twice the electron-atom mass ratio, m and M are the electron and atom masses, E_{e1} is the threshold field defined above, E the applied field, q_e the collision cross-section, and N the number density.

For molecular liquids (like nitrogen) ignoring the electron energy losses by excitation of electronic states, the ionization coefficient is:

$$\alpha_L = \frac{3e}{I_L}\left[\frac{E_v}{E}\right]^2\exp\left[-\left(\frac{E_v}{E}\right)^2\right] \qquad (3.2)$$

where $E_v = \frac{N}{e}(G' I_L q_e q_i)^{0.5}$

and G' is the characteristic field strength defined by the vibrational excitation cross-section $q_i \sim 10^{-16}$ cm^2. In these expressions the constant values were determined using experimental data obtained with n–heptane.

Hernandez-Avila et al. (1994) have investigated the electrical and transport parameters such as threshold voltage U_s, and apparent mobility K for liquid nitrogen in gaseous and liquid states. For purified non-polar liquids in a point cathode configuration a corona discharge regime was established in the close vicinity of the tip. Thus, a liquid Townsend coefficient could be used to describe the ionization properties of the high field corona in liquids. The experiments used a tungsten tip (1-10μm) at a distance of 4-10mm from a collector plate. For liquid nitrogen they found that the threshold voltage (voltage at which a detectable current appears > 10^{-12}A) depends only on liquid density N and tip radius r_p and is independent of the hydrostatic pressure (up to 6MPa), a fact that sustains the hypothesis that the discharges take place in the liquid phase. A method for calculating the ionization coefficient for liquid nitrogen is presented whereby

for $E/N \leq 0.512\ F_V/N$ $$\frac{\alpha_{liq}}{N} = \frac{3e}{I_L}\frac{E}{N}\left(\frac{F_V}{E/N}\right)^2 \exp\left(-\left(\frac{F_V}{E/N}\right)^2\right) \tag{3.3}$$

and for $E/N \leq 0.512\ F_V/N$ $$\frac{\alpha_{liq}}{N} = \frac{0.5e}{I_L}\frac{E}{N} \tag{3.4}$$

where $F_V = e^{-1}\ N(G'I_L q_e q_i)^{1/2}$ is a characteristic field strength depending on the electron charge e and density N, G' is the vibrational energy of the molecular ground state, and I_L is the ionization energy of the liquid and of the q_e and q_i, which are the elastic and inelastic scattering cross-sections.

Taking into account the number density for liquid nitrogen ($N=1.7\times10^{28}$ m^{-3}) for electric field intensities of 459 MV/m, the ionization coefficient is 1.7×10^4 1/m and increases rather quickly to 1.7×10^7 1/m for E = 770 MV/m. From 770MV/m the variation is linear

up to $\alpha = 8.5 * 10^7$ 1/m. The negative corona onset threshold electric field strength was estimated to be 1000 MV/m.

Bonifaci (1994) has studied the work function of the cathode in non-polar liquids. Two types of conduction regimes were identified for non-polar liquids. For very sharp needles (r_p <0.2μm) a field emission current was observed which had a strong dependence on voltage (Fowler-Nordheim law) before reaching the space charge limit. Electric fields higher than 1000 MV/m at the tip (E_{FN}) were needed for the current onset ($I > 10^{-12}$ A) for this conduction regime in liquid nitrogen. Studies of the work function of a metal in non-polar liquids (Φ_l) at low voltages have shown that the work function in a liquid is related to the one in vacuum (Φ_v) by: $\Phi_l = \Phi_v + V_0$ where V_0 is the energy of the electronic conduction level. V_0 can be positive (neon, decane, cyclohexane) or negative (Ar, Xe, CH_4). V_0 is a function of the fluid density N. For liquids with a negative V_0 the excess electrons were quasi-free and their mobility was high, while for the positive or close to 0 V_0 liquids, the electron was localized and had low mobilities. The experimental data showed that the threshold value of the voltage at which Fowler-Nordheim emissions occur is related to the V_0 such that the smaller V_0, the lower the E_{FN}.

Another conduction regime took place at larger point radius (r_p > 0.5 μm) when a regular current pulse regime similar to the Trichel regime in air was detected above a threshold voltage U_s. The electric field intensity for this conduction regime was 3-4 times lower than the E_{FN} in the same liquid. A relation between the U_s and V_0 was again found. Liquids with higher V_0 will present a higher U_s. The electric fields in the vicinity of the tip were between 200-1000 MV/m. In this region a plasma-like layer was formed. This layer was generated by the discharges that can occur over small distances around the tip.

In this regime the space charge limited current was proportional to the V^2. Two different calculated values of the V_0 for the liquid nitrogen, which are 0.36 eV and 0.7 eV are presented. It is possible to estimate the maximum number of electrons in an avalanche using the ionization coefficient for molecular liquids using:

$$N(x) = N_0 \exp\left(\int_0^x \alpha(E(x'))dx'\right) = N_0 \exp\left[\frac{3r_p E_p e}{4I} \exp\left(-\left(\frac{E_v}{E_p}\right)^2\right)\right] \quad (3.5)$$

where it is assumed that the avalanche length is in the order of r_p. From here we see that the tip electric field E_p should be higher than E_v; otherwise the electron number is small. The radius of the electron swarm in an avalanche depends on Coulomb repulsion of electrons, and its minimum value can be estimated as $R > (eN/E)^{1/2}$. If the avalanche radius is smaller than $(eN/E)^{1/2}$ then its space charge generated electric field is larger than the external field, and the avalanche changes to a streamer. The maximum number of electrons for an electric field equal to the threshold field ($E_p = E_v$ = 700 MV/m) can be estimated at $n_{max} = 5\times10^{21}$ m^{-3} in liquid nitrogen. The presence of a high-energy layer around the tip (plasma layer) is determined by the fact that the electron energy necessary to leave this layer is very small (Φ_p = 0.01 eV).

Hernandez-Avila et al. (1994) have studied the hot electron phenomena in liquid and gaseous Ar and N_2 in divergent fields. The electronic phenomena in these liquids consisted of Trichel type discharges, which seem to be independent of pressure. These liquids were much more stable than the hydrocarbons but for energies high enough (>7.37 eV) the liquid nitrogen molecule was expected to dissociate. Purified gases were used and the charges have been generated using x-ray. The tip radius was between 0.1-12 μm and the gap between 0.5-10 mm. The negative corona onset for the LAr was reached

at electric fields of E_s = 200-300 MV/m and for nitrogen E_s = 1000 MV/cm. The mobility was calculated using the slopes of the $I_m^{1/2}$ (U) plots, and a value of 0.7-4×10^{-3} cm^2/Vs was obtained for the negative carriers in liquid nitrogen from space charge limited current measurements. This low mobility shows that the electrons are attached as N_2^- or N^- during the charge transport process. The apparent charge in liquid nitrogen for negative polarity was in the order of 1.7×10^{-1}pC.

For liquids, at very low tip radius, the field emission process occurred, which had a corona onset field strength 2000MV/m for argon and decreased with the tip radius increase. A set of current pulses appeared after the corona onset similar to the corona discharges in gases. For values of tip radius (r_p) higher than 10 μm the corona onset was almost constant E_s ~1000 MV/m for nitrogen and 200 MV/m for argon. The space charge limited current gave EHD mobilities of ~10^{-3} cm^2/Vs, which shows that the carriers were mainly ions and that liquid motion occurred. For the positive polarity no current could be detected at the relatively low electric fields used. The light emission analysis showed that for negative points in liquid nitrogen excited states of 11 to 12 eV existed, which means that very hot electrons capable of ionizing were produced near the point electrode. For liquid nitrogen an avalanche length (x_i) of the same order with the tip radius was obtained and the electric field at x_i was E_i ~350 MV/m (which is in good agreement with the breakdown voltage of 320 MV/m during microsecond pulses duration).

3.4.1 Cryogenic Liquids Breakdown

Kadowaki (2002) studied complete breakdown of liquid nitrogen / polymer film using photographic observations. The nitrogen and the film breakdown in a point-to-plane geometry were observed. The tip was made of stainless steel with a radius of about 1μm,

and the gap was 10mm. The plate was covered with a PET film of 20 or 50 μm and positive and negative step or ramp voltages of up to 50 kV were used.

For the positive tip, the breakdown voltage increased for both components (the film and the liquid) with the film thickness. First, the film breakdown took place, and subsequently the complete breakdown occurred. This happened because even at low fields applied electrons were emitted and charge accumulated on both side of the film, which produced a high enough electric field at the negative plane. Kadowaki concluded that the film increases the breakdown voltage for the positive tip due to the so-called barrier effect.

As the voltage increased positive charges were emitted at the tip and traveled to the negative plane, where they were collected. As they accumulated the potential across the film increased up to its breakdown voltage. If no film were present a smaller potential drop would build up until enough electrons were emitted from the plane to neutralize the present charges. The presence of the film suppressed the electrons emissions until the voltage drop across the film was high enough to produce its breakdown.

For the negative tip the barriers effect could not be observed. In this case the film breakdown occurred repeatedly until a complete breakdown because the film breakdown was much lower than for the positive tip case. This was because the mobility of the free electrons in liquid nitrogen was higher than the positive charges and the charges traveled faster in the case of negative tip, increasing the potential on the film surface to the breakdown value before enough charge density was built up in the space between the electrons to trigger the streamer. After a few discharges the attached electrons with a lower mobility traveled through the gap and created a charge density that was high enough to produce the breakdown of the liquid. The negative tip breakdown voltage for

the case when no film was deposited on the plane was between 45-60 KV for a gap of 10mm and a tip radius of about 1μm. For the positive tip a breakdown voltage of 42-45 kV was observed. The breakdown electric field intensities for the negative tip were between 8.5-11.3 GV/m and 7.9-8.5 GV/m for the positive tip.

This work shows that insulating the collector to increase the liquid nitrogen breakdown voltage is not a good solution.

Husain and others (1998) have investigated different insulation materials for super-conductor breakdown and their characteristics at cryogenic temperatures. They have measured the breakdown voltages for gaps of 1-5mm between electrodes of different shapes and sizes. A cone to plane geometry was also tested. The cone tip radius was 87.5μm. A relatively constant breakdown of liquid nitrogen was obtained at about 17MV/m for most of the tested geometries under 50Hz voltages. Also the breakdown characteristics of a set of materials at room temperature and at cryogenic temperatures were obtained.

Hayakawa et al (1997) have studied the breakdown mechanism of liquid nitrogen from the perspective of the effects of area and volume. They have measured the breakdown voltage in LN_2 with or without thermal bubbles for a sphere-to-plane and coaxial cylinder geometry under various pressures. The sphere tip radius was 3-25mm, and the gap was between 0.5-1.5mm. At atmospheric pressures they found a breakdown electric field intensity of about 100MV/m using 60Hz ac. They concluded that the insulation characteristics of the LN_2 largely depend on the stressed area and volume. The breakdown voltage was found to decrease sharply as the bubble volume increased and to saturate at large bubble volumes. Also, a smooth finish surface had a higher breakdown

value than a rough one. The rough surface produced decreases in the breakdown voltage of up to 30% with respect to the smooth surface at atmospheric conditions (close to saturation state) and lowered it as the pressure increased.

Hara et al. (2002) looked at the DC pre-breakdown and breakdown characteristics of liquid nitrogen in the presence of conducting particles. They used parallel and point-to-plane geometries. For the divergent field case they used a 20mm stainless steel sphere and gaps between 3-5 mm. They observed that the breakdown values for different conducting particles lay between the corona onset and the breakdown voltage, which means that, as expected, the breakdown strength of LN_2 is decreased by the presence of conducting particles. For a 2.5 mm parallel gap the onset and breakdown voltages were 7kV and 24kV, which gives field strengths of 2.8MV/m and 96MV/m.

Gerhold and others (1999) studied the DC breakdown of liquid nitrogen under different voltage ramping conditions. The breakdown voltage was measured for a parallel plate configuration with a gap of 1.25mm and a stressed area of about 500 cm^2. The voltage ramping was varied between 0.04kV/s and 68kV/s. The breakdown probability was found to be similar at lower voltages and had a larger span at higher voltage ramps. The mean electric field strength was about 15MV/m.

Frayssines et al (2002) looked at the pre-breakdown and breakdown phenomena under quasi-uniform field, ac, and impulse voltage in liquid nitrogen. The test cell consisted of a 10mm diameter sphere at 1mm distance from a plate; both were of stainless steel. In LN_2 negative streams were formed at lower voltages than positive ones but their propagation speed was lower than the positive streamer velocity. As a consequence the breakdown voltage at positive polarities was much lower than at negative ones. The

breakdown mechanism was controlled by the streamer initiation. The discharge initiation voltage of negative streamer was lower than the positive one. The initiation fields increased with the absolute pressure from 60-80MV/m at atmospheric pressures to 75-105MV/m at 0.5MPa.

For point plane geometry much lower values for the streamer initiation were obtained. Negative polarity applied to a 1μm tip radius electrode produced a negative streamer at 1400 MV/m. The initiation fields were 40% higher at positive polarity at point-plane geometry.

3.4.2 Other Electrical Phenomena Occurring in Cryogenic Liquids

Denat et al. (2002) presented a study on the thermally and electrically induced bubbles in liquid argon and nitrogen at high fields. To avoid thermally generated bubbles higher hydrostatic pressure should be sustained. Experimentally, pressures higher than 0.5MPa will eliminate the effect of the thermal bubbles on the dielectric breakdown of LN_2. Electrically induced bubbles were obtained at high electrical stresses. For negative polarity, in a point to plane geometry, at the threshold voltage V_s, the current jumped by several orders of magnitude and showed regular pulses. The pulse duration was about 10ns in LN_2. These current pulses were due to electron avalanches in the liquid. For electron avalanches to appear the electric field strength in LN_2 had to be 1100 MV/m for a tip radius of 1μm. A localized non-equilibrium plasma layer formed around the tip, which had a radius of the same order of magnitude as the tip radius r_p.

Arii K. and Schmidt W. F. (1984) have studied the current injection and light emission in liquid argon and xenon (atomic liquids) in a divergent field. The current and the light emission characteristics in purified and non-purified LAr and LXe were measured for a

point-to-plane geometry. The currents read were very noisy at low current values, but after a steep increase at values higher than 10^{-9}A stable currents could be measured. The obtained current in LAr at 87K for a gap of 2mm and an applied voltage of 2-4 kV was between 1-80nA, while for the LXe it ranged between 1-80nA for a gap of 0.85mm and a voltage of 1.5-3kV. At low current levels the I – V characteristic is given by the rate of charge generation at the tip, while as the rate of charge carrier generation increased, the current was dominated by a space charge limited process.

Charge carriers formed at the tip by two processes called field emissions and field ionization. The field emission took place when a negatively charged tip electrode transferred electrons by a tunneling process to the liquid. The energy barrier for an electron to undergo an field emission process is given by $\Delta\varepsilon_{fe} = | \Phi_v - V_0|$ where Φ_v is the work function of the metal with respect to the vacuum, V_0 is the energy of the electronic conduction level in the liquid, and the energy barrier for an atom to be ionized by a field ionization process is $\Delta\varepsilon_{fi} = | I_l + V_0 - \Phi_v |$. If the energy barrier for field emissions is smaller than the one for field ionization, the field emission sets in earlier than the field ionization and the conduction current for the negative polarity is higher than the one for the positive polarity. This was observed experimentally for LAr. If the two energies are comparable than the current for different polarity are very different, as in the case of LXe or LN_2. The space charge limited current had a linear variation in a V vs. $I^{1/2}$ plot.

The mechanism of current pulses and light emission for the negative polarity was explained by the existence of electron avalanches. The electrons emitted from the cathode formed avalanches, which produced a rapidly growing current. The electrons moved outward and attached, forming negative ions, which have smaller mobility, and thus a

space charge developed which produced a lowering of the cathode field. The discharge stopped until the space charge drifted towards the anode. Then a new cycle started. The magnitude of the pulses remained the same while the frequency increased with the voltage.

Bonifaci and Denat (1996) have looked at the transport phenomena in a point-plane geometry in liquid argon. The tip radius was about 0.1-2μm and the gap 0.5-10mm. The I-V behavior of the point to plane geometry in a field emission mode showed a $V \sim I^{1/2}$ (Nordheim-Fowler type relation) when the charge density remained under a certain level such that the field was not disturbed by the charges. When the charge density increased such that the negative charges were not removed fast enough, the process was governed by a space charge limitation. Two relations were obtained as a solution of the Poisson equation for a hyperboloid approximation of the tip:

$I = \frac{\pi \varepsilon_r \varepsilon_0 v}{0.3}(V - V_0)$ for a constant carrier drift velocity (v) and

$I = 4\frac{K \varepsilon_r \varepsilon_0}{d}(V - V_0)^2$ for a constant mobility (K).

For a small tip radius ($r_p \sim 0.1$ μm) electric fields of 2000 MV/m were necessary to obtain corona onset. For a larger radius ($r_p > 0.5$ μm) electron avalanches were the dominant process. At fields higher than 300-400 MV/m current pulses were obtained. The liquid purification had a very important effect on the current level, while the onset voltage did not depend on the liquid purification in an equally important manner.

3.5 SUMMARY

The chapter presents the electric properties and phenomena that occur in dielectric liquids followed by a particularization on the cryogenic liquids and more specifically on liquid

nitrogen. This chapter presents also the current understanding regarding charge carrier generation in cryogenic liquids which explains why EHD pumping of these liquids is possible. In liquid nitrogen, for negative polarity, the presence of a bonded electron state was found. Electrons are emitted from the metal surface in the shape of corona-like discharges (usually from the charged electrode sharp tip) for fields high enough (higher than 300 MV/m) and are localized relatively quickly forming negative nitrogen ions, which are transported across the electrode gap. The negative mobility of these ions is reported to be around 2.5×10^{-3} cm/Vs. The electric current levels are in the order of nA, and a linear variation of the V with the $I^{1/2}$ is observed at voltages above the threshold voltage.

These considerations suggest that for EHD pumping of liquid nitrogen the negative polarity should exhibit a better pumping performance. Ion-drag pumps using liquid nitrogen would rely on liquid nitrogen ion generation and transport to produce motion.

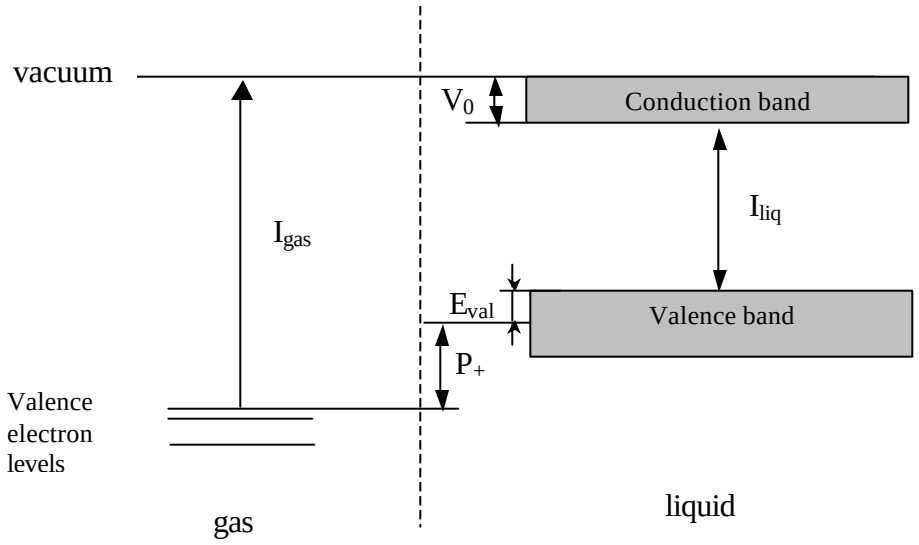

Figure 3.1 Electronic energy bands in a liquid (Schmidt, 1991)

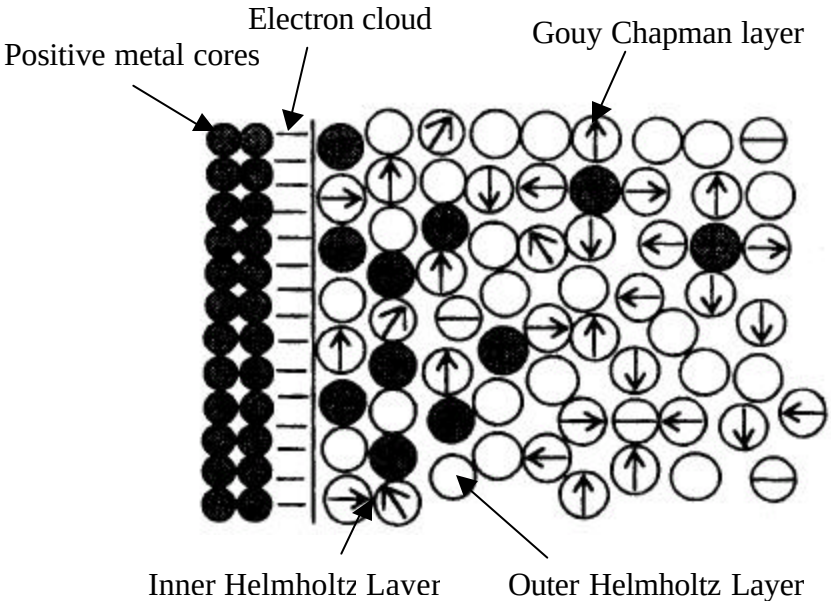

Figure 3.2 The metal/liquid interface layers (Lewis, 1994) (Legend: arrow – polar molecule and its orientation, empty – neutral molecule, full – positive molecule, line – negative molecule)

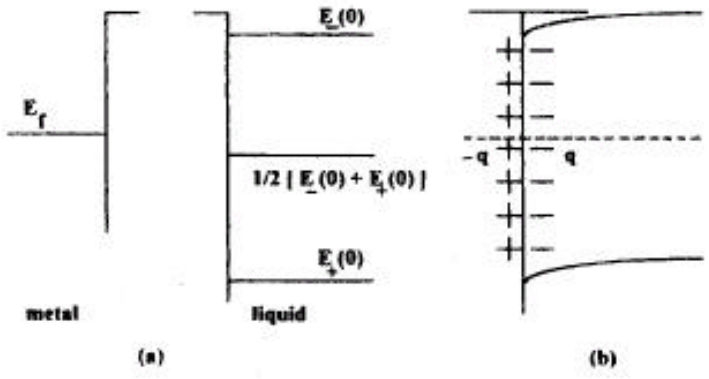

Figure 3.3 Energetic levels at the metal/liquid interface before (a) and after (b) they are put in contact ($E_{-/+}(0)$ – localized electron/hole energy level, E_f – Fermi level) (Lewis, 1994)

CHAPTER 4 DESIGN, FABRICATION AND TESTING OF THE EHD ION-DRAG MICROPUMP

4.1 INTRODUCTION

This chapter presents the design, fabrication and testing of a novel ion-drag electrohydrodynamic (EHD) micropump. Different emitter electrode designs, with the objective to maximize the electric field gradients between the emitter and collector electrodes, were designed and tested. The results quantified the effect of various electrode designs on the pumping performance. The micropump was packaged using an epoxy-gasket, which bonds two ceramic substrates together. On one of the substrates, planar or 3-D electrodes were patterned using MEMS techniques. The micropump was packaged such that it can be integrated directly on the back of a heat source (e,g, computer chip). While the meso-pump demonstrated in Chapter 5 takes care of losses in the loop, the micropump will provide local pumping (chip level) of the fluid over the heat source, thus boosting the overall pumping capability in the loop.

The micropump fabrication uses cost-effective microfabrication technology and thus is suitable for mass production using micromachining techniques. The micropump layout was obtained by TRW Company by sputtering niobium on the ceramic substrate and was patterned using a reactive ion etching technique. The micropump dimensions are $19 \times 15 \times 1$ mm and are chosen to fit a typical heat dissipating microelectronic device. The micropump design is flexible, allowing its dimensions to be chosen according to the application. Using the basic EHD micropump pattern, consisting of the emitter/collector pair, the whole heat-dissipating surface can be covered by replicating this pattern.

As presented in the previous chapter, EHD micropumps have been investigated by a number of researchers over the past decade (Bart et al., 1990; Richter et al., 1991; Fuhr et al., 1992; Fuhr et al., 1994; Cho and Kim, 1995; and Ahn and Kim, 1997). Richter et al. (1991) proposed one of the first ion-drag EHD micropumps consisting of two parallel grids obtained from micromachined silicon substrates, anodically bonded. The grids were 3 mm $\times$ 3 mm in size and consisted of 70 or 140 μm through-holes in a 380 μm thick silicon wafer. The results were promising, with a maximum pressure of 2500 Pa and a maximum flow rate of 14 ml/min being obtained with ethanol at an applied voltage of 700 volts. Fuhr et al. (1992 and 1994) and Cho and Kim (1995) used a traveling electrical wave to drive the fluid along the pumping channel. Ahn and Kim (1997) proposed a micro ion drag pump with planar electrodes with electrode spacing of 100μm and which at 100V provided up to 250Pa in static pumping tests.

As concluded also in the previous chapter, among the advantages of an EHD pumping system are the lack of moving parts (no wear or contamination due to lubrication), ease of mass production, low cost manufacturability, and the controllability (pumping output can be controlled by the voltage applied), which is inherent in all EHD pumps. Last, but not least, EHD pumps consume negligibly small power (on the order of milliwatts) for the dimensions listed here.

4.2 MICROELECTROMECHANICAL SYSTEMS AND MICROFLUIDICS

The micropump in the present study is a microelectromechanical systems (MEMS)-based device that can be utilized in microfluidic systems to deliver liquid to hot spot(s), with applications to cooling of the next generation electronic devices.

MEMS is an interdisciplinary field that represents a new branch in mechanical engineering dealing with small devices which incorporate mechanical and electrical components. The fabrication techniques used in MEMS are mainly derived from the integrated circuits fabrication industry. The MEMS devices' dimensions range from micrometers to millimeters.

A very wide range of applications has been explored in the last decade and increasingly successful MEMS implementations can be found. MEMS devices can be used to sense and actuate at small scales. Some of the most popular MEMS applications are pressure sensors and accelerometers for airbags, gyroscopes used in navigation devices, actuators for micro-mirrors, or switches in optical applications. Concepts like "lab on a chip" or integrated transducers are active research topics in the MEMS area. Another interesting domain opened by the application of the micro machining techniques in producing mechanical devices is microfluidics. Microfluidics deal with fluid manipulation devices, which incorporate small fluid passages. Some of the most promising applications of microfluidics are found in biomedical systems and cooling systems. Most of the above applications require means to transport the fluids, which are provided by integrated micropumps. Systems like laser-diode arrays, radar systems, and high-speed computer multi-chip modules could benefit from microcooling systems developed using MEMS techniques that incorporate micropumps to drive the fluid.

4.3 THEORETICAL BACKGROUND

The EHD effect occurring when an electric field is applied to a dielectric fluid medium has been known and applied for decades, but with the advent of MEMS new and promising applications can be developed. By applying voltage to a dielectric fluid an

ordered fluid motion is obtained due to the field-induced charges driven by the Coulomb force, which results in a pumping effect. This effect is called electrohydrodynamic (EHD) pumping and is produced by the interaction of the electric field and the free charges in the dielectric fluid medium. The pumping effect is achieved when the charged particles drag the neutral molecules in a given direction. When an electric field is established between a high voltage electrode, called an emitter, and a grounded electrode, called a collector, the electric field between the electrodes drags the charged fluid particles through the fluid, thus setting the fluid in motion. This type of EHD pump is called an ion-drag pump. The body force that is acting on the fluid molecules can be expressed by the following equation (Melcher (1981)):

$$\vec{f}_e = q\vec{E} - \frac{\varepsilon_0}{2} E^2 \nabla \varepsilon_r + \frac{\varepsilon_0}{2} \nabla \left(E^2 \rho \frac{d\varepsilon_r}{d\rho} \right) \tag{4.1}$$

where ρ [kg/m^3] and q [A×s/m^3] are the mass and charge density fields within the fluid, E [V/m] is the electric field, ε_0 is the permittivity of vacuum, and ε_r is the dielectric constant of the fluid. The first term represents the Coulomb force, also called the electrophoretic force, and acts on the charged species within the fluid. This component of the EHD body force contributes the most to the ion-drag pumping. The second component of the EHD body force, called the dielectrophoretic force, is related to the gradients of the dielectric constant in the fluid medium. The dielectrophoretic force acts on the neutral particles if a non-uniform electric field is present. The third term in the above expression is called the electrostrictive force and is related to the electric field non-homogeneity within the dielectric medium. In a single-phase fluid, the last two terms are often ignored, since the changes in the electrical permittivity of the fluid over the small distances that separate the two electrodes are negligible.

Pickard (1959), Steutzer (1963) and Melcher (1981) have developed theoretical models for ion-drag pumping. The main assumptions include parallel plate geometry where the electric field is uniform, unipolar injection and space charge limit conditions, neglected turbulence and secondary effects, and surface charges on the insulating boundaries. Balancing the pressure force and the electrohydrodynamic force,

$$\nabla p = qE \tag{4.2}$$

or, for a 1-D planar configuration,

$$\frac{dp}{dx} = qE \tag{4.3}$$

These models predict the pressure generation to be proportional to the electrical permittivity of the fluid and the square of the average electric field; therefore,

$$\Delta p \sim \varepsilon(E^2 - E_0^2) \tag{4.4}$$

where p is the static pressure, x is the coordinate perpendicular to the plane of the charged plates, q is the space charge density, and E is the electric field strength.

Stuetzer determined the maximum static pressure obtainable from a plane parallel electrode ion-drag pump to be

$$P_{max} = \frac{9}{8}\varepsilon\left(\frac{V - V_0}{d}\right)^2 \tag{4.5}$$

where V_0 is a threshold voltage when the pumping starts and d is the distance between the plates.

Pickard introduced an efficiency coefficient η, which accounts for emission laws at the electrode:

$$P_{max} = \frac{9}{8}\eta\varepsilon\left(\frac{V - V_0}{d}\right)^2 \tag{4.6}$$

It should be mentioned that these relations only give a qualitative expression for the pressure head due to simplifying assumptions made in deriving them. However, they show that the pumping capability of an EHD ion-drag pump depends on the dielectric permittivity of the fluid and the electric field strength. Thus, fluids with higher dielectric values will cause a greater pumping effect. Also, the relations show that pumping increases quadratically with the electric field strength.

The electrode design plays an important role in designing an EHD pump. The design should balance two counteracting trends. One is the filtering effect (hydrodynamic drag) of the electrode on the fluid flow, and the other is the efficiency of the ion injection and transport process in the bulk fluid. In a microscale design these considerations are also very important, since the overall pumping efficiency depends on the efficiency at which the free charges are injected in the fluid, the location where they are injected with respect to the pumping channel wall, and the pressure drop penalty caused by the flow obstruction due to the emitter and collector. The injection process depends on the electric field strength at the tip of the emitter; thus, for ion injections to occur minimum electric field strength at the injection point is required. The momentum of the microjets generated by the acceleration of the free charges due to the Coulomb forces towards the collector should be transferred mainly to the bulk fluid, and the momentum depends also on the average electric field between the electrodes. If the highest-intensity electric field region is very close to the wall, these jets will be transferring their momentum to the wall, resulting in a lower pumping efficiency. Thus, it is desirable to keep the ion injection elements close to the wall to act in the region where the shear stresses are large, while

keeping them far enough away to have an efficient transfer of the momentum to the bulk fluid.

Another factor that has to be taken into account is the additional pressure drop introduced by the presence of the emitters and collectors in the fluid path. Thus, the collector should be designed such that it will introduce the smallest pressure drop in the flow, while the emitter design should be optimized to balance the optimum free charge injection with the momentum transfer to the bulk fluid, and the lowest pressure drop.

In an ion-drag pump, pumping is achieved if the electrical shear stresses are higher than the viscous shear stresses. In most cases the flow obtained in micropumping is laminar. In laminar flows the highest shear stress that resists the flow is at the channel wall. Thus, the locations at which the ions are generated and to which they are accelerated play an important role in determining the overall pumping efficiency. As this study shows, using bump-shaped electrodes which balance the two trends described above will provide the best pumping performance.

4.3 DESCRIPTION OF THE MICROPUMP DEVICE

4.3.1 Design

Figure 4.1 depicts the schematic of the micropump device. The micropump consists of two ceramic substrates that are bonded together by an epoxy gasket to form a pumping channel of about 100μm high. On the bottom substrate a series of patterned electrodes is deposited. Several electrode designs were tested to identify an optimum electrode design. Electrode design plays a critical role in maximizing the electric field intensity, thus leading to high EHD pumping heads at low power consumption. As shown in Figure 4.1, the micropump components used in the present micropump design include:

- A bottom alumina substrate on which a set of EHD pumping stages are deposited and patterned. The design consists of planar and saw-tooth emitters and planar collectors. The electrical connection strips are passed beneath the epoxy gasket, and the external leads are wire- bonded to them.
- An epoxy gasket that bonds the two covers.
- A top cover with inlet and outlet ports obtained using laser cutting of the alumina substrate.

The electrode geometry and dimensions were carefully selected to allow a wide range of test conditions with the objective of determining an optimum configuration. Four different electrode patterns were designed. The design layouts were prepared in Cadence. Each design measured 19 mm × 32 mm, representing typical dimensions of selected microelectronic devices.

The different geometries for the four designs are summarized in Table 4.1. The distances between the emitter and collector electrodes or the electrode gap (s) and the distances between the stages (d) were varied in the different layouts.

Table 4.1 Specifications of various design options (see Figure 4.2)

Design Option	Geometry	s [μm]	d [μm]	Emitter tip angle [degrees]	Number of stages
A1	Planar	50	100	180	95
A2	Saw – Tooth	50	100	~60	80
B1	Saw – Tooth	100	200	~60	50
B2	Saw – Tooth with bumps	100	200	~60	50

Design option A1 consists of a planar straight emitter and straight collector. The collector width is 30 μm and the base width of the emitter electrodes is 30 μm. The electrode gap (s) is 50μm while the stage gap (d) is 100μm. The total number of stages, which represent

a pair of emitter-collectors, is 95. This design option was included to serve as a base case in comparing the pumping performances of different designs.

The design A2 has a stage spacing of 100μm and a gap of 50μm, while the emitter geometry is similar to a saw with triangular teeth. The teeth allow a higher electric intensity at the tips, which results in better pumping. The strip connecting the teeth has a width of 20μm, and the collector width is 30μm. The teeth are triangular with a 50μm base and 50μm height.

Design B1 differs from A2 in that the electrode gap is 100μm and the stage spacing 200μm. These two designs allow us to study the effect of the electrode gap for the saw-tooth geometry.

Design B2 has geometrical characteristics similar to B1 to which a series of "bumps" formed by solder deposition was added on top of each saw tooth (Figure 4.4 and Figure 4.5). This design in conjunction with the B1 design will allow us to study the effect of the 3D bump structures on the pumping performance.

The Cadence layout for one of the designs is presented in Figure 4.3. The blue layer represents the epoxy sidewall, the red layer represents the inlet and outlet ports, and the green layer represents the EHD pump electrodes and the electrical connection leads. The scale is in microns.

4.3.2 Microfabrication

Fabrication of the electrodes was performed at TRW Corp. microfabrication facilities. A typical microfabrication process began with polished ceramic substrates. The square substrates were approximately 3-inch length, allowing six units to be fabricated in parallel. Niobium was sputter-deposited onto the ceramic, coated with photoresist, and

optically exposed using a 1X aligner. Following development, a reactive ion etch defined the niobium metallization pattern.

Some of the designs used a Ti/Pd/Au overlayer, capable of accepting solder. A liftoff pattern of photoresist was deposited, exposed, and developed. Ti/Pd/Au was sequentially evaporated in 40/400/40 nanometer thickness (Figure 4.5). These layers have the following roles: Ti serves as an adhesion/barrier layer; Pd is used as a solder contact layer; and Au provides protection against Pd oxidation. Rinsing off the remaining photoresist left Ti/Pd/Au behind on the chosen regions of the niobium. A solder dipping process deposited InSn solder onto the Ti/Pd/Au patterns forming the solder bumps. Depending on the shape of the adhesion region, different bump configurations could be obtained. Because the solder deposition process is surface tension dominated, the average height of a bump is about 12% of the base characteristic length. Some microscope photos of electrode structures are shown in Figure 4.6.

The top covers consisted of the same ceramic material as the base. Laseronics Corp. used a laser to cut the ceramic to the correct final dimensions and to include an inlet and outlet port on the top cover. The two covers were aligned and bonded using an gasket based on epoxy material, which was cured under pressure at about 150 °C for an hour. The epoxy layer thickness, which determines the channel height, was measured after the assembly and was found to be between 40 μm –70 μm. The range in numbers also includes some degree of tilt after assembly.

4.4 EXPERIMENTAL SET-UP

The experimental setup for testing the different micropump designs will be described in the following section. The experimental setup consists of a fluid container where the

micropump was placed (Figure 4.8) and a 1kV power supply to supply the EHD electric field.

4.4.1 The Working Fluid

Static pumping tests were performed using a 3M's heat transfer fluid called HFE-7100. The thermophysical properties of this fluid are listed in Table 4.2.

This fluid has low vapor pressure; hence it can be used for tests in an open container. It has a good dielectric constant (k ~7.4), a relatively low viscosity, and a relatively high thermal conductivity. The boiling point of HFE-7100 is 61^{o}C at atmospheric pressure.

Table 4.2 Thermophysical properties of the working fluid

Thermophysical Property	**HFE-7100**
Boiling Point (^{o}C) (at 1 atm)	61
Liquid density (kg/m^{3})	1402
Liquid kinematic viscosity (cSt)	0.38
Liquid specific heat (J/kgK)	1253
Dielectric strength (kV/mm)	11
Dielectric constant	7.40
Thermal Conductivity (W/mK)	0.068

4.4.2 Device Packaging

The device is shown in Figure 4.7. Two leads were wire-bonded to the electrode connections, or in some cases crocodile clippers were used. A plastic graded tube was attached on the exit port of the device using transparent epoxy. The tests were performed in a small transparent container (Figure 4.8). Except for the graded tube, the device was

completely submerged in a bath of a 3M thermal fluid. The tube grading was in millimeters, and the reading was done with the bare eye.

4.4.3 The EHD Power Supply

The output of a DC high voltage power supply from Brandenburg Corp. (http://www.brandenburg.co.uk/477.html) was connected to the electrodes. The power supply has a maximum voltage output of 1kV and a maximum current of 4mA with an output ripple of 4 mV and a current measurement uncertainty better than 1 μA. Both positive and negative polarities can be used.

4.5 EXPERIMENTAL PROCEDURE

The transparent container and the test module were carefully washed with acetone to avoid the contamination of the fluid with impurities. The pump was placed inside the liquid container and fixed to the bottom. Liquid was poured in the container until it covered the device. The tube was inspected to ensure that the liquid coming through the inlet port reached the tube, which meant that the pump was full of liquid. The voltage was increased gradually at a rate of about 100 V per minute. Once the pumping action was observed at a particular voltage, the stable height was read using the bare eye and recorded.

As can be seen in Figure 4.8, the pump produced a liquid column rise of about 45 mm, which corresponds to hydrostatic pressures above 700 Pa. In some cases as the voltage was further increased the liquid overflowed the tube. Additional details of the results will be given later in section 4.9.

4.6 DATA REDUCTION

The hydrostatic pressure was calculated from the recorded height using:

$$\Delta p = \rho g h \tag{4.7}$$

where ρ is the fluid density, g the gravitational constant and h the height rise.

The power consumption was determined using P = VI, where V represents the applied voltage and I the current flowing through the pump.

4.7 UNCERTAINTY ANALYSIS

The main uncertainty in determining the generated pressure head was the uncertainty associated with the height reading. A maximum reading error of 1mm was determined. Thus, a pressure uncertainty of 14 Pa is reported. The variations in density due to temperature changes as well as other effects like capillarity have been neglected.

The uncertainty of the power estimates is related to the accuracy of the voltage and current readings. The power measurement uncertainty was about 1mW.

4.8 RESULTS AND DISCUSSION

Several tests were performed to investigate the repeatability of data between different runs. The pressure head versus the electric field strength for different runs of each design is presented in Figure 4.9. The differences between different runs can be explained by the uncertainty in the height measurement as well as by the possible variations in the electrical conductivity of the fluid due to impurities. The data shows fairly good repeatability between tests allowing us to compare the pumping performance among different designs and to make general qualitative considerations regarding the new design features proposed in this work.

The pumping head results for the planar and the saw-tooth designs A1 and A2 with the electrode gap of 50 μm are shown in Figure 4.10. The electric field was estimated by dividing the voltage by the electrode gap. It should be mentioned that this approximation

is very rough, especially in the cases where a planar and a saw-tooth geometry are compared. Still, for the purpose of our study where we are mostly comparing average values for the specific gap, this approximation is acceptable and is commonly encountered in literature. The results clearly show a higher pumping performance with the saw tooth geometry as compared to the planar electrode.

Although the electrode gap is the same in both cases, the pumping started at a higher voltage for the planar electrode. This can be explained by the tip's higher electric field in the case of the saw-tooth electrode. It is known that the ion injection process is initiated at a threshold electric field, which is reached in the vicinity of the points with the highest curvature. For the saw-tooth configuration, high curvature points are provided by design. This is why the voltage at which the pumping starts, for a gap of 50 μm, is about 500 V for the planar configuration, while using the saw-tooth configuration decreased the voltage to about 150 V.

The pumping head for the configuration A1 was 600 Pa at about 900 V, while in the case of configuration A2 only about 200 V were needed to obtain the same pumping head. This behavior can be explained by improved ion injection efficiency in the case of design A2. In the planar configuration the ion injection sites are located at the tip of the planar electrode edge irregularities, while in the case of the saw-tooth geometry specific and evenly distributed injection locations are provided. The results show that the saw-tooth design presents better ion injection efficiency and lower threshold voltage than the planar configuration, which results in a better pumping performance.

The results obtained with the saw-tooth electrodes for electrode gaps of 50 μm (A2) and 100 μm (B1) are shown in Figure 4.11. The larger number of stages (pairs of electrodes)

in the 50 µm-gap device could be responsible for the better pumping performance of this design. The results show that the pumping for the case A2 starts at a lower threshold voltage than in the case B1. This is because the pumping starting voltage depends on the tip electric field, which for a smaller gap is higher.

The electric field intensity and the pressure head for the 100 µm saw-tooth design with and without 3-D bump structures (see Figure 4.6 b) are shown in Figure 4.12. The results show that the pumping effect is significantly improved by the presence of the bump structures. A possible explanation is that the number of active sites, represented by the points with high curvature on the emitter, is higher in the case of the bump electrode thus providing a more efficient ion injection. It can be seen that for the no-bump geometry, a pumping head of 500 Pa was obtained at a voltage of 1000 V, whereas this same pumping head can be obtained for the bump geometry at less than 500 V.

The experimental results for the four different designs are presented in Figure 4.13. Several observations can be made from these graphs. As expected, the planar design (A1) resulted in the lowest pressure head. The second observation is that a much higher pumping performance was obtainable with the saw-tooth emitters. The pumping head results obtained with the B2 design show that the presence of the 3D bump structures could significantly improve pumping performance. Among the four electrode geometries tested, the A2 design, which has a larger number of pumping stages, performed the best. Thus, it can be concluded that reducing the electrode gap, which also allows the number of electrode pairs to be increased, combined with the 3-D bump structures can significantly improve the pumping capability. Based on the results of this study, different configurations can be determined depending on the design requirements.

In the tests, steep increases of pumping head with the voltage could be observed, which is referred to as "threshold voltage." This is consistent with the general behavior of a dielectric fluid upon applying electric field. At low applied voltages, which are usually associated with low electric field intensities at the emitter, the pumping head and the current are low and are mainly due to the dissociated impurities transported between the electrodes. In this regime the current and the pumping are almost independent of the applied voltage. As the electric field is increased, eventually an emitter electric field high enough will be reached such that ion injection will occur. At this moment sudden increases in the current and pumping are observed, and the flow will be mainly due to the injected charges. The associated voltage is the threshold voltage. Interesting observations can be made on our experiments concerning this behavior. The impurities dissociation region is evident in the case of design A1 but decreases significantly for the design B1 such that for lower gaps and bump structures this region is almost nonexistent. This confirms our assertions that saw tooth and bump structures provide more efficient ion injection.

The rates of input electrical power consumption for the various micropumps as a function of pressure head for the various designs tested are shown in Figure 4.14. As can be seen in this figure, the lowest power consumption was obtained for the saw-tooth design with the smaller electrode gap. The planar design requires the highest power input, which makes this design the least desirable.

The currents versus voltage results are depicted in Figure 4.15. In most of the cases a sensible current occurred above 100V, when the dissociation current was expected to decay because most of the impurities were neutralized at the electrodes. Above this level,

a fairly repeatable current behavior was obtained. The results indicate that the variation of the current with the voltage is nearly the same for all the saw-tooth electrode designs tested, which means that they were operating in the charge limited region. For the planar electrode, the current-voltage behavior was similar to those of the saw-tooth electrodes up to a voltage of a 600 V. Beyond the 600 V level, the amounts of current began to deviate for the two types of electrodes. The current behavior of the planar electrode also suggest this electrode design was the least preferred choice.

4.9 SUMMARY

An experimental investigation was conducted to determine the feasibility of an EHD micropump with a set of novel features proposed to obtain a better pumping performance. The results of the experiments successfully validated the new concepts and showed that adding a saw-tooth electrode geometry combined with 3-D structures provides a significant increase in the pumping performance. Novel microfabrication techniques were used which proved very useful in obtaining better electrode configurations.

Four different designs were designed, fabricated and tested. The best configuration contained a saw-tooth emitter featuring a 3-D solder-bump structure. Using a 3M fluid with a gap of 50 μm and a saw-tooth emitter configuration (design A2) at an applied voltage of about 250 V, the micropump provided a pumping head of 650 Pa, while using a bumped saw-tooth configuration with 100 μm gap (B2) at 500 V resulted in a pumping head of about 750 Pa. One of the main objective of the micropump tests was to improve our understanding of on ion-drag pumping and electrode design, so that we can design a better electrode for the meso-pump that will be used in the cryogenic tests.

4.10 PRESENT WORK CONTINUATION

One of the major goals of the research presented in this thesis is developing a cryogenic spot cooling system using EHD pumping which includes EHD micropumps attached on the hot surface and eventually EHD meso-pumps. Zhao and Fourounghi (2003) published a paper on the cryogenic EHD micropumping which represents the continuation of the work presented in this chapter and was based on the conclusions drawn in the next chapters. Their paper presents the preliminary efforts on developing a micropump for cryogenic cooling of certain specialty electronics, including those of sensor and detector applications. A packaging method compatible with cryogenic applications is proposed. The tested micropump, fabricated by MEMS techniques, had a saw-tooth emitter and planar collector with 50-μm electrode spacing and 200 μm pair spacing. The pump was tested in sub-cooled liquid nitrogen (with about 7 K sub cooling). It was shown by the experimental tests that the EHD effects pump liquid nitrogen if the electrodes of the pumps are properly designed. The tested micro pump pumped liquid nitrogen at a flow rate of 2.3 g/min and had an output pumping head of 5 Pa when 1000 volts were applied across the electrodes.

This paper presents the successful testing of a cryogenic EHD micropump. This accomplishment combines the research in the EHD micropumping (Chapter 4) and the cryogenic EHD pumping (Chapters 5-8) which have been started in the work presented in this thesis.

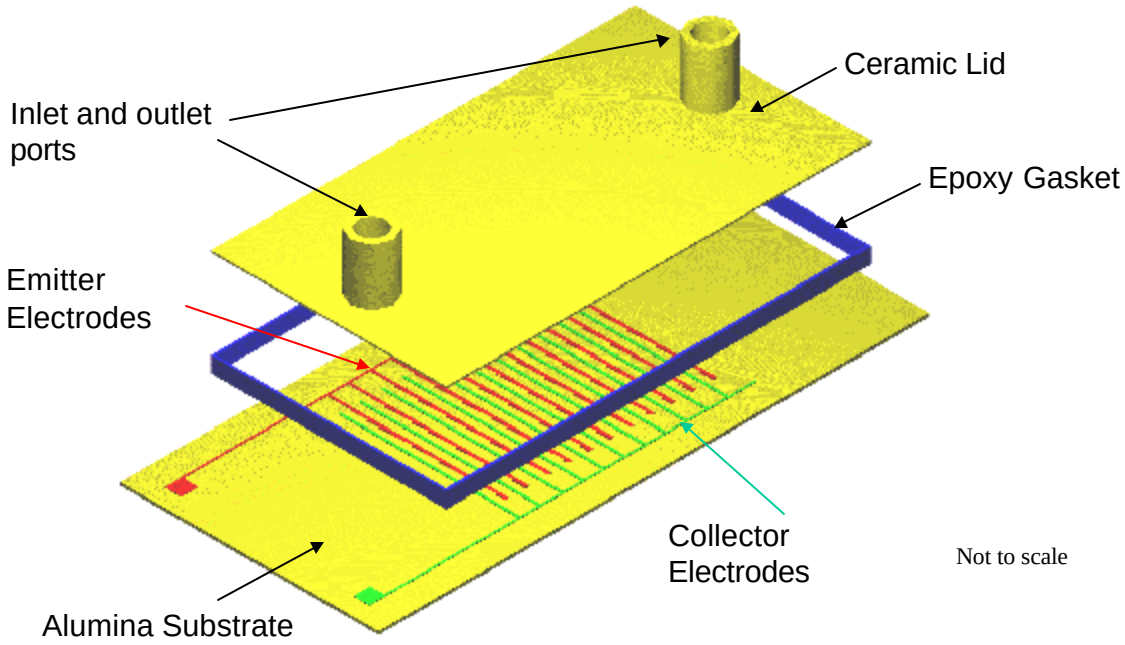

Figure 4.1 The schematic of the micropump design

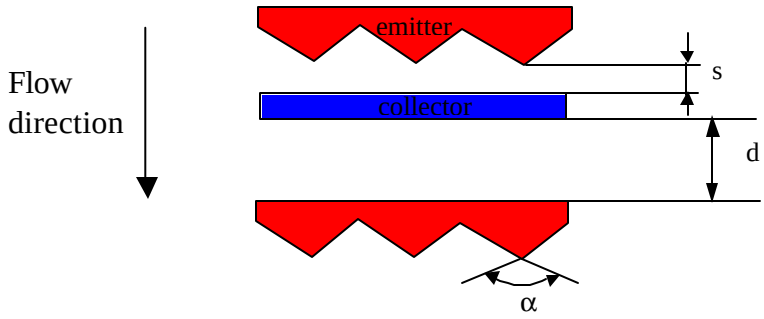

Figure 4.2 Schematic diagram of the emitter and collector electrodes

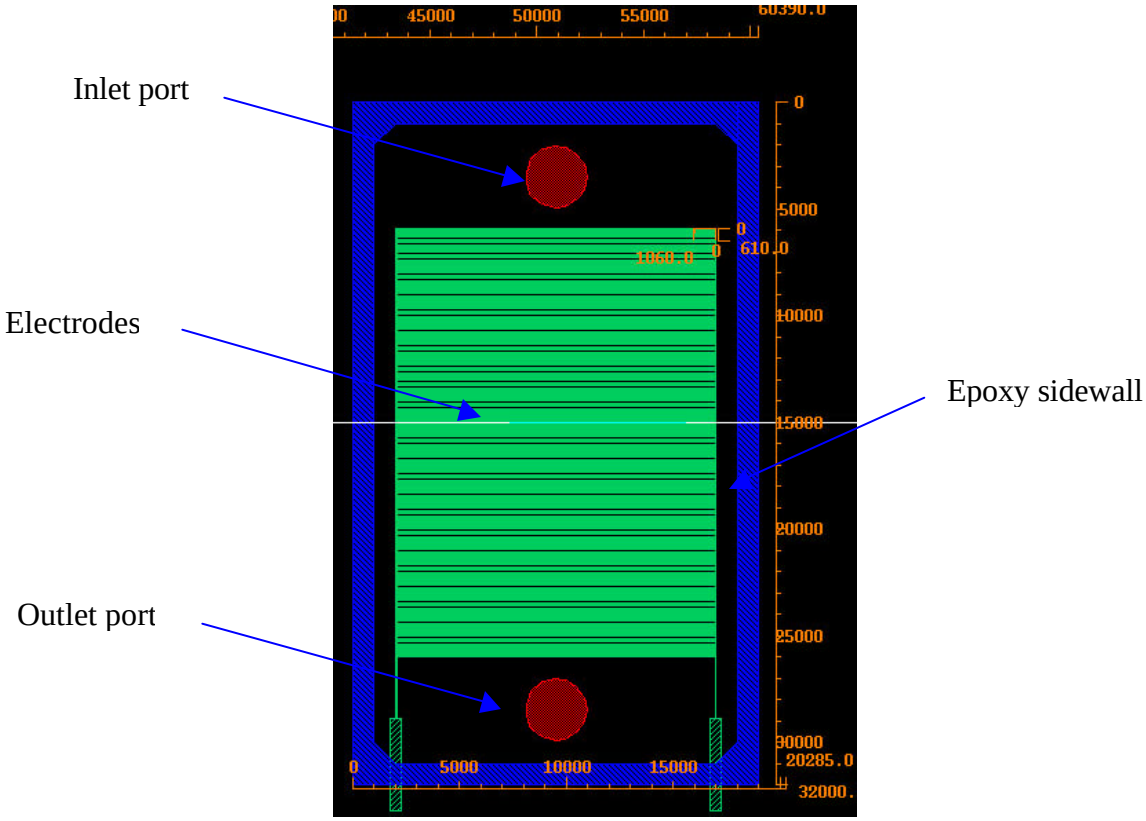

Figure 4.3 Cadence drawings of the micropump design (dimensions in μm)

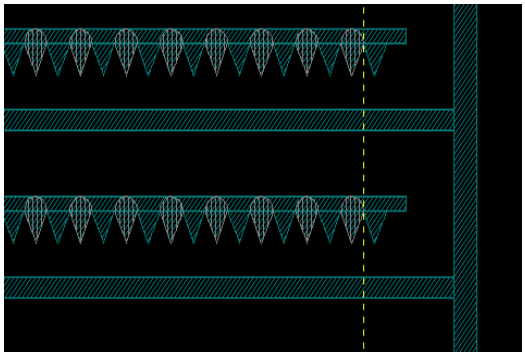

Figure 4.4 Saw-tooth electrode pattern with triangular bumps

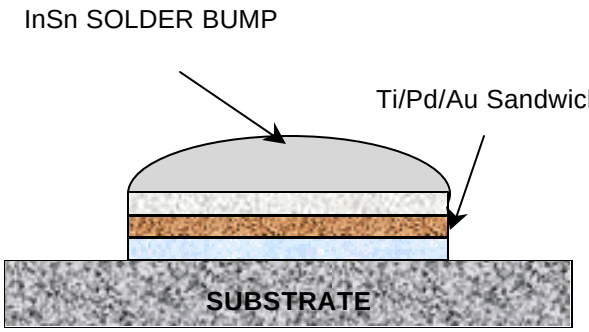

Figure 4.5 Schematic diagram of solder bump bonding

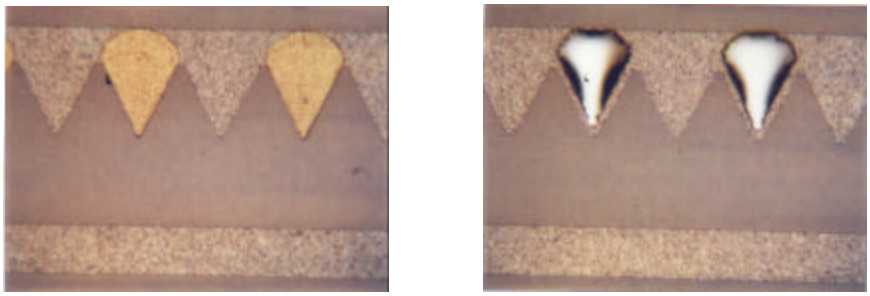

(a) Ti/Pd/Au overlayer (b) In/Sn solder bumps

Figure 4.6 Microscope photos of electrode structures

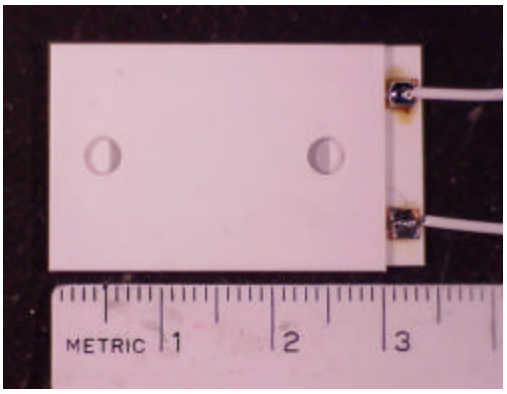

Figure 4.7 A photograph of the assembled micropump.

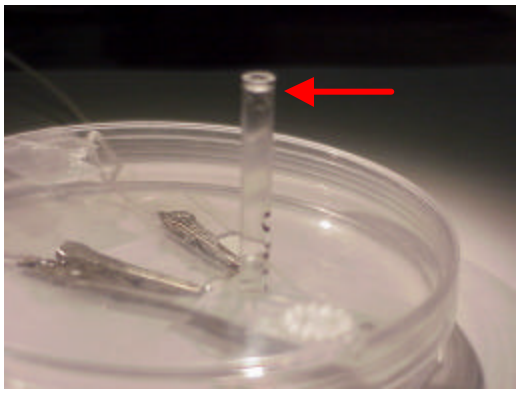

Figure 4.8 Static pressure test of device. Liquid column level is near the top of tube.

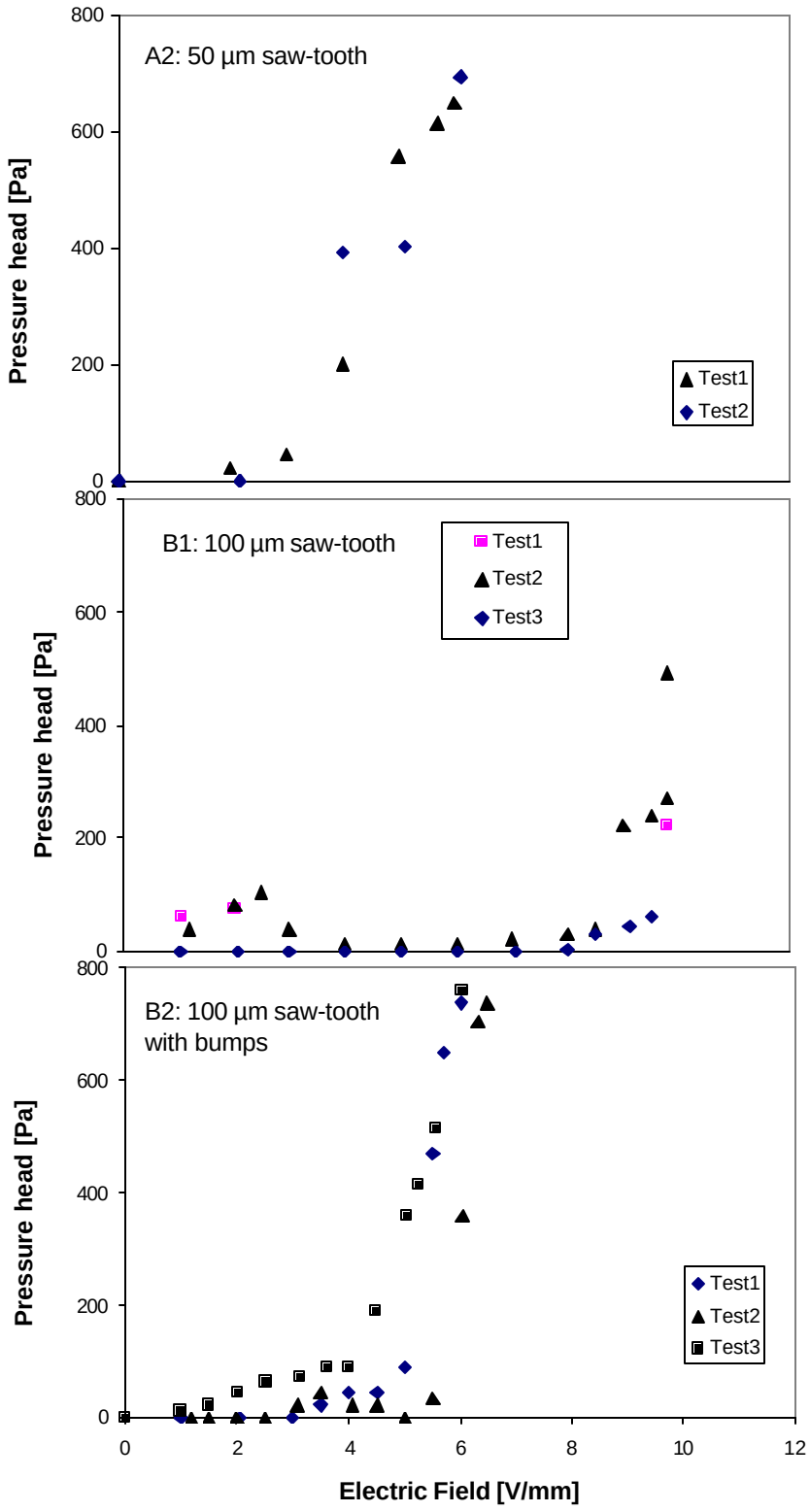

Figure 4.9 The pressure head versus electric field results for the designs A2, B1, B2 in different tests

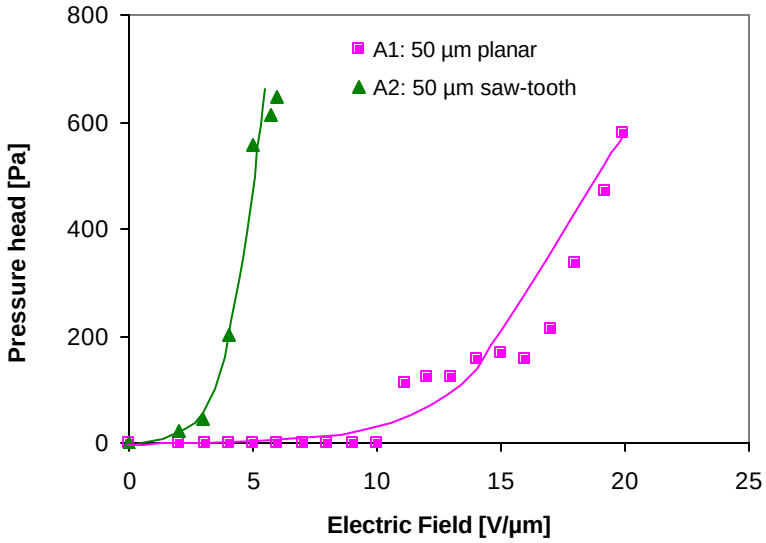

Figure 4.10 Pressure head versus electric field for the 50 µm planar and saw-tooth designs

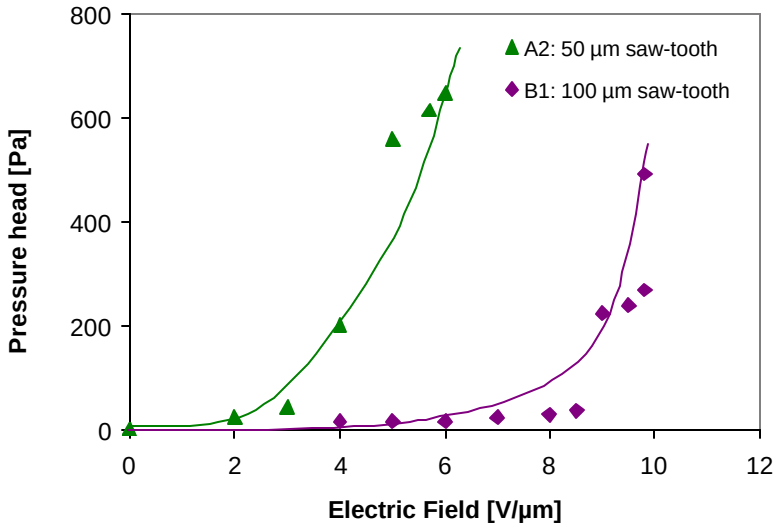

Figure 4.11 Pressure head versus electric field strength for two different electrode gaps

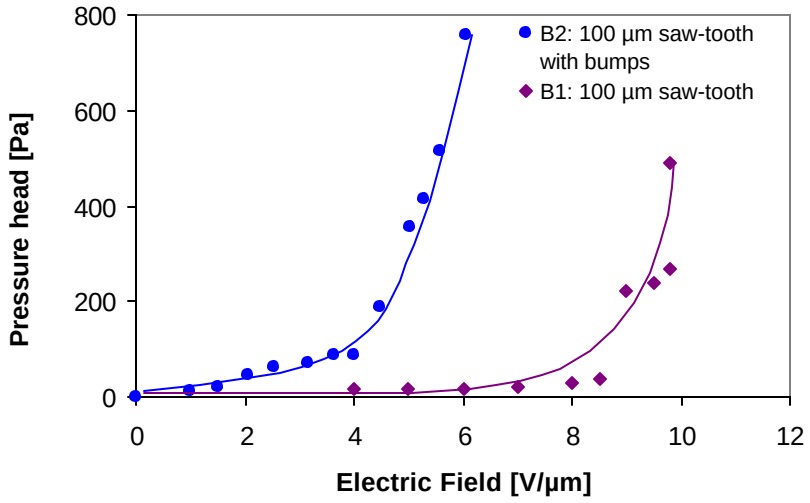

Figure 4.12 Pressure head versus electric field for 100 µm saw-tooth electrode with and without 3-D bumps on the electrodes

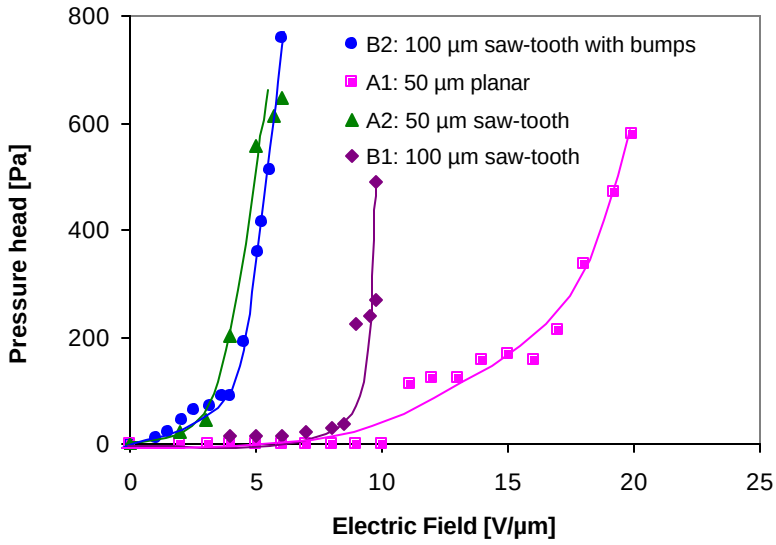

Figure 4.13 Pressure head versus electric field for various electrode designs

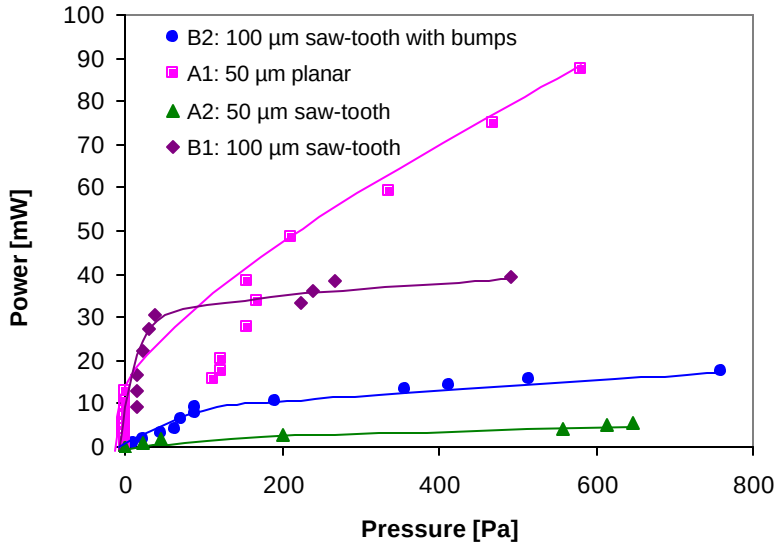

Figure 4.14 Input electrical power consumption versus generated pumping pressure for various designs

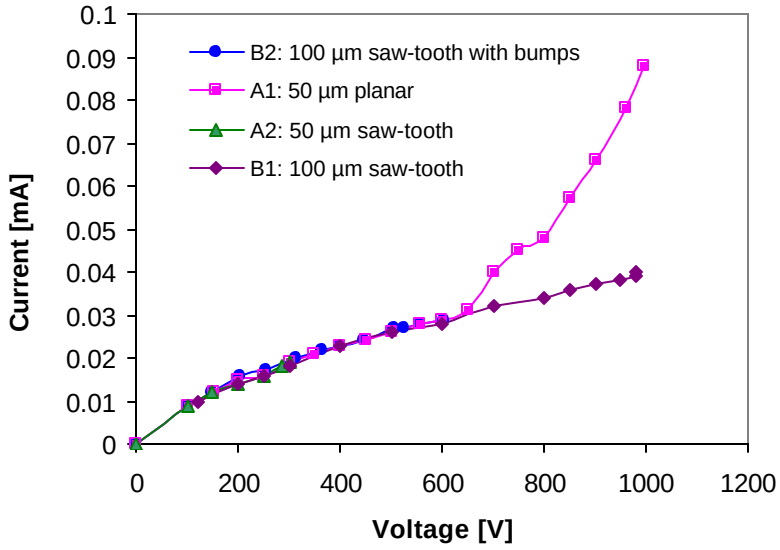

Figure 4.15 Electrical current versus voltage for various designs

CHAPTER 5 DESIGN, FABRICATION, AND ROOM TEMPERATURE TESTING OF THE MESOSCALE EHD PUMP

5.1 INTRODUCTION

In this chapter, design, fabrication, and testing of a meso-scale EHD pump that will be an essential component of a cryogenic spot cooling system is presented. In the next chapter this pump will be used in a closed loop experimental facility to investigate the feasibility of EHD pumping of liquid nitrogen with application to spot cooling of sensors and detectors. The ultimate goal of this effort is to develop an efficient heat rejection unit for cryogenic cooling with ultra low parasitic thermal, mechanical, and electromagnetic noise, as required by special applications such as sensors and detectors.

In an effort to demonstrate liquid nitrogen's pumping capability, a meso-scale EHD pump was designed and fabricated to ensure compatibility with cryogenic operation requirements. First, static pressure tests at room temperature were performed with a one-stage EHD pump using R-134a as working fluid, and were followed by testing of a three-stage pump with a 3M electronic cooling fluid. Finally, closed loop tests were performed using R-134a. These tests were performed to determine the pumping capability of the EHD pump at room temperature conditions. The tests prepared us to characterize the pump performance and identify critical operation parameters before testing the pump in a much more challenging environment involving cryogenic liquids pumping.

5.2 THEORETICAL BACKGROUND ON ELECTRODE DESIGN

In liquids with very low conductivity a quasi-universal charge generation mechanism is proven to exist (Castellanos, 1998). The mechanism consists of an ion generation process at the metal-liquid interface, followed by the ions being accelerated by the

Coulomb force to the opposite polarity electrode. These ions provide momentum, or "drag" along the rest of the fluid. For asymmetrical configurations in the regions with points of high curvature, the electric field intensity is high, and the ion injection process occurs. The charged particles move in a jet-like motion towards the oppositely charged electrode. The pumping force is very much dependent on the electric (conductivity) and fluidic (viscosity, density etc.) properties of the liquid.

From the foregoing introduction it is clear that electrode design plays an important role in designing an ion-drag EHD pump. The design should balance two counteracting trends: the filtering effect of the electrode on the fluid flow, and the efficiency of the ion injection process in the bulk fluid, which depends on the location of the active tips on the charged electrode. Pumping is achieved if the electrical shear stresses are higher than the viscous shear stresses. If the fluid flow entering the pumping section is in a laminar fully developed regime, which is usually encountered in this kind of system, then the shear stress is the greatest at the wall and decreases linearly towards the centerline. Ion injection occurs at the tip of the charged electrode where the radius of curvature is the highest and the electric field intensity is maximum. The ions will then be attracted (due to the Coulomb force) to the collector, presenting a jet-like behavior. Thus, the locations at which the ions are generated and to which they are accelerated play an important role in determining overall pumping efficiency. If the ion injection location is too close to the wall, most of the momentum from the EHD jets will be transferred to the wall. But if it is too far from the wall, the EHD momentum transfer efficiency will be lower, since the jets will act in a region where the shear stress is lower than at the wall.

5.2.1 The Earlier Work

In the literature, several different types of electrode designs have been proposed: grid type emitter and collector, drilled holes plate electrode, ring electrodes, needle-type, and screen with needles.

Stuetzer (1959) pioneered the ion-drag pressure generation by offering a model for the ion-drag EHD pumping of different electrode geometries. He considered three geometrical configurations: plane electrodes (in Cartesian coordinates), a cylindrical geometry (in cylindrical coordinates), and a needle type geometry (in spherical coordinates). He derived the pressure generation for the ion-drag pump and showed that (after a set of simplifying assumptions) the pumping head is proportional to the electrical permittivity of the fluid and the maximum electrical field strength in the system. He also derived shape factors for the three geometries mentioned above. For the parallel plates the shape factor is 1; for the concentric cylinders the shape factor is twice the logarithm of the ratio of the radii of the collector to emitter; and for the needle (spherical) geometry the shape factor is proportional to the ratio of the radii of the needle emitter tip and the collector. He concluded that substantially higher EHD drag pressures could be obtained with the needle geometry based on the maximum electric field strength obtainable in the three cases.

Sharbaugh and Walker (1985) designed and evaluated an ion-drag pump. They used a wire mesh emitter electrode with a number of needles oriented towards a wire mesh collector. They observed that using a non-polar fluid (such as transformer oil) for two parallel screens with no sharp points a small pumping effect was obtained. They assumed that most of this pumping effect was likely due to solid contaminants in the fluid, such as

dust. As points were introduced on the emitter, the pumping became steady, and useful velocities were reached. They concluded that inclusion of sharp points increased the pumping effect.

Barbini and Coletti (1995) studied the influence of the electrode geometry on ion-drag static pressure. They compared the theoretical relations for EHD pumping with the experimental data. They used two types of emitter electrodes: a drilled disk electrode and a screen electrode. They found that the screen electrode performed better and that the theoretical relations were not fully in agreement with the pumping results. Therefore, more complex processes and effects, such as charge injection at the liquid–solid interface, had to be taken into account to describe the ion-drag pumping phenomenon.

Bryan and Yagoobi (1990, 1992 and 1994) presented an experimental investigation of an ion-drag pump in a vertical and axisymmetric configuration. To minimize the filtering effect of the mesh electrode they used needles attached to a ring shaped emitter, which minimized the hydrodynamic drag on the flow. They analyzed the two-dimensional flow field generated by a single stage ion-drag pump, and compared the model with the experimental results for a two-mesh electrode pump configuration.

Castaneda and Yagoobi (1991) used thirteen electrode pairs to pump Refrigerant-11. The electrodes consisted of simple tin-copper wire rings pressed into grooves cut in the inside surface of a Lexan tube.

5.2.2 The Electrode Design

Based on theoretical analysis and extensive search of literature for previous work in this area, the final electrode design selected for the present study involved a ring shape emitter with needles around the circumference and a ring shape collector. The design

specifications required it to fit inside a 3/8'' pipe and to have good pumping performance. The emitter was made out of stainless steel 316. First, a blank piece of steel with a conical shape on the internal surface and a cylindrical and conical shape on the external surface was obtained. Then, an EDM machine was used to cut 30 teeth with a distance of 1.5 mm from the tip to the base plane. The emitter geometry and dimensions are presented in Figure 5.1. The geometry was designed to minimize the flow filtering effect and to inject ions in an efficient manner.

The collector consisted of a 316 stainless steel ring (see Figure 5.2), which was placed coaxially with the emitter in the flow path. Photographs of the emitter are presented in Figure 5.3. Small irregularities are present along the edges, but the tips, which are the most important active part of the electrode, are sharp and point in the pumping direction, acting as good field intensifiers.

5.3 SINGLE-STAGE EHD MESOPUMP

5.3.1 EHD Pump Design

The overall pump design (first generation) is shown in Figure 5.4. The main issues concerning the EHD pump design are the electrical and pressure fittings, which must be compatible with the cryogenic temperatures and high pressures that the pump is required to withstand. Three Teflon PTFE cylindrical parts (labeled as Parts 1, 2, and 3 in Figure 5.4) were mounted together to ensure the electrical insulation between the emitter (Part 5) and collector (Part 4) and between the electrodes and pump case (Part 6). The main design difficulty was producing a high-voltage experimental apparatus in which only ultra low currents (on the order of micro amps and lower) are flowing through the system.

The Teflon PTFE components were stacked together and placed in a stainless steel tube (Part 6 in Figure 5.4). The CAD drawings of the Teflon parts are presented in Figure 5.5 to Figure 5.7. The Teflon parts were machined from a cylindrical rod that was bored through to obtain a 3/8" inner diameter. They were then machined such that they could be connected to the electrodes. The electrode connection was one of the most challenging tasks.

In the last version of the design, the electrodes were connected to the power supply via two electrode fittings obtained from Connax, Inc. The electrodes were selected to withstand pressures of up to 350psi and voltage up to 25kV. The electrodes were placed inside the Teflon parts (see Figure 5.8). Upon mounting the Teflon parts, the electrodes were pressed on a very thin wire, which makes the electrical connection. The wire was soldered to a small, circular stainless steel sheet. A small spring connects electrically to the fittings conductor, passing through the Connax fitting and pressing on this metal sheet when the fitting was tight. This design was the result of a few iterations. The previous designs suffered from a critical issue, which was arching (sudden electrical discharge) between the conductor found on the high voltage path and the pump casing, which was grounded. Although in most of the cases the arching was limited by our design efforts, its occurred frequently enough to prevent high voltage from being obtained on the emitter, which is critical in obtaining a pumping effect.

The pumping unit design provides easy disassembling to allow the testing of different electrodes. The distance between the tips of the emitter and the collector was 2.5 mm, and there are 4.0 mm between the base of the emitter needles and the collector.

5.3.2 Static Pumping Tests Using R-134a

5.3.2.1 Experimental Set-up

The first set of experiments consisted of static (no flow, open loop) pumping tests with R-134a. This refrigerant is easy to handle, is affordable, and has relatively good electrical properties (Table 5.1). These experiments were performed in a pressurized transparent glass cylinder chamber. The test section consisted of the pumping stage connected to a graduated tube. Thus, the relative liquid column height was used to measure the pumping head. A schematic of the experimental set-up for the R-134a EHD pumping tests is shown in Figure 5.9. The pumping section was connected to the high voltage power supply through a special high voltage connection. A 0-30kV Glassman high voltage power supply is used to provide the high voltage. The collector and the chamber metallic parts are grounded.

Figure 5.10 presents the testing set-up. The small, enhanced tubes in the left part of the picture are part of a water-cooled loop, which served as condenser. The pumping section is placed in a vertical position inside the chamber and is connected to a graded tube. A bare wire connects the ground electrode to the condenser, which is grounded. The high voltage wire is passed through a feedthrough, present in the right side of the picture, and then connected to the power supply. An absolute pressure transducer was used to monitor the pressure during charging and the state inside the chamber such that a constant refrigerant level was maintained.

5.3.2.2 Experimental Procedure

A typical experimental set began by first assuring proper electrical connections between the electrodes and the high voltage gear ware. To test the electrical connections, high voltage was applied between the emitter and collector until a small spark occurred.

Sparking voltage corresponding to about 3kV/mm in air indicated that the electrical connections were properly established.

The chamber was then closed and charged with R-134a to a reference steady- state level. A DC high voltage was applied to the pump. At about 6kV a visible pumping effect was observed, and once the current became stable, the pumping height, current and voltage were recorded. Figure 5.11 shows the pumping effect at about 16kV when the height was 18mm, which represents around 210Pa.

5.3.2.3 Data Reduction and Uncertainty Analysis

The static pressure generated by the pump was calculated from the respective liquid column height measurements. The uncertainty of the pressure measurement was estimated, based on the height reading uncertainty of 1mm, to maximum ±12 Pa.

5.3.2.4 Results and Discussions

The static pumping tests performed with R-134a used a negative polarity for the emitter, and the collector was grounded. The applied voltage was varied from 0 to 25 kV.

The liquid column height and pumping head results are presented in Figure 5.12. A pumping head of 144 Pa was generated with a voltage of 15 kV. The power consumption was 550 mW. The power consumption varied between 0.1-0.5 W (Figure 5.13). A measurable pumping head was detected at about 6 kV and increased almost linearly with applied voltage. Above 15 kV the pumping was not possible due to the fact that the refrigerant was close to the vapor saturation state, and bubbles were generated as the voltage was further increased. The presence of the bubbles decreased the electrical resistance of the refrigerant, and thus unstable current and sparking occurred. The static pressure experiments achieved their purpose, which was to obtain a first-performance assessment of the pumping capability for a given electrode design and working fluid.

Moreover, any instability in the electric field and/or electrode connections and the working fluid would be normally revealed during such experiments, so that appropriate corrective action can be taken before the closed loop experiments.

5.4 THREE-STAGE EHD MESOPUMP

A three-stage EHD pump was designed, fabricated and tested to verify the possibility of increases in pumping performance using multi-staging. The design requirements for the multi-stage pump were similar to the ones set for the one-stage system. These efforts were undertaken after the liquid nitrogen tests using the one-stage pump presented in the next Chapter were performed. They are meant to demonstrate ways to increase the pumping capability in case the system requires it.

5.4.1 Pump Design

The three-stage pump has the same overall dimensions as the one-stage pump, since it uses the same casing. The three Teflon parts were changed to accommodate three pairs of electrodes, which are equally spaced at about twice the electrode gap. The electrode gap was maintained at 2.5mm and thus the stage spacing is 5mm. As in the case of the single-stage pump, one of the most important issues in designing the pump is the electrode connection. The solution here is similar to the single-stage pump. Each electrode sits on a thin wire, which passes through the Teflon insulation and connects to a thin metal sheet. The wires coming from each electrode with the same polarity are soldered to the same sheet. A small spring connects to the Connax fitting conductor on one end and on the other pushes upon the metal sheet. The mounting of the stages is in parallel, which provides the same voltage to each stage.

5.4.2 Three-Stage Pump Tests with 3M Fluid

5.4.2.1 Experimental Set-up

The working fluid in these tests was a 3M fluid, which has relatively low vapor pressure. This allowed us to perform experiments in a set-up open to atmosphere. The experimental set-up consisted of a liquid container inside which the pump was placed in a vertical position. The same high voltage power supply was used to apply a negative voltage to the emitter. The liquid column height was measured using the same graded tube. The experimental procedure was similar to the previous test. The measurement uncertainty is the same as in the previous tests.

5.4.2.2 Results and discussion

During these tests the voltage was varied between 0-30kV. The pressure versus voltage is presented in Figure 5.14 for three different tests. The results show a good repeatability. The pumping started in this case at about 15kV and the pressure head followed an almost quadratic behavior with the voltage. The maximum pressure head was reached at about 30kV and had a value of about 2000Pa. The pressure head and the power consumption are represented in Figure 5.15. The power consumption was in the same range as the previous experiments. The electric properties of the two fluids (see Table 5.1) used in the two tests presented above are relatively similar; this is why the pumping currents are also similar, which explains the power consumption levels' similarity.

Table 5.1 Thermophysical properties of the liquids

Thermophysical Property	HFE-7100	R-134a
Boiling Point (^{o}C) (at 1 kPa)	61	-26
Liquid density (kg/m^{3}) (at 1 kPa)	1402	1207
Liquid kinematic viscosity (cSt)	0.38	0.166
Liquid specific heat (J/kg-K)	1253	1425
Dielectric strength (kV/mm)	11	NA
Dielectric constant	7.40	~ 7
Saturation Pressure (kPa) at Room temperature (25 ^{o}C)	27	665

The tests performed with the three-stage pump show that higher pressure heads can be obtained using multiple-stage pumping. The comparison between the single-stage and the three-stage experiments are valid, since, as shown in the introduction, the pumping head depends mainly on the electric field strength and the dielectric constant of the fluids used. Since the dielectric constants are similar and the pump geometry is the same, the differences in the performance between the two experiments are due to the multi-staging. At about 15 kV the single-stage pump provides about 160 Pa, while the three-stage pump reaches 200 Pa. Although comparison at higher voltages was not possible due to the lack of data for the single-stage pump, higher differences are expected at higher voltages.

5.5 EHD PUMPING LOOP

5.5.1 Loop Design

I designed a flow loop in order to determine the loop pumping performance of the EHD meso-scale pump. The loop was built in the university machine shop facility. The flow loop design for conducting the EHD pumping experiments is shown in Figure 5.16. The closed loop was designed to allow conducting single-phase liquid nitrogen tests. The loop can withstand charging pressures on the order of 26 bars (up to 400psi), and allows efficient fluid cooling down to liquid nitrogen temperatures. The loop consists of a 3/8 inch copper pipe liquid line (part 4 in Figure 5.16) that connects the EHD ion-drag pump (part 1) to a copper block 5×1.25×1.25cm (2×0.5×0.5 in) on which an electrical (resistive) heater is attached to simulate the thermal load (part 2). Another copper block heat exchanger is connected to a cryocooler, which provides the cooling load (part 3). The loop is suspended on four G-10 supports (part 5) to minimize the conductive heat losses. A two-phase accumulator (part 6) connected to the main loop is used to provide temperature and pressure stability and controllability. The loop is placed inside a copper shroud to minimize radiation heat transfer (part 7). Some of the requirements in designing the cryogenic loop included relatively small dimensions (meso-scale), the ability to withstand high pressures and to allow good grounding and electrical isolation of the high voltage line. More details about the cryogenic loop design can be found in the next chapter.

The actual loop in the preliminary stages of construction and after the R-134a tests is presented in Figure 5.17 and Figure 5.18. The overall dimensions of the loop are 10×22.5cm (4×9 inches). The EHD pump is connected to the 3/8 in tubing through a set

of copper gasket-sealed flanges, acquired from Duniway Corp., called Conflat flanges. The flanges were modified, so they could be brazed to the pump casing and the loop tubing, and were bolted together. The pump casing length was about 6.25cm (2.5 inches), and the diameter is about 2.5cm (1 inch).

The tubing of the loop is bent into a curved rectangular shape with 2.5cm (1 in) radius turns to minimize flow resistance. Two 1/16" tubes are connected to the flow loop. One of these tubes is used to connect the two-phase reservoir to the main loop, and the other is attached to the charging port. Both lines pass through the cryocooler interface, such that the two fluid lines are cooled-fed. The purpose of the cold feeding is to provide cooling to the reservoir and to limit the conductive heat gains through the charging line, connected to the exterior, which is at a high temperature.

The pumping direction is from left to right in Figure 5.17, which means that the liquid leaving the pump will go through the hot side heat exchanger (part 2 in Figure 5.16), through the hot line, and then will be cooled in the cold side heat exchanger. The pump was placed at the middle of the cold line to ensure that only liquid nitrogen would flow through the pump.

All the system components had to be vacuum compatible since during the cryogenic experiments the loop was placed inside a vacuum chamber. Thus, a vacuum-compatible pressure transducer was used in our experiments. The pressure transducer ports were connected through some holes made in the Conflat flanges downstream and upstream of the EHD pump using 1/16 piping (Figure 5.17).

The differential pressure (DP) transducer is positioned parallel to the line between the inlet and outlet of the EHD pump. For the R-134a tests a Sensotec FP2000 (0-10in)

pressure transducer was used. The measurement accuracy of the device is given as 0.1% of full scale, which means 2.5 Pa. An absolute pressure transducer was also used for system pressure measurement during the charging and operation.

The two-phase reservoir is suspended by a G-10 support to minimize heat losses by conduction (Figure 5.17). The two-phase reservoir is used to provide controllability to the loop temperature. The reservoir exchanges liquid with the loop through the connecting line. The reservoir temperature can be controlled by means of a thermofoil heater, which is attached to the reservoir. When the loop and the reservoir are at the same temperature due to buoyancy, bubbles can travel along the connecting line to the reservoir. The reservoir was connected to the loop just before the cold side heat exchanger to take advantage of this bubble filtering effect.

5.5.2 Loop Tests Using R-134a

The first set of experiments conducted using the EHD pumping loop used R-134a as working fluid. The experiments were designed to test the pumping capability of the EHD pump in the closed loop configuration.

5.5.2.1 Experimental Procedure

First, the loop was cleaned using alcohol and purged with refrigerant. Next, the loop was charged with R-134a to the saturation pressure corresponding to the room temperature. The charging mass was measured by weighing the loop to verify that the loop was fully flooded. The steady state differential pressure was measured and recorded as a reference value. The power supply was switched on, and the voltage was gradually increased. At each voltage, the steady state current and differential pressure were recorded.

5.5.2.2 Experimental Results

The pumping head results as a function of applied voltage are depicted in Figure 5.19. The applied voltage varied from 0 to 23 kV. The pumping started at about 2.5 kV and continued to increase to a pressure of 300 Pa at an applied voltage of 22 kV. The corresponding pressure versus power consumption is presented in Figure 5.20. The power consumption, for the loop tests with R-134a using the single-stage pump, was reduced comparatively to the static pumping tests. One explanation for this reduction could be the difference in the level of impurities present in the working fluid during the static pumping experiments, which was higher than the one found in the loop tests. This would mean that the impurity current was lower in the case of the loop tests, which makes the power consumption lower. Also, a lower level of impurities may explain why the starting voltage in the loop tests was lower than the static pumping tests. The impurity current consisting of both polarity charge carrier presence appeared inside the liquid when the voltage was applied and had no pumping effect. As the impurity level was decreased, in the case of the loop tests, the ion driven flow occurred at lower voltages.

5.6 SUMMARY

This chapter presented the design, fabrication and testing of a novel EHD pump which will be used to pump liquid nitrogen. The designs of a single-stage and three-stage EHD pumps were presented. A set of experiments was performed to determine the feasibility of using the pump for EHD pumping. A single-stage pump was tested in a static pumping configuration using R-134a refrigerant. The results showed that the pump could provide a pumping head of about 140Pa at an applied voltage of 15kV passing the feasibility test. Next, the three-stage pump was tested using a dielectric fluid provided by 3M (HFE 7100), which has the advantage of allowing experiments to take place in room conditions.

The results showed the potential of improving the pumping performance using multiple stage pumps. A closed loop was designed and built with the final aim of using it in EHD pumping tests with liquid nitrogen. The closed loop tests were performed using R-134a. The results showed that the developed EHD pump can be successfully used in closed loop EHD pumping experiments.

The work presented in this chapter shows that the original design EHD pump can successfully be used in vertical and closed loop pumping. These EHD pumping tests also prove the feasibility of an EHD pump for use in heat transfer devices.

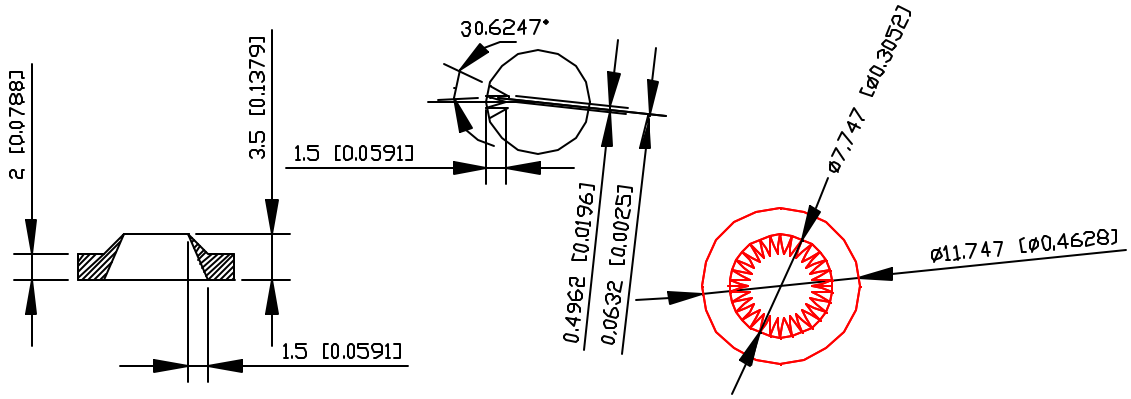

Figure 5.1 CAD drawing of the emitter (dimensions in mm [inches])

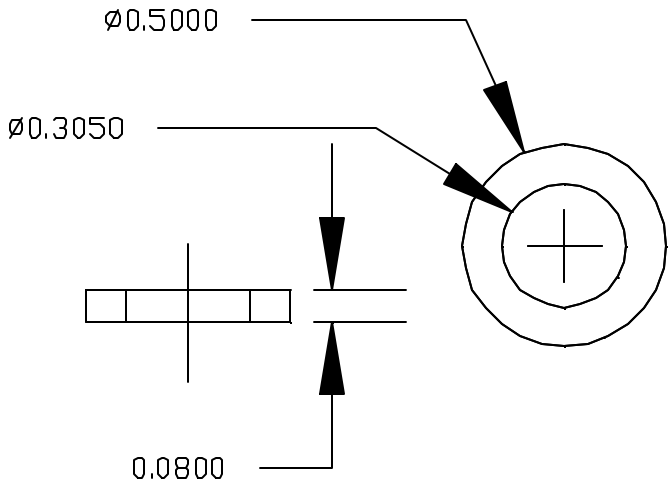

Figure 5.2 CAD drawing of the collector (dimensions in inches)

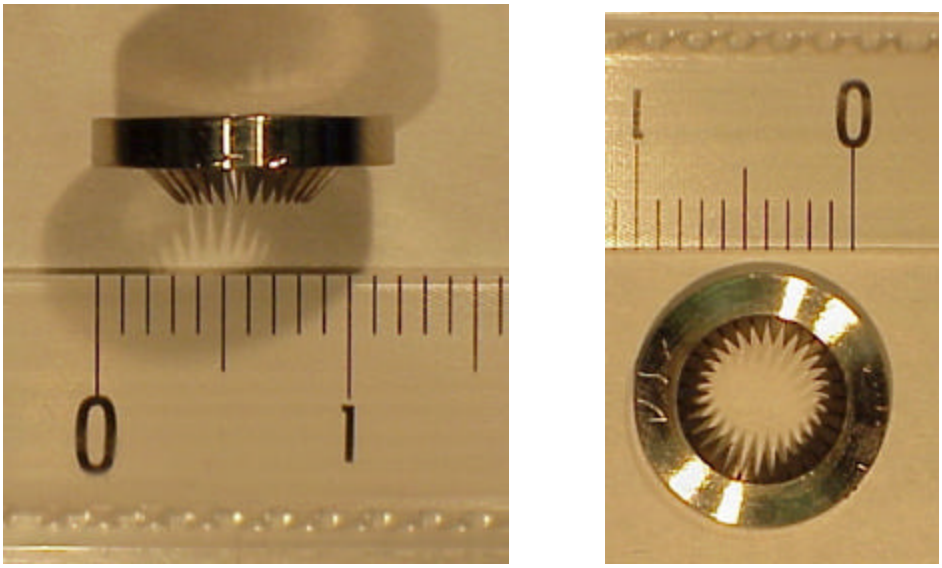

Figure 5.3 Photographs of the emitter

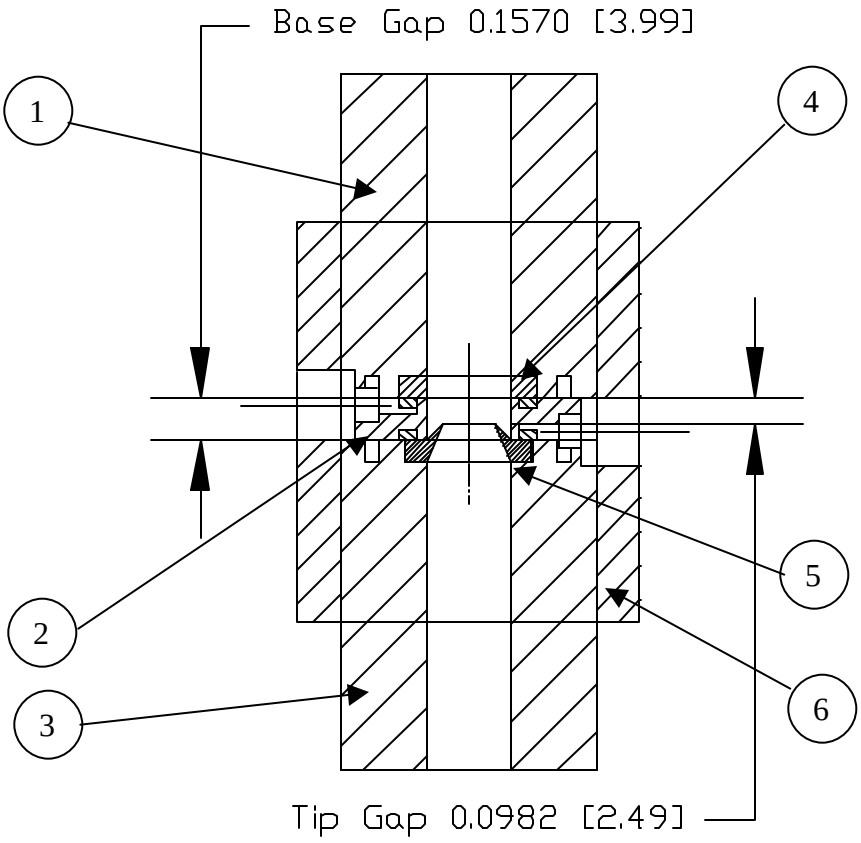

Figure 5.4 Schematic diagram of the pump and its components

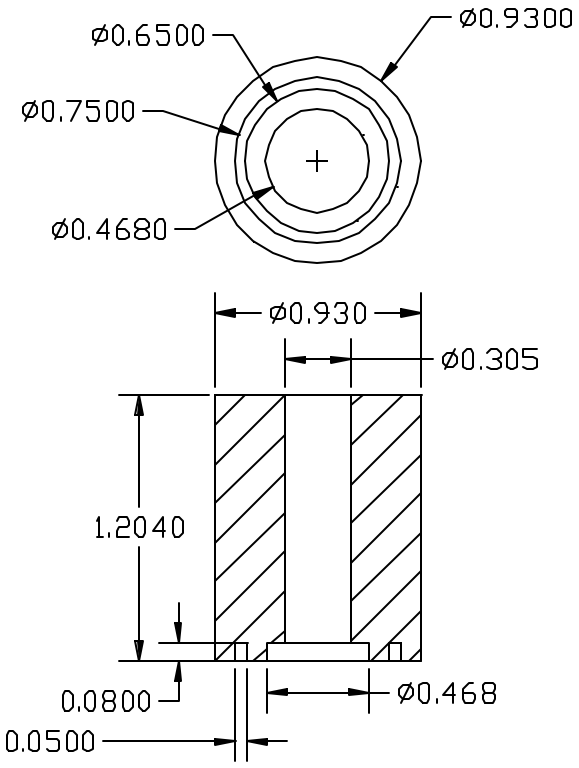

Figure 5.5 CAD drawings of the Teflon part for the emitter (all dimensions are in inches)

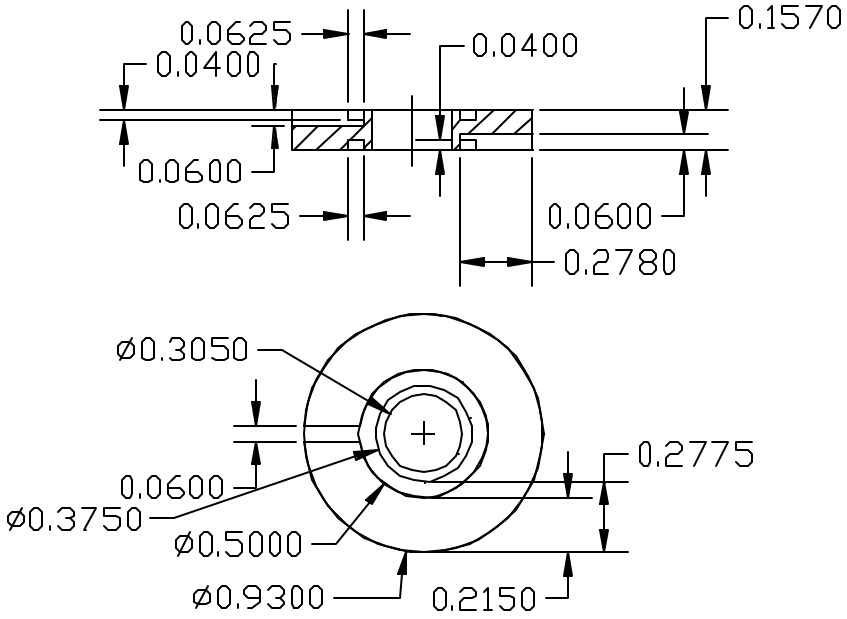

Figure 5.6 CAD drawings of the central Teflon part (all dimensions are in inches)

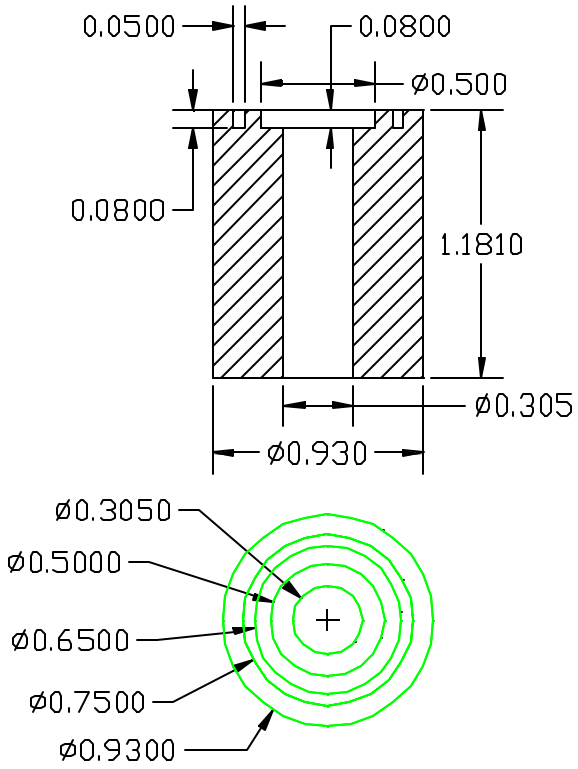

Figure 5.7 CAD drawings of the Teflon parts for the collector (all dimensions are in inches)

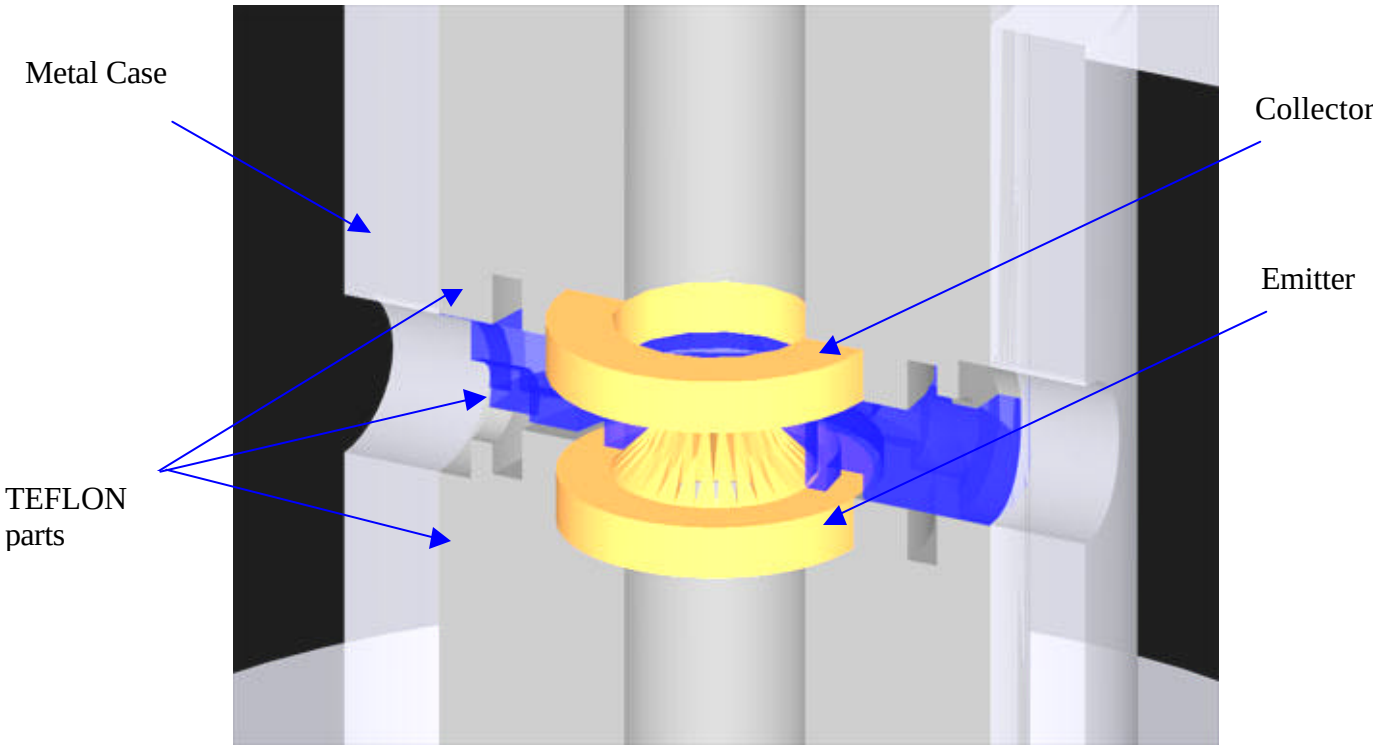

Figure 5.8 A CAD drawing of the EHD pump

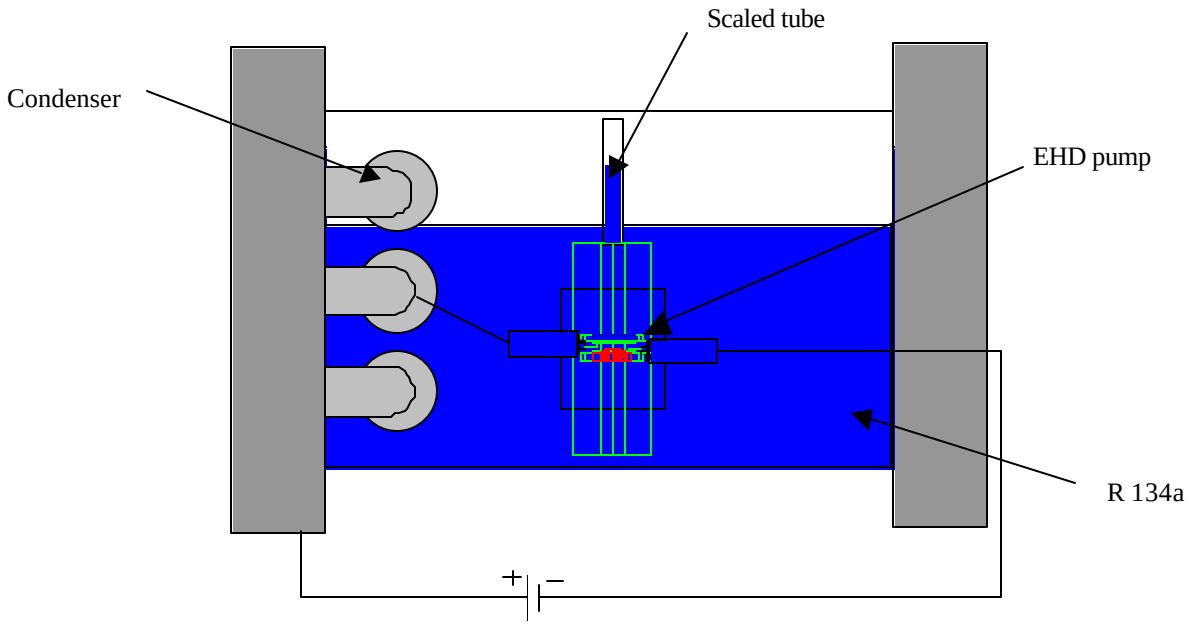

Figure 5.9 Schematic diagram of the R-134a test set-up

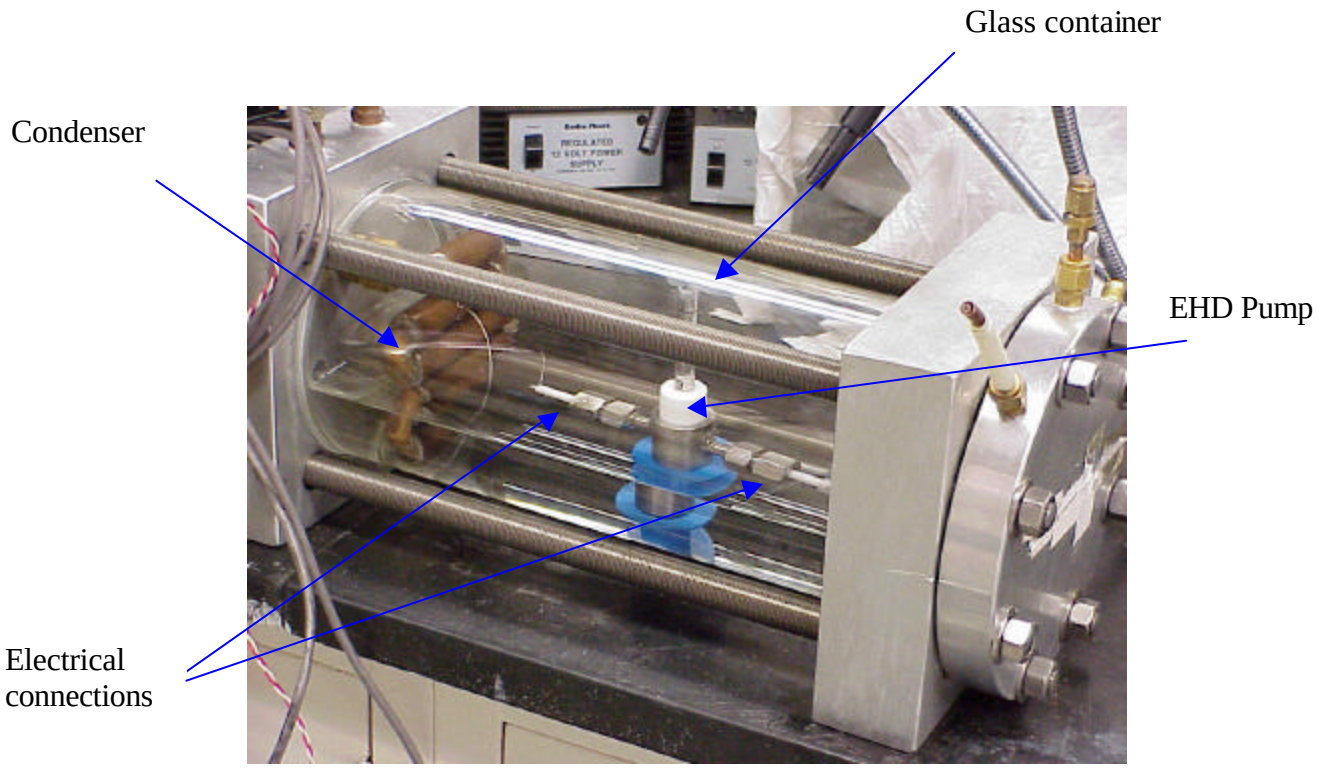

Figure 5.10 A photograph of the R-134a static pumping setup

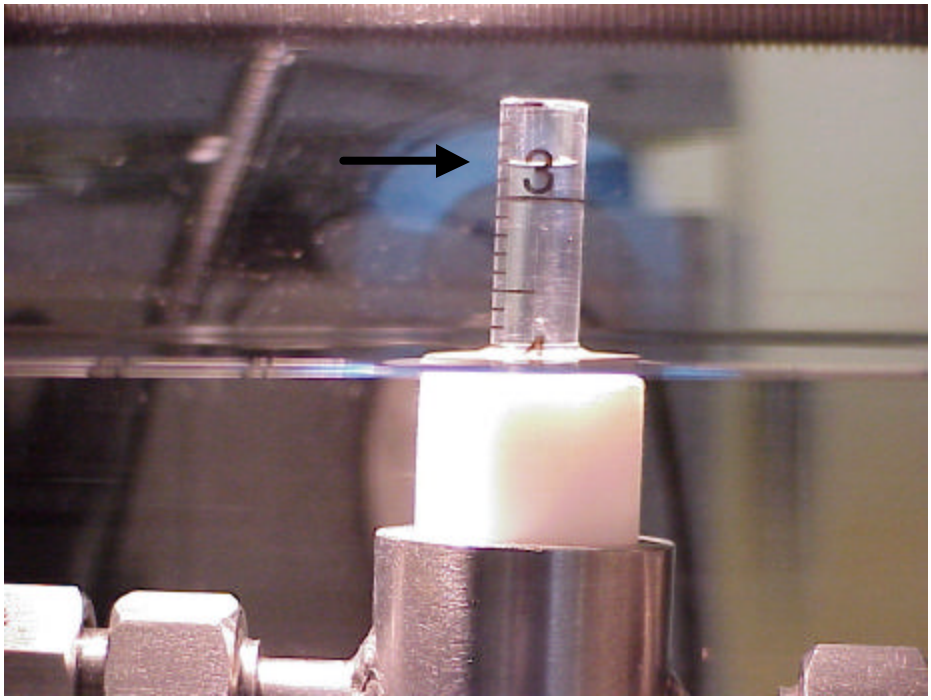

Figure 5.11 A photograph of the static pressure test

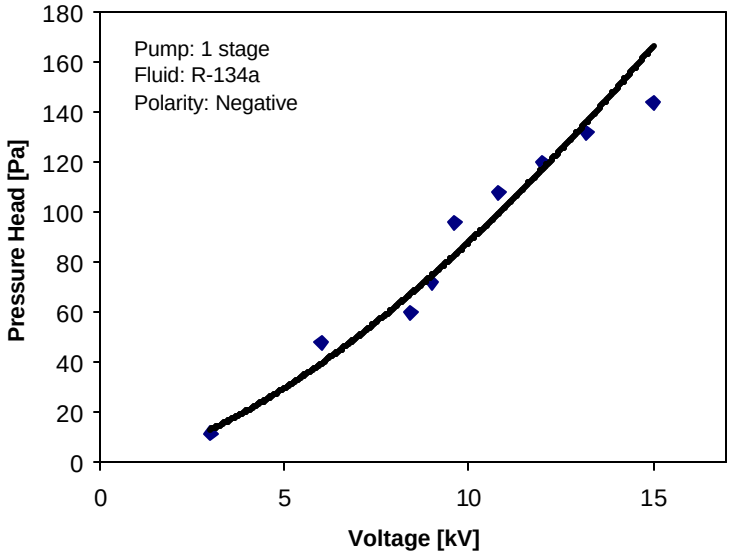

Figure 5.12 Pressure head versus applied voltage for the one-stage R-134a static pressure tests

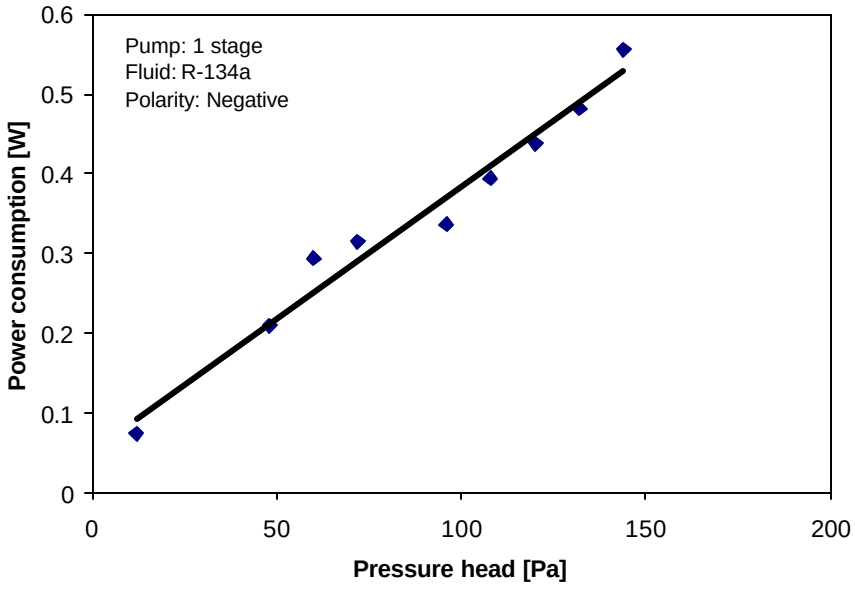

Figure 5.13 Pressure head versus power consumption for the one-stage R-134a static pressure tests

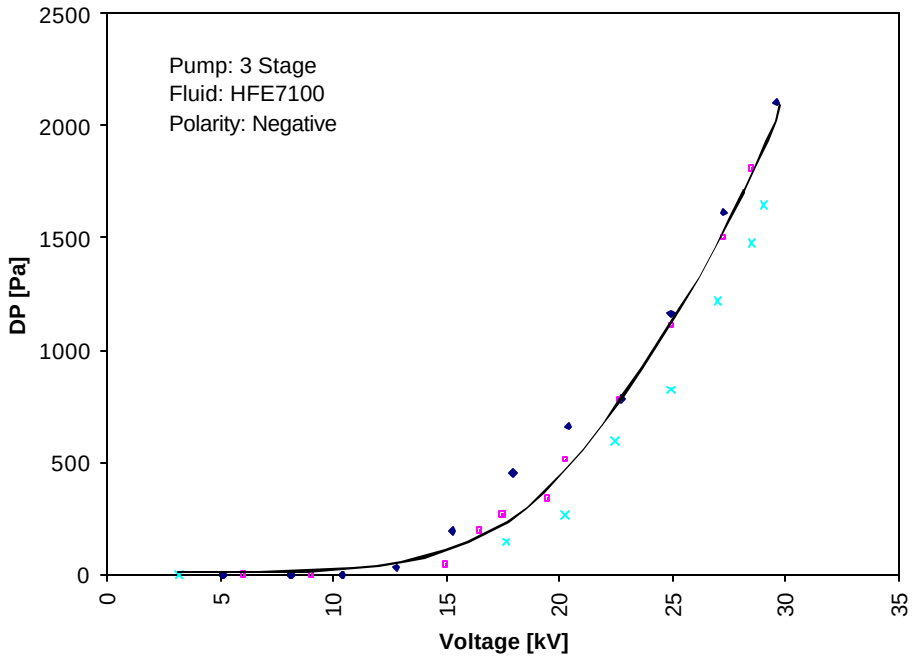

Figure 5.14 Pressure head versus applied voltage for the three stage HFE7100 fluid tests

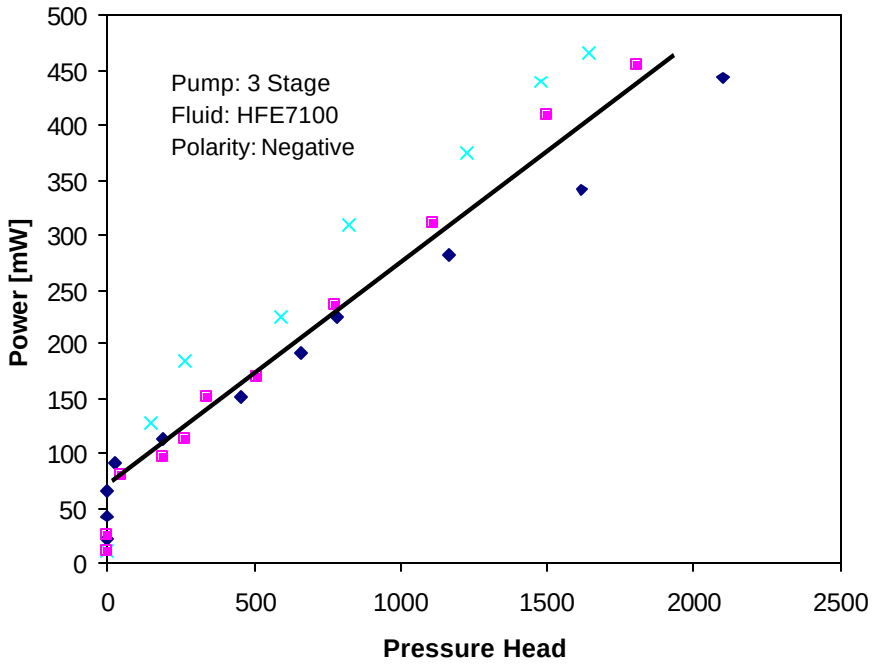

Figure 5.15 Power consumption versus pressure head for the three stage HFE 7100 fluid tests

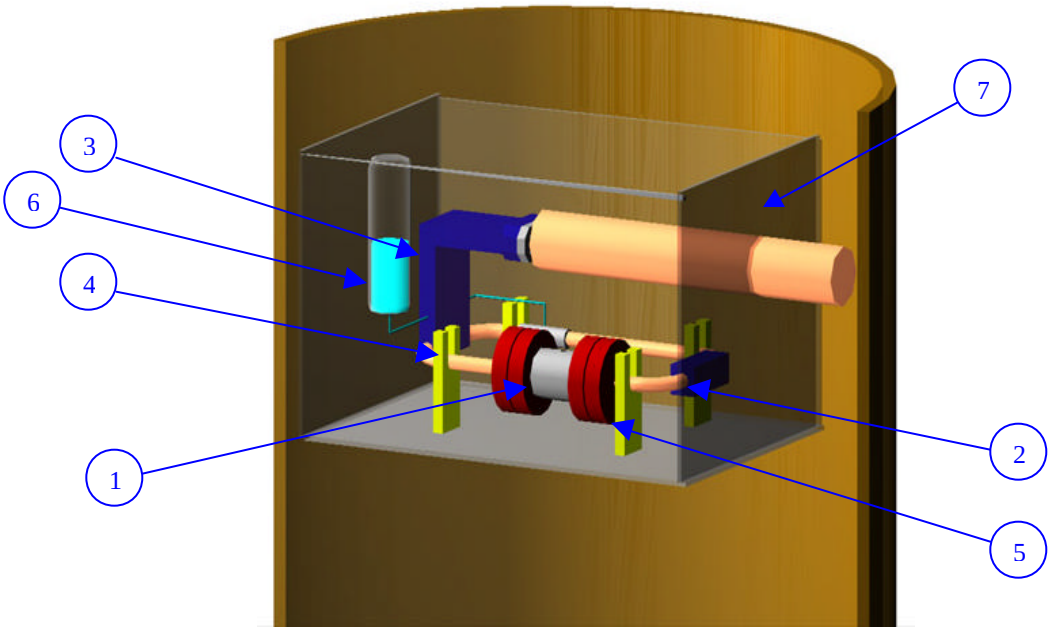

Figure 5.16 CAD drawing of the flow loop (1 - EHD pump, 2 – heater, 3 – cryocooler interface, 4 – 3/8 pipe loop, 5 – G10 supports, 6 – two-phase reservoir, 7 - shroud)

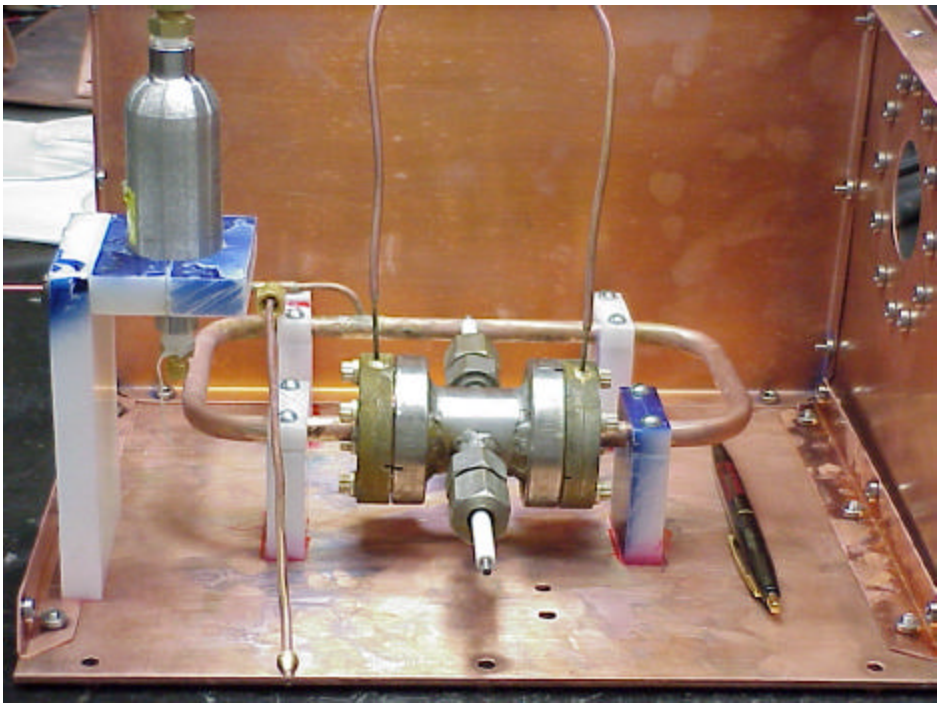

Figure 5.17 A photograph of the front view of the loop during construction

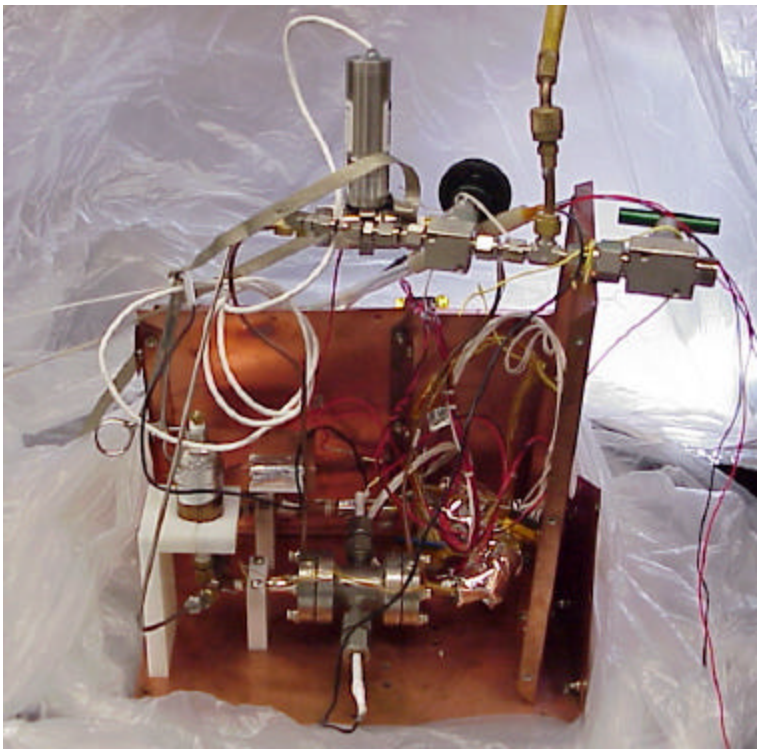

Figure 5.18 A photograph of the loop used for the R-134a pumping tests

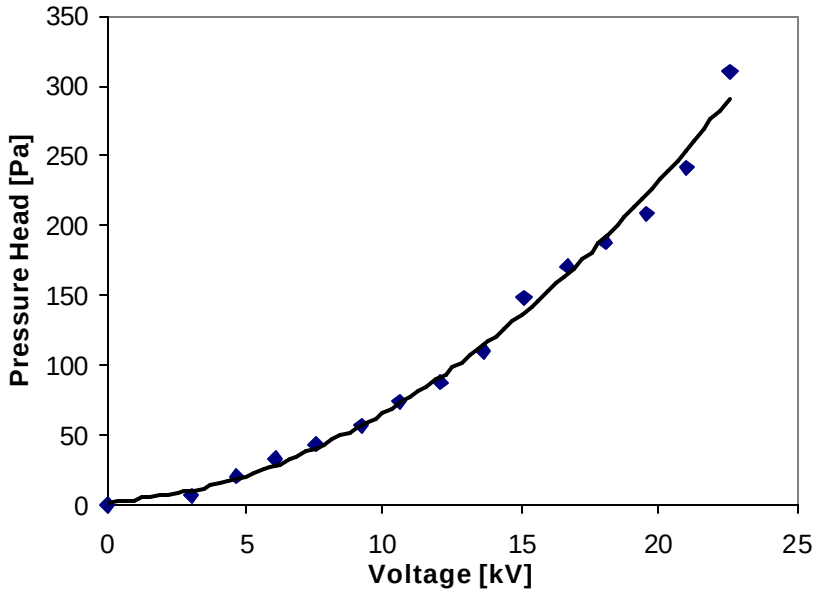

Figure 5.19 Pressure head versus applied voltage for the R-134a loop pumping tests

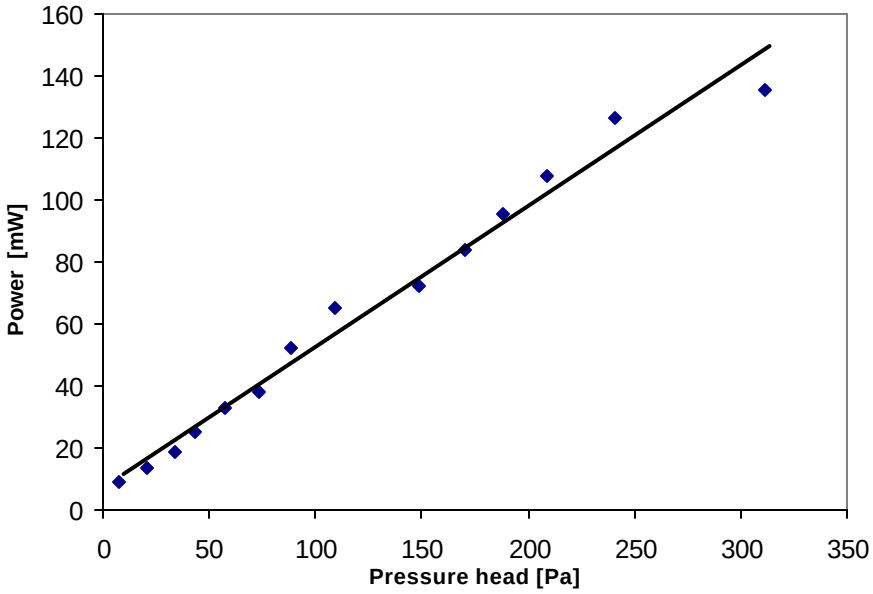

Figure 5.20 Power consumption versus pressure head for R-134a loop pumping tests

CHAPTER 6 EXPERIMENTAL APPARATUS, DESIGN AND TESTING PROCEDURE FOR THE EHD-PUMPED CRYOGENIC COOLING LOOP

6.1 INTRODUCTION

A potential application for EHD pumping that has not been explored by the scientific community is the pumping of cryogenic dielectric liquids, which are widely used for the cooling of cold electronic devices. Although the room temperature liquid ion-drag pumping relies mostly on the fluid ionization by the electric field, for cryogenic liquids ion injection processes are expected to be the main provider of charged particles for EHD pumping. Lower currents are expected for cryogenic liquids pumping since they exhibit lower conductivities. The operating temperature is another reason for which pumping current are lower. It is well known that the ion injection process is dependent on temperature thus for cryogenic temperatures the ion injection processes are weaker. Still clever emitter designs should overcome this problem.

An important advantage of cryogenic liquid pumping is an improved stability with respect to the room temperature liquids. Room temperature liquids consist of relatively complex molecules while most of the cryogenics have very simple molecular structures. Although the long-term effects of electric fields on liquid molecular structure is not yet fully understood or reported, basic reasoning leads us to assume that the electric field would not exert any harmful effects on cryogenic liquids. Most cryogenic liquids exhibit relatively simple and stable molecular structures, most being mono- or diatomic fluids. Although the electric fields used in this application are far below the levels needed to

break the molecules, in the event of a molecular breakdown, the atoms would recombine into their initial molecular structure.

In ion-drag pumping the force acting on the charged fluid molecules is known as the EHD body force (Melcher (1981)):

$$\vec{f}_e = q\vec{E} - \frac{\varepsilon_0}{2} E^2 \nabla \varepsilon_r + \frac{\varepsilon_0}{2} \nabla \left(E^2 \rho \frac{d\varepsilon_r}{d\rho} \right) \tag{6.1}$$

where q and ρ are the charge and mass density of the fluid, *E* is the electric field intensity, ε_0 is the dielectric permittivity of the vacuum, and ε_r is the dielectric constant of the fluid. In a liquid phase fluid, the last two terms can be neglected, so the pumping force in the fluid is primarily related to the Coulomb force:

$$\vec{f}_e = q\vec{E} \tag{6.2}$$

Pumping in a single-phase fluid is possible when charge is generated in the fluid. Ion injection occurs through ion generation at the metal-liquid interface. In the presence of a strong enough electric field, a mechanism similar to corona emission occurs, producing ions inside the liquid (Hernandez-Avila et al (1994)). This is achieved with the use of electrodes with sharp points or edges, where due to their small radius of curvature, very strong electric field intensities are obtained such that ionization of the dielectric fluid takes place.

This chapter presents the experimental set-up and the tests that were performed to determine the feasibility of using an EHD pump to drive liquid nitrogen in a cooling loop.

6.2 LIQUID NITROGEN, STATIC PUMPING TESTS

A test section was fabricated for the static EHD pumping tests with liquid nitrogen. A transparent housing for the two electrodes was built from acrylic plastic. The pump was

connected to two acrylic tubes. Wires were soldered to the emitter and the collector, and these wires were passed through two small holes made in the acrylic wall that were then sealed with silicone glue (Figure 6.1). The test section was placed in a styrofoam container, which was filled with liquid nitrogen. Initially, violent boiling occurred, but after some time the system reached a steady state and stable pumping was obtained. In order to measure the static pressure head, the upper tube was etched with markings. On applying the voltage, the EHD pumping head level was obtained by measuring the relative liquid column height (Figure 6.2). The applied voltage was between 0-26 kV. The test results, presented in Figure 6.3 and Figure 6.4, show the pumping head versus the applied voltage. Pumping started at an applied voltage of about 12 kV. The initial pumping head was around 2 mm (corresponding to a pressure of about 16 Pa) and increased linearly up to a value close to 16 mm (~125 Pa). The power consumption to generate the maximum pressure was about 0.5 W (Figure 6.4).

The static pressure tests with liquid nitrogen demonstrated that it was possible to pump liquid nitrogen using an ion-drag EHD pump. Also, relatively good pumping heads were obtained. Because the tests were performed in an open environment the liquid nitrogen was contaminated with dissolved oxygen and ice particles, which were entrained in the pumping action. Their presence made the pumping action relatively unstable for long periods of time. These problems will be avoided for the liquid nitrogen loop tests. Although the contaminates produce instability, they have a beneficial effect on the pumping since they consist of charged particles whose presence improves the pumping performance.

6.3 CRYOGENIC LOOP SET-UP

Following the directions provided by Mario Martins from the Thermal Engineering Branch at NASA GSFC I designed the cryogenic flow loop set-up. The flow loop used in the cryogenic tests was described in Chapter 5. The experimental loop set-up consists of the following components (see Figure 5.16):

(1) EHD pump;

(2) electrical (resistive) heater attached to the hot side heat exchanger;

(3) interface to the cold side heat exchanger;

(4) liquid line;

(5) G-10 supports;

(6) two-phase liquid accumulator;

(7) copper shroud.

The flow direction along the line, which contains the EHD pump, is from the cold side to the hot side heat exchanger. The EHD pump is placed on the cold liquid line to ensure that only liquid enters the pumping section.

To simulate a heat load a small thermofoil resistive heater (0.5" by 0.5") with a maximum heat output of 5 Watts was attached to the hot side of the heat exchange surface. The hot-side heat exchanger consists of a rectangular (0.5"×0.5"×2") copper block piece, which is bored to a 3/8" internal diameter pipe to allow fluid to pass through. The 3/8" piping is silver-brazed to the copper block (see Figure 5.16).

A similar block is used in the cold side heat exchanger. The cryocooler is connected to it through a copper interface (cryocooler interface), which is used to conduct the cold provided by the cryocooler to the heat exchanger and then to the fluid. The cryocooler

interface is connected to the cryocooler bracket by a bolted flange. Between the two matting surfaces a graphite sheet was used to ensure a low contact thermal resistance.

6.3.1 The High Voltage Connections

One of the most important issues in the cryogenic tests was the high voltage connection. The pump's internal high voltage connection was presented in the previous chapter. A Teflon insulated wire was soldered to the Connax conductor coming out from the pump. The wire was connected at the other end to a high voltage ceramic feedthrough, which allowed the high voltage connection to be passed through the vacuum chamber wall. Inside the chamber aluminum breed was used to shield the high voltage connection. First, more heat-shrinking insulation tubing was added to the high voltage connection wire to reach a thickness of about 2.5mm (1/10"). On top of this insulation the shield was added. The shield was insulated again using heat-shrinking tubing. The shield was connected to the ground (Figure 6.17). The purpose of the insulation is to screen the electromagnetic waves generated by the high voltage currents passing through the circuit. The electromagnetic interference was found to be very important, especially since the electromagnetic waves generated inside the chamber are reflected back inside the chamber by its metallic walls.

On the exterior of the chamber a well-insulated connection to the coaxial cable coming from the high voltage power supply was made.

The ground was connected outside of the chamber through a 5-pin feedthrough. Connections to the ground line were made from the loop pipe and shielding (Figure 6.17).

6.3.2 The Cooling System - Cryocooler

The cooling system consisted of a cryocooler and a vacuum chamber (Figure 6.9). The cryocooler has two stages. The first stage goes down to about 50K when no load is attached to it. A bracket is connected to the second stage (Figure 6.8). On the bracket two heaters are attached, which are used to control the amount of cooling provided by the cryocooler. The second stage provides about 30K when 15W are applied to the thermofoil bracket heater. In these conditions the bracket temperature is maintained at 73K. Thus, the maximum cryocooler cooling power is about 15W at a bracket temperature of 73K.

Both stages are installed inside the vacuum chamber. The vacuum chamber is capable of producing high vacuum levels on the order of 10^{-6} torr. First a mechanical pump is employed to create a vacuum in the order of 10^{-4} torr and then a cryopump takes over to go down to the abovementioned vacuum level. This deep vacuum ensures a very good thermal insulation medium, since no convective heat transfer to the chamber walls will be present.

The cryocooler and the vacuum chamber were controlled and monitored using the instrumentation installed in a control rack (Figure 6.9). The control system monitors the temperatures at the first and second stage of the cryocooler, in addition to the chamber pressure and the cryopump temperature.

The system was under sufficiently low vacuum such that heat transfer due to convection was negligible, thus radiation and conduction were the main heat transfer mechanisms.

During cooling it is important to conduct the heat from the loop towards the cryocooler. A few design features are meant to provide a good conduction cooling mechanism. The

main heat transfer path starts from the fluid passes through the loop pipe walls and the cryocooler interface and reaches the cryocooler. Additional cooling paths are provided which connect different points along the loop to the cryocooler interface. The reservoir and the pressure transducer, as well as the pressure taps, are connected to the cryocooler interface using copper tape.

The two-phase reservoir and the loop are suspended using supports made of a very low conductivity material (called G-10) to minimize heat losses by conduction to the shroud (Figure 6.7). To minimize the radiation losses two methods are used. First, most of the components (the EHD pump, hot side heat exchanger, reservoir, copper lines, the cold side heat exchanger, and the cryocooler interface) are covered with MLI (Multi Layer Insulation). The MLI consists of a set of 5-10 sheets of very thin aluminum foil specially coated to have a very low emissivity. These sheets are intercalated with fine plastic nets. The plastic net provides air gaps in between the layers, which ensures a high resistance to thermal conduction across the MLI.

Second, a shroud is used, which shields the radiation exchange between the loop and the chamber walls, which are at room temperature. The shroud consists of a cage built from copper sheets (Figure 6.6). The shroud is connected to the first stage of the cryostat. To ensure a relatively low radiation exchange between the loop and the shroud, the shroud is maintained at a temperature very close to the loop temperature by the first stage. Besides its role as a radiation shield, the shroud also plays a supporting role as a structural foundation, since all the system components are attached to the base plate.

The two-phase reservoir is used to provide more controllability to the loop temperature. The fluid exchanged with the loop is cooled in the reservoir's connecting line, which is

passed through the cryocooler's copper interface (Figure 6.7). Thus the reservoir is cooled two ways: by the tape attached to it and by the connecting line. A 5W thermofoil heater is attached to the reservoir, which is used to control the reservoir temperature.

6.3.3 Cryogenic Loop Instrumentation

The loop instrumentation had to comply with the vacuum chamber requirements as well as with the cryogenic temperature conditions. Selecting and calibrating it was an important challenge.

6.3.3.1 Pressure Transducers

Two pressure transducers were used during the experiments (Table 6.1). A differential pressure (DP) transducer is positioned in parallel with the line between the inlet and outlet of the EHD pump to measure the differential pressure generated by the pump. An absolute pressure transducer was used for system pressure measurement during the charging and operation.

Table 6.1: Locations of the pressure transducers

Device	Location
Differential Pressure Transducer	EHD Pump
Absolute Pressure Transducer	Charging Line

The differential pressure transducer was required to be vacuum-compatible, to operate under cryogenic temperatures, and to allow accurate differential pressure measurements in the range 0-5Pa. These requirements represented a serious challenge since they are not encountered in pressure transducer applications. A Validyne DP10, variable reluctance pressure transducer was finally selected and used in our experiments. The range of the pressure transducer is 0-860Pa (3.5 InH_2O) with a rated accuracy of 0.25% FS, which includes non-linearity, hysteresis and repeatability.

The pressure transducer was installed on the bottom shroud plate and connected to it using a copper bracket. The bracket supports and provides cooling to the transducer. Special care was taken when mounting the pressure transducer lines to avoid any hydrostatic pressure difference. To achieve this the elevation of the two pressure lines with respect to the bottom plate was maintained at equal levels.

The schematic of a variable reluctance pressure transducer is presented in Figure 6.10. A variable reluctance pressure transducer consists in an inductive half-bridge which consists of a pressure sensing diaphragm and two coils. The coils are wired in series and are mounted so their axes are normal to the plane of the diaphragm. Clamped tightly between the coil housings, the diaphragm is free to move in response to a differential pressure. The coils are supplied with an AC excitation, typically 5 Vrms at 3 to 5 KHz. The coils are matched so that their impedances are approximately equal. When a differential pressure is applied to the sensor, the diaphragm deflects away from one coil and towards the opposite. The diaphragm material is magnetically permeable, and its presence closer to one coil increases the magnetic flux density around the coil. The stronger magnetic field of the coil, in turn, causes its inductance to increase, which increases the impedance of one coil. At the same time, the opposite coil decreases its impedance. The change in coil impedances brings the half-bridge out of balance, and a small AC signal appears on the signal line.

The change in coil impedance is directly proportional to the position of the diaphragm, so the amplitude of the signal is directly proportional to the applied pressure. The phase of the signal with respect to the excitation is determined by the direction of movement of the

diaphragm. The output of a variable reluctance circuit at its full-scale pressure is 20 mV/V or more, which is significantly high.

These pressure transducers have the ability to measure very low pressures accurately. They also have a high frequency response and rugged durability since they have no linkages or other connections to the sensing element. They can be built in a welded version where the chambers are mounted together by welding. In this design they can withstand very high line pressures of up to 3200psig (220bars), and since the temperature sensitive electronics are separate from the sensing device, they can operate at cryogenic temperatures. For the above-mentioned reasons, a variable reluctance pressure transducer model DP10 was selected. The construction of the DP10 is compatible with the vacuum chamber requirements since it exposes only metal surfaces to the surrounding, exhibiting very low out-gassing.

The DP10 pressure transducer comes with a signal-conditioning unit (CD15), which consists of a carrier demodulator. The unit provides a 5kHz excitation signal to the transducer, allowing zero balancing and span adjustments using ten-turn dials. The unit also processes the transducer output, providing a -/+10V dc output for full scale.

The pressure transducer provides a linear output voltage signal with the pressure input. A preliminary calibration was done using liquid nitrogen. A special set-up for the calibration was designed to allow pressure measurement on the order of Pascals.

The calibration set-up scheme is presented in the Figure 6.11. The pressure transducer is placed inside the vacuum chamber and connected to the cold end of the second stage of the cryostat using a copper bracket (Figure 6.12), which supports it and allows cooling of the DP cell. The transducer is mounted to the bracket using four bolts, and a graphite foil

is placed between the mating surfaces of the bracket and transducer to decrease the contact thermal resistance. The pressure lines are passed through a feedthrough, which allows the lines to come out from the vacuum chamber and then connect to the calibration set-up. The calibration set-up consists of two parallel lines, connecting the positive side of the pressure transducer to a manometer and the negative side to the atmosphere. A set of nine valves is used to control the vacuuming, charging and operation of the calibration set-up (Figure 6.13). The valves V1 and V7 are used to isolate the system from the charging and vacuuming lines. The valves V3 and V9 are connected between the positive and negative pressure lines to allow equilibration of the pressure levels between them. Valves V2 and V5 are connected along the negative line and V4 and V6 on the positive line, which allows the pressure transducer to be isolated from the manometer in different stages of the vacuuming and charging process. An absolute pressure transducer is used to monitor the pressure on the charging line and inside the calibration system.

The manometer is installed on the positive line. One end is connected through the positive pressure line to the pressure transducer, while the other end is connected to a cross connection (Figure 6.11). In this cross connection three lines are brought together: the line exiting from the pressure transducer, the negative line, and a gas nitrogen (GN2) purging line. Through the purging line a very small outgoing nitrogen flow is provided to ensure that no air gets into the system. The valve V8 controls the GN2 purge flow, which is released to the atmosphere. This cross connection allows an equilibration of the pressure at the exit of the manometer and the negative pressure line.

The system is cleaned a few times by vacuuming and purging it with GN2. To vacuum the system the valves V2, V4, and V7 are closed, with the remaining valves left open. Then V1 is closed and V7 is opened to charge and purge with GN2. This operation is repeated at least three times. After cleaning, the system is charged and the valves V5 and V6 are closed to isolate the pressure transducer from the rest of the system. The vacuum chamber is evacuated and the transducer is cooled down to 73K such that at 1atm (15 psi) the nitrogen inside the pressure transducer chambers is in liquid state.

A small, outgoing GN2 flow is established in the part of the system open to atmosphere. Alcohol is poured inside the manometer, which closes the communication of the positive and negative lines in that region so that they communicate only through the valve V3 at this point.

When the pressure transducer temperature reaches steady state at 73K, which ensures liquid nitrogen inside the pressure transducer, the valves V2, V4, V5 and V6 are opened. At this point the manometer level is zero and the pressure between the positive and negative sides are equal since V3 and V9 are open. When V3 and V9 are closed, one side of the pressure transducer is connected to the atmosphere and the other to the positive end of the manometer. By closing and opening V7 the positive side pressure is increased, and by opening V3 it is decreased, allowing DP variation. The pressure measurements are made by recording the height difference between the liquid levels inside the manometer. For the liquid nitrogen calibration tests the liquid used inside the manometer was alcohol. The manometer tube orientation was vertical.

The results of three sets of calibration tests are presented in Figure 6.14. The first set of results was obtained using GN2 at room temperature and atmospheric pressure; the

second set of tests used liquid nitrogen (LN2) at atmospheric pressure at 75K, and for the last set the temperature was set to 68K. The least square fit line for the data has the equation DP = 85.861×V - 2.7882, and the R^2 = 0.9981 where DP represents the differential pressure applied to the transducer, V represents the transducer voltage output, and R^2 the explained variance. The standard deviation and the maximum deviation for each test are presented in Table 6.2. The GN2 tests present a maximum deviation of about 16Pa, which represents about 2% of the full range. The liquid nitrogen tests have a slightly increased maximum deviation of 36 Pa for the 75K tests and 23 Pa for the 68K tests, which represents 4.1% FS and 2.7%FS.

Table 6.2 Results for the liquid nitrogen calibration tests

Test	Standard Deviation	Max Deviation
GN2 (Run 1)	4.88	15.93
GN2 (Run 2)	3.77	14.56
GN2 (Run 3)	4.34	14.86
LN2 T=75K (Run 1)	5.16	23.24
LN2 T=75K (Run 2)	6.66	23.24
LN2 T=75K (Run 3)	11.15	36.62
LN2 T=68K (Run 1)	7.59	23.39
LN2 T=68K (Run 2)	5.54	22.02
LN2 T=68K (Run 3)	11.15	18.00

The values for each set of tests were close and the results show that cryogenic operating conditions do not affect the pressure transducer operation. Also, the least square fit line is very close to the pressure conversion line provided by the manufacturer, which is given by DP = 86×V. These considerations allow us to conclude that the pressure transducer calibration can be performed in room temperature conditions and used in the cryogenic conditions.

The error analysis shows that the error in reading the height difference is the main source of error for the calibration. The uncertainty of about +/-1 mm in the height difference readings translates to a pressure uncertainty reading of about 15.6 Pa.

A low range calibration of the transducer was performed using the same set-up. A series of improvements with respect to the previous calibration were applied to allow much lower resolutions. For this calibration, the manometer liquid used was n-heptane, which has one of the lowest densities among the atmospheric liquids (687kg/m^3), about 15% lower than the alcohol. Another improvement, which allowed more accurate measurement of manometer pressure difference, was using an inclined tube manometer. The inclination angle was one degree with respect to the horizontal plane. Since as proved before the fluid present in the transducer does not affect its performance, the fluid inside the transducer was atmospheric air. The calibration range in this case was 0-1Pa. Figure 6.15 presents the calibration data collected from more than three runs. The calibration curve used shown in the figure is DP = 86V, which is the curve provided by the manufacturer. For this curve the explained variance was about 90% and the maximum deviation was 0.15Pa. These experiments show that the pressure transducer has a pressure reading uncertainty lower than +/- 0.15Pa.

6.3.3.2 Temperature Measurement

Four silicone diodes (cryosensor) and two RTDs were used to measure the temperature of the loop. Four more silicone diodes controlled and monitored the cryocooler operation. The silicone diodes were acquired from Lakeshore, Inc. (DT471-SD-10L). One of the silicone diodes was acquired calibrated, and an uncertainty of about 0.5K is estimated. The silicone diodes were mounted at different locations along the loop. The hot side heat exchanger temperature was measured by three silicon diodes mounted at the inlet and

outlet and on the hot side heat exchanger. Two cryosensors (Lakeshore Cernox RTD) were installed at the inlet and outlet of the cold side heat exchanger. The reservoir temperature was monitored using a silicone diode attached on the topside of the reservoir. The silicone diodes' installation procedure had to be followed very carefully to obtain good temperature measurements. First, the surface was carefully cleaned using acetone and alcohol. Then, a small layer of varnish from Lakeshore Inc. was deposited on the measurement location. The varnish was covered with a very fine paper to insulate the silicone diode from the copper's conductive surface. Then the silicone diode was attached using some pressure. The silicone diode connections were made using very small gauge manganine wire, which has a relatively good electrical conductivity but a low thermal conductivity. These connecting wires were very carefully heat sunk to the copper pipe using varnish (Figure 6.16). This installation procedure ensures minimal heat leaks from the surrounding to the diodes through the connecting wires, and thus provides accurate measurements of the local temperature. The mounting was left to dry out for about 6-8 hours after which the varnish became solid and filled all the gaps between the silicone diode sensing surface and between the wires and the base surface.

One silicone diode was installed on the second stage of the cryostat, and three more were attached to the bracket. Table 6.3 summarizes the locations of the temperature sensors used in the cryogenic experiments.

Table 6.3: Locations of the temperature sensors

Part	Location
SD1	BRACKET CONTROL
SD2	BRACKET INTERLOCK
SD3	TWO PHASE RESERVOIR
SD4	HOT SIDE OUT
SD5	SECOND STAGE
SD6	HOT SIDE IN
SD7	BRACKET MONITOR
SD8	HOT SIDE

CX9 (SD9)	COLD SIDE IN
CX10 (SD10)	COLD SIDE OUT

6.3.3.3 Heaters

Heaters were used to maintain and control the temperature of different parts of the system. They were mounted on the reservoir, the hot side heat exchanger, and cryocooler interface. The heaters mounted on the reservoir and cryocooler interface were used to control their temperature. A small thermofoil resistive heater (0.5" by 0.5") with a maximum heat output of 5 Watts was attached to the hot-side of the heat exchange surface. The heaters' locations are summarized in Table 6.4.

Table 6.4: Locations of the heaters

Mounted on	Location	Characteristics
Hot side	Vertical long sides	Two connected in parallel, total resistance 48.1 ohms
Reservoir	Around middle	Resistance 54 ohms

6.3.3.4 Current Measurement

The current flowing through the EHD pump has values in the order of nA to mA. Therefore, careful planning and much thought had to be given to the instrumentation and measurement criteria to assure accurate measurements of the current. In the present set-up the final choice was narrowed down to measurement of the current across a resistance of 120MΩ installed in series in the high voltage circuit before the pump (Figure 6.17). A multimeter with very high input impedance was used to measure the voltage drop across the resistance. In parallel with the voltmeter (V), to protect it against current spikes during eventual sparking, a neon bulb (NB) was mounted.

6.3.4 Data Processing

The output of all of the instrumentation was connected to a data acquisition system (DAS) using Labview software, which displayed and stored the test information as it was

obtained. The same program was used to control all the heater circuits. The DAS acquired the readings from the temperature sensors, pressure transducer and high voltage power supply at time intervals of about 75sec.

6.4 TESTING PROCEDURE

The liquid nitrogen tests were conducted in the vacuum chamber facility at the NASA Goddard Space Flight Thermal Laboratory.

The complete testing procedure included several steps:

- loop cleaning
- pressure and electrical testing outside the chamber
- loop mounting inside the chamber
- pressure and electrical testing inside the chamber
- charging
- cooling down and obtaining a stable fully flooded system
- EHD pump testing.

The testing procedure had to implement a set of strict and specific cleaning requirements because the system was to be placed inside the vacuum chamber. A set of tests had to be performed when the loop was outside the chamber to ensure the electrical connections' integrity and to pressure proof the system. Once these tests were successfully passed, the loop was mounted inside the chamber. Installing the loop inside the chamber consisted of making and testing the electrical connections for the instruments and high voltage circuit and connecting the cooper interface to the cryocooler bracket. As the loop was installed inside the chamber the high voltage electrical connections were checked again, and another pressure test was performed. Finally the shroud top cover was mounted and the

chamber was closed. The vacuum pumping procedure was started, after which the system was cooled down to liquid nitrogen temperatures. The system temperature and pressure was controlled such that a steady state fully flooded loop was obtained. At this point, the EHD pumping tests were performed.

6.4.1 Loop Cleaning

The necessity for a clean system required the use of materials with very low out-gassing rates and the cleaning of the exterior surfaces from greases, oxidation and other contaminants. The presence of these substances inside the chamber would be harmful to the vacuum system because they could clog the vacuum pumps. Metals and Teflon present low out-gassing rates, which make them some of the best candidates for use in the vacuum environments. Copper, steel and Teflon are the main materials used in the loop to ensure vacuum chamber compatibility.

Before each installation of the loop, the system chamber was cleaned inside using alcohol and acetone to eliminate all the above mentioned contaminants. After these cleaning procedures, gloves were used to manipulate the loop. Special attention was paid to the soldered electrical connections, which could introduce wax contaminants if not properly cleaned.

6.4.2 Pressure and Electrical Testing Outside the Chamber

A set of electrical and pressure tests were performed to check the quality of the high voltage electrical connections and the system sealing. First, the pump was detached from the loop, and the continuity of the electrical connections was established by measuring the resistance between the electrodes and the other end of the electrical connection. Next, a spark test was performed, in which high voltage was applied to the system to determine

the voltage at which the sparking occurred in air. The sparking voltage in air is in the order of 3kV/mm. Thus, the expected sparking voltage for the pump was about 6-7kV for the 2.5mm electrode gap. This test was very important, since although the electrical connection would look fine when their resistance is measured, problems such as current leaks due to improper insulation could arise when the high voltage is applied. These problems, if not detected early, would be more pronounced at cryogenic temperatures due to the thermal stresses, which may open or widen small cracks present in the insulation.

Following the electrical connections testing, the EHD pump was installed in the loop and the pressure tests were performed. The pressure testing consisted of a preliminary leak test using a helium leak detecting system. First, a relatively low vacuum was pulled on the system. Then a small source of helium was sprayed around the system joints to test their sealing. The vacuum pump continuously pumped out the loop so that in case of a leak the helium that penetrated inside the system would be signaled by the helium detector. This leak detection system is reliable at relatively low to moderate pressures. Once any leak problems were fixed the system underwent a high-pressure test. The loop was charged to about 340psi (about 24bar) and the absolute pressure evolution in time was monitored in most of the cases overnight to ensure that it held pressure.

6.4.3 Loop Mounting Inside the Chamber

The loop mounting inside the chamber consisted of placing the shroud on which the loop is mounted inside the chamber, making the electrical connections, and attaching the copper interface to the cryocooler head.

The bottom shroud wall and the lateral walls were mounted together and the system was placed inside the chamber. The shroud was connected to the cryocooler's first stage

interface with twelve bolts (Figure 6.6) to support the system. The electrical connectors were mounted together, bundled, passed through a hole provided in the shroud, and finally attached to the lateral external wall of the shroud using aluminum tape to heat sink them. The instrumentation was tested to ensure that the electrical connections were made correctly. Then the high voltage connection was made by putting together the respective connectors and insulating them with several layers of heat-shrinking tubing to ensure good insulation. Finally, the second stage interface was mounted to the cryocooler bracket by tightening in the four designated bolts.

6.4.4 Pressure and Electrical Testing Inside the Chamber and Charging

Inside the chamber the loop was tested again by performing a spark test and a pressure test to ensure the newly made connections were appropriate. First the spark test was performed. Next, a number of cleaning flush-charges using research-grade nitrogen gas were applied to the system to eliminate moisture and other gas contaminates present inside the loop. The loop was vacuumed first to a moderate vacuum level (10^{-4} torrs) and then charged to about 340 psi (24bars). When the pressure was stabilized the loop was discharged down to a pressure just above the atmospheric pressure such that no backflow would contaminate the loop, and then vacuum was pulled again on it. This procedure was repeated a few times. To finalize the pressure testing, the system was charged to 340psi and the pressure was monitored for several hours to ensure no leaks were present.

The final step in the loop cleaning was to pull a lower vacuum on the system for a long period. Using a turbo pump, the loop was maintained at an absolute pressure in the order of 10^{-5} torrs, usually overnight. Finally, the system was charged at room temperature with

research-grade liquid nitrogen up to approximately 340psi (24 bars), the pressure at which the charged gas mass corresponds to a liquid filled cold loop.

6.4.5 Cooling Down and Obtaining a Stable, Fully Flooded System

Once the loop testing and charging was finalized the cooling procedure was started. The shroud top lid was mounted and the shroud covered using MLI to minimize the radiation heat exchange between the shroud and the chamber walls. The external surface of the MLI was cleaned using alcohol and then a final inspection was made to ensure that all the system components were in order. Then the vacuum chamber closed.

The vacuum chamber was evacuated using a mechanical pump, which took the chamber pressure down to about 10^{-4}torrs. Then a cryopump was employed to decrease the chamber pressure down to 10^{-6}torrs. Once the chamber was brought to the operating conditions vacuum of about 10^{-5}-10^{-6} torrs, the cryocooler was started. In order to get liquid nitrogen the loop needs to be cooled down from the room temperature to about 77K. During cool down the loop temperature was monitored to ensure a cooling rate of up to 100K/hour. This rate ensures acceptable thermal stresses on the system.

Figure 6.18 presents the temperature and pressure evolution during a typical cooling down process. In the first part of the cooling process, the thermal resistances controlled the temperature variation in the system. The SD5 temperature dropped the quickest because it was installed on the second stage (Figure 6.6) of the cryocooler, which is the coolest point. The second stage cooled the loop through the bracket (see SD1 in Figure 6.6) and the cryocooler interface. The cold-side in and out temperatures (see SD9 and SD10) were the lowest temperatures around the loop, as expected. The difference between the hot side (SD4, SD6 and SD8) and the cold side (SD9 and SD10)

temperatures was due to the thermal resistance of the loop. There was a small difference between the cold line (on which the pump is mounted) and the hot side due to the additional thermal mass of the EHD pump. The reservoir temperature decreased slower than the loop temperature because it was cooled at a lower rate. The pressure showed a relatively small drop due to the gas contraction of the cooling. When the cold side (SD9 and SD10) reached a temperature of about 144K the condensation started in this region. The loop cooling temperature and pressure slopes became steeper. The bracket temperature flattened since the whole cooling power of the cryocooler was used to condense the nitrogen inside the loop. When the loop temperatures reached about 115 K they met, since the condensation took place around the entire loop and the pressure started to drop very fast. Soon, the loop was flooded with condensate and further condensation took place only in the line towards the reservoir and inside the reservoir. This is why the pressure slope decreased. The loop continued to cool down and the pressure continued to decrease, together with the temperature. The reservoir temperature and absolute pressure followed the saturation curve until the radiation losses of the loop equaled the total cooling power and the loop temperatures stabilized. But, the condensation inside the reservoir continued at a lower rate, making the reservoir temperature to continue to drop. Finally, the reservoir and the loop temperatures met and corresponded to the saturation temperature at the loop pressure. When this moment occurred the reservoir heater was started to maintain the reservoir at a higher temperature than the loop. And thus the pressure in the system was increased to the corresponding reservoir saturation pressure while the loop was at a lower temperature. This ensured that only subcooled liquid was present inside the loop since due to buoyancy forces all the

eventual bubbles were either liquefied or traveled towards the reservoir. This ensures that the loop was fully flooded.

6.4.6 EHD Pumping Tests

The main objective of the pumping experiments was to evaluate the generated pressure head and mass flow rate of liquid nitrogen inside the loop.

The testing procedure began when the loop temperatures were stable and a fully flooded system was obtained. The high voltage was applied using a 0-60kV Glassman power supply described in the previous chapter. The high voltage power supply was turned on, and a negative DC voltage was supplied to the emitter. The voltage was increased at a rate of approximately 2 kV/min, and the system was allowed to reach a steady current. In a typical experiment, when the voltage increased above 6 kV the pressure transducer reading showed fluid motion. At a high voltage of about 12 kV the pressure reading was about 0.65 Pa (see Figure 6.19). Pumping experiments were run for more than 24 hours and stable operation of the pump was observed.

6.5 SAMPLE LIQUID NITROGEN EHD PUMPING RESULTS

A typical pressure head, voltage, and current variation are presented in Figure 6.20. The applied voltage was 14kV. As seen in the figure, the current decreased very slowly from about 120nA to 2nA over several hours. This current behavior is due to the fact impurities have a contribution to the initial current but they get neutralized or deposited in time. The pressure head reached a steady value of about 0.74Pa, much faster than the current. The pressure head reading standard deviation was about 0.07Pa during the steady regime. A stable operation was observed for periods higher than 5 hours, as the figure shows.

The liquid nitrogen pumping results for a range of different voltages are presented in Figure 6.21 and Table 6.5. The voltage was varied from 12kV to 20kV. The pressure head varied between 0.6Pa to 1Pa. The pressure reading uncertainty had a maximum value of 0.13Pa for the maximum pressure level. The pressure head increased almost linearly with the voltage. In most of the experiments the current reached a stable value at around 2nA.

The recorded pressure heads are relatively low with respect to the room temperature EHD pumping results. Still due to the very small flow resistance of the loop, the mass flow rates for these low-pressure heads were sufficient to achieve the desired heat removal rate of about 1W at a temperature drop of up to 1K. A more detailed flow analysis of the liquid nitrogen loop pumping will be presented in Chapter 9.

Table 6.5 The voltage and pressure head results for the liquid nitrogen EHD pumping tests

Voltage [kV]	DP [Pa]	Uncertainty [Pa]
12	0.68	0.07
12	0.51	0.06
12	0.57	0.01
14	0.73	0.08
14	0.63	0.09
14	0.74	0.07
14	0.86	0.10
16	0.88	0.09
16	0.73	0.08
18	0.86	0.09
20	0.90	0.03
20	1.00	0.13

6.6 SUMMARY

The present chapter presented the EHD closed loop pumping of liquid nitrogen. I have designed and operated a complex set-up which allowed liquid nitrogen EHD pumping tests to be performed for the first time. The experimental design and instrumentation criteria, as well as testing procedures were described in detail. Realizing the cryogenic conditions and the extremely low flow rates in the current experiments, the experiments systematically established EHD pumping of liquid nitrogen in a closed loop. The pressure head results are relatively small but the corresponding mass flow rates are sufficient to achieve the specs for cooling of HTS systems in line with the objective of this research. The pressure head results are very small (less than 1%) in comparison to the static tests. These results are explained by the fact that in pure cryogenic liquids, and in particular in liquid nitrogen, the rates of fluid ionization are very low. This conclusion is also supported by the very low pumping currents, which are up to 1000 times lower than those obtained during EHD pumping of liquids at atmospheric temperatures. The significance of the present experimental research is the fact that non-mechanical (EHD) pumping of liquid nitrogen in a closed loop was demonstrated for the first time. The work represented a combination of clever EHD electrode design and experimental design of the system.

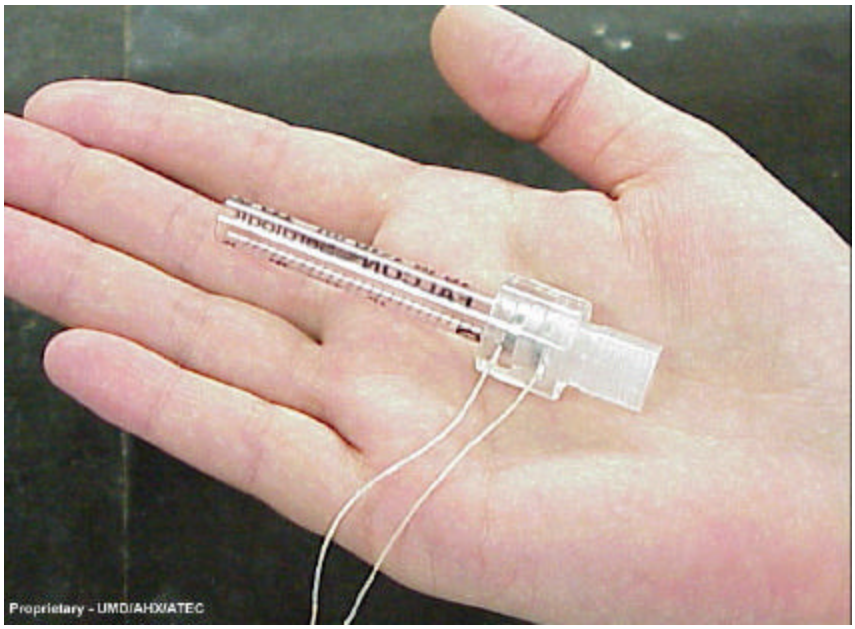

Figure 6.1 Test section used for the vertical EHD pumping tests

Figure 6.2 A photograph of a liquid nitrogen static pressure test. Arrow indicates liquid column height.

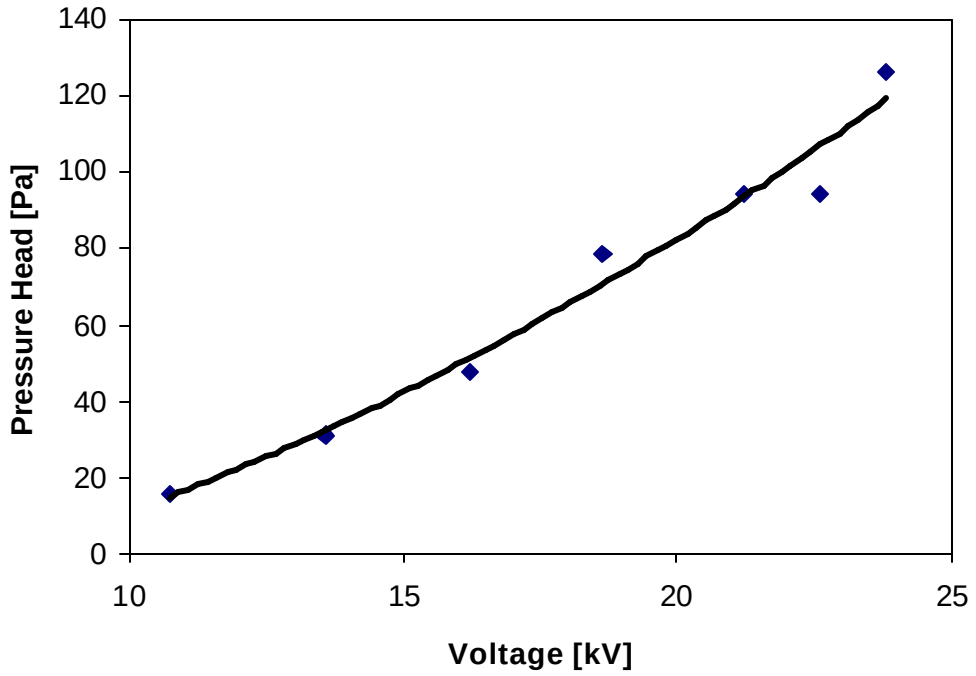

Figure 6.3 Pressure head versus applied voltage for LN2 Dewar tests

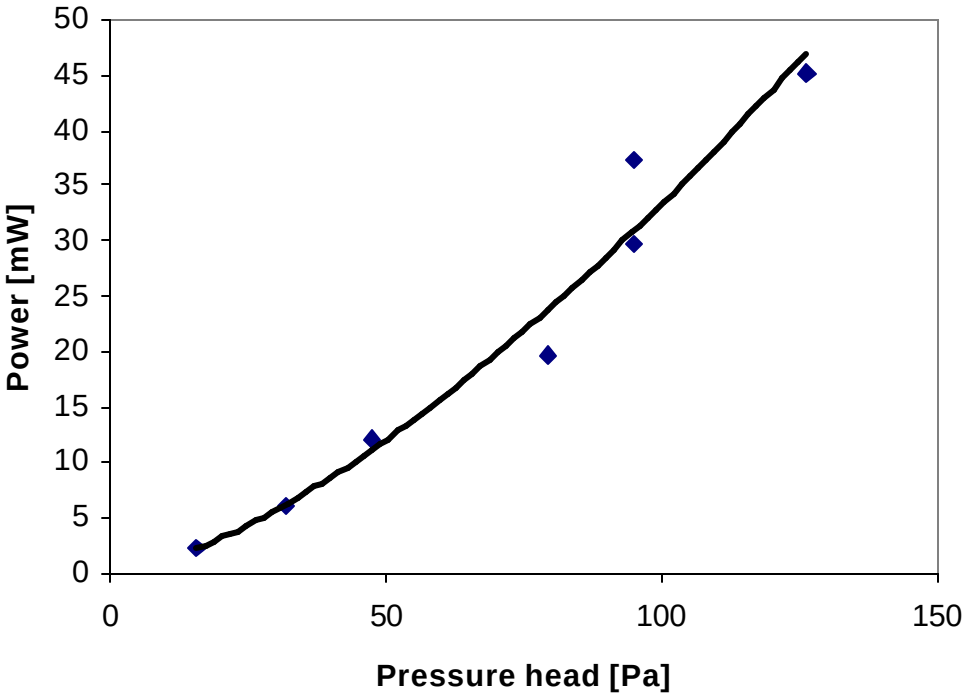

Figure 6.4 Power consumption versus pressure head for LN2 static pressure tests

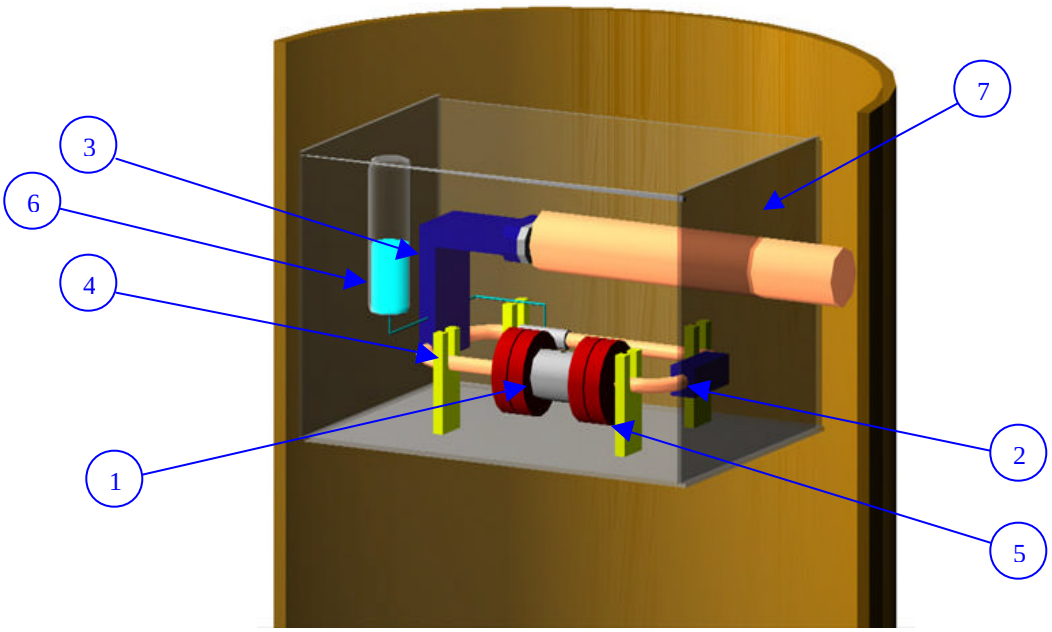

Figure 6.5 CAD drawing of the flow loop (1 - EHD pump, 2 – heater, 3 – cryocooler interface, 4 – 3/8 pipe loop, 5 – G10 supports, 6 – two-phase reservoir, 7 - shroud)

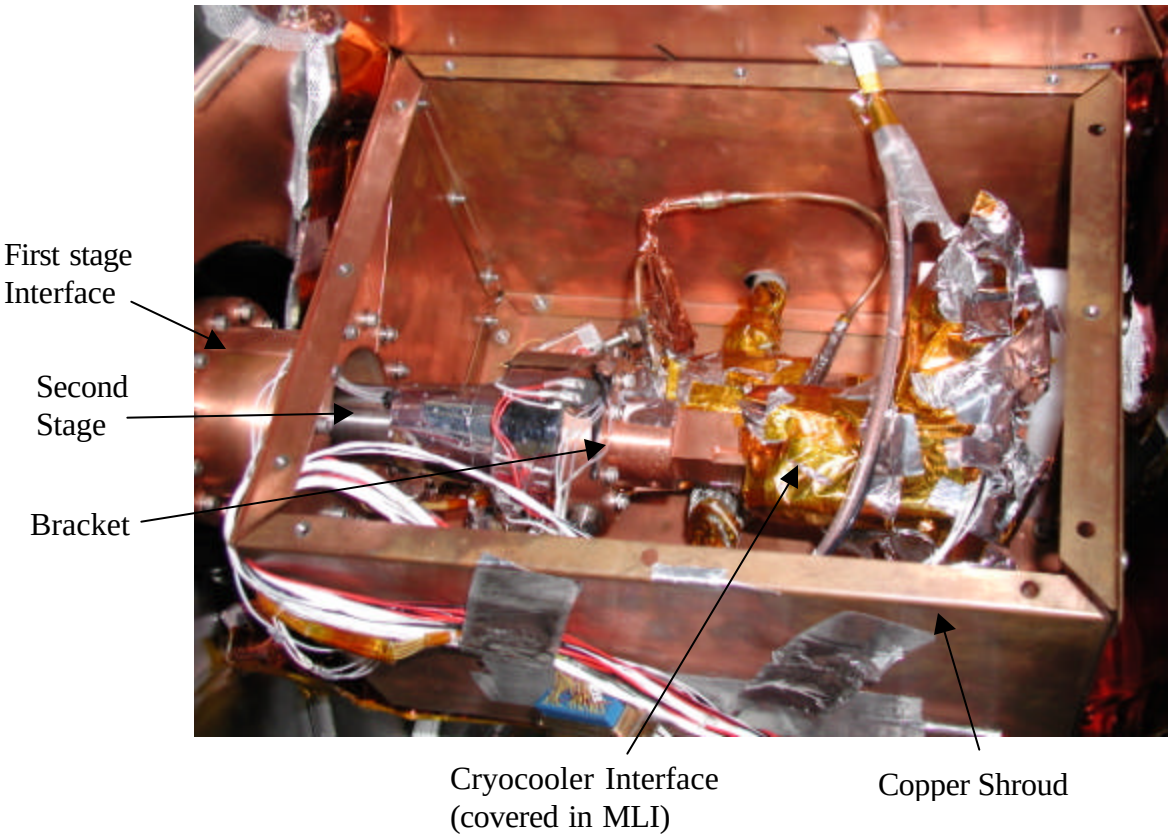

Figure 6.6 Picture of the cryogenic cooling loop

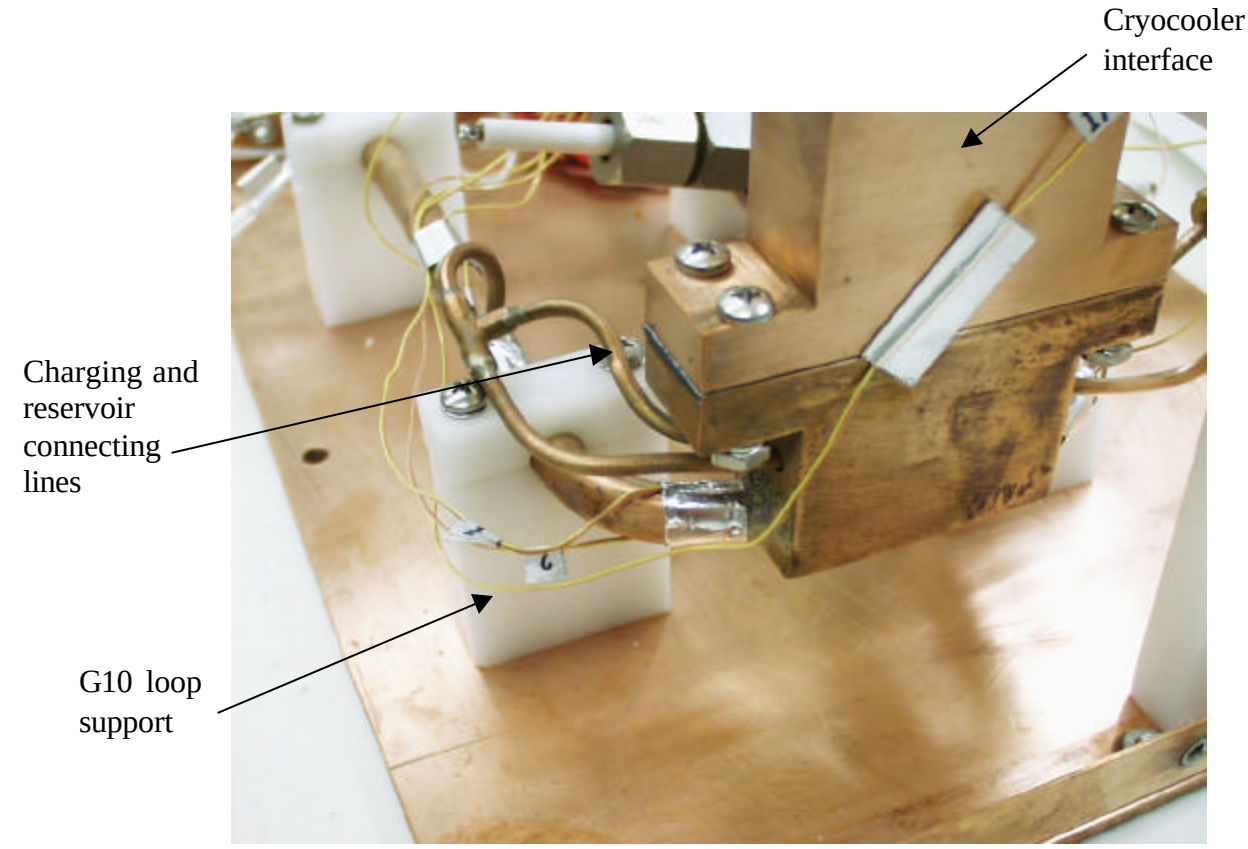

Figure 6.7 Cryogenic loop details

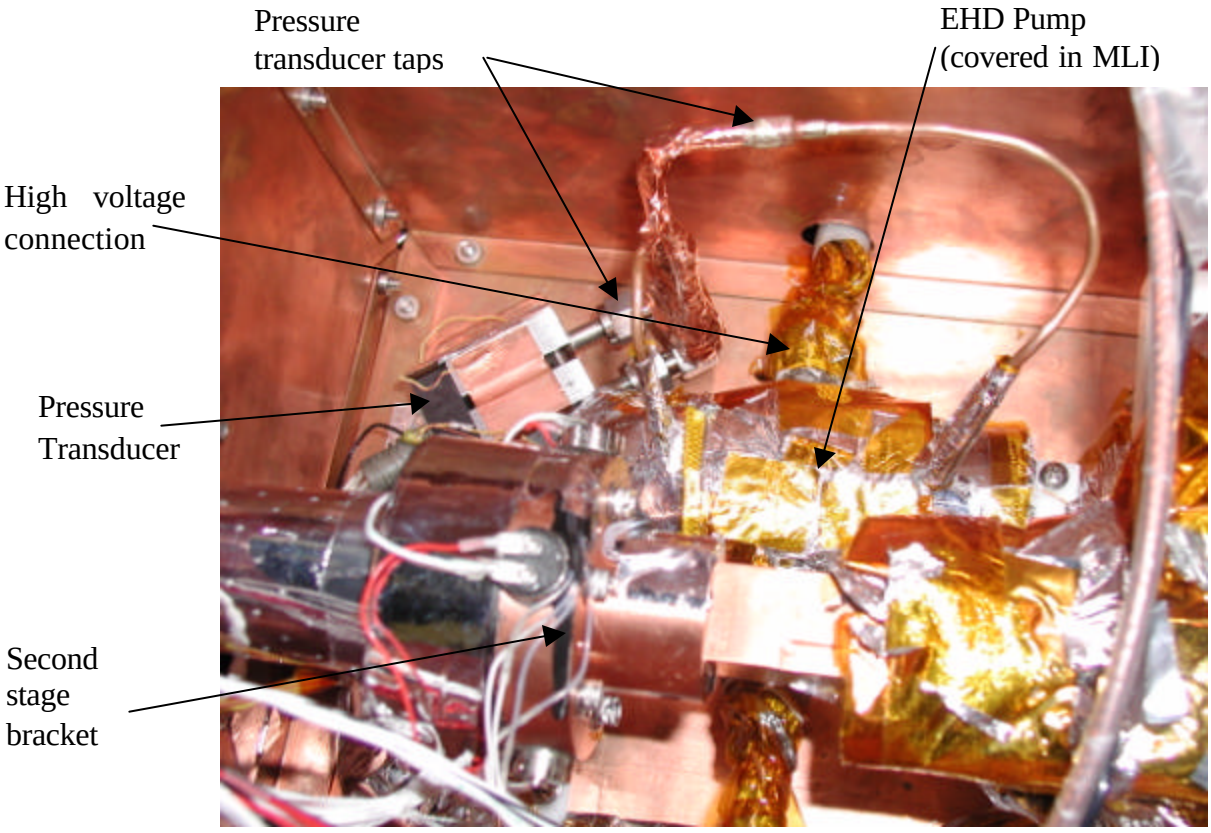

Figure 6.8 Picture of the cryogenic cooling loop

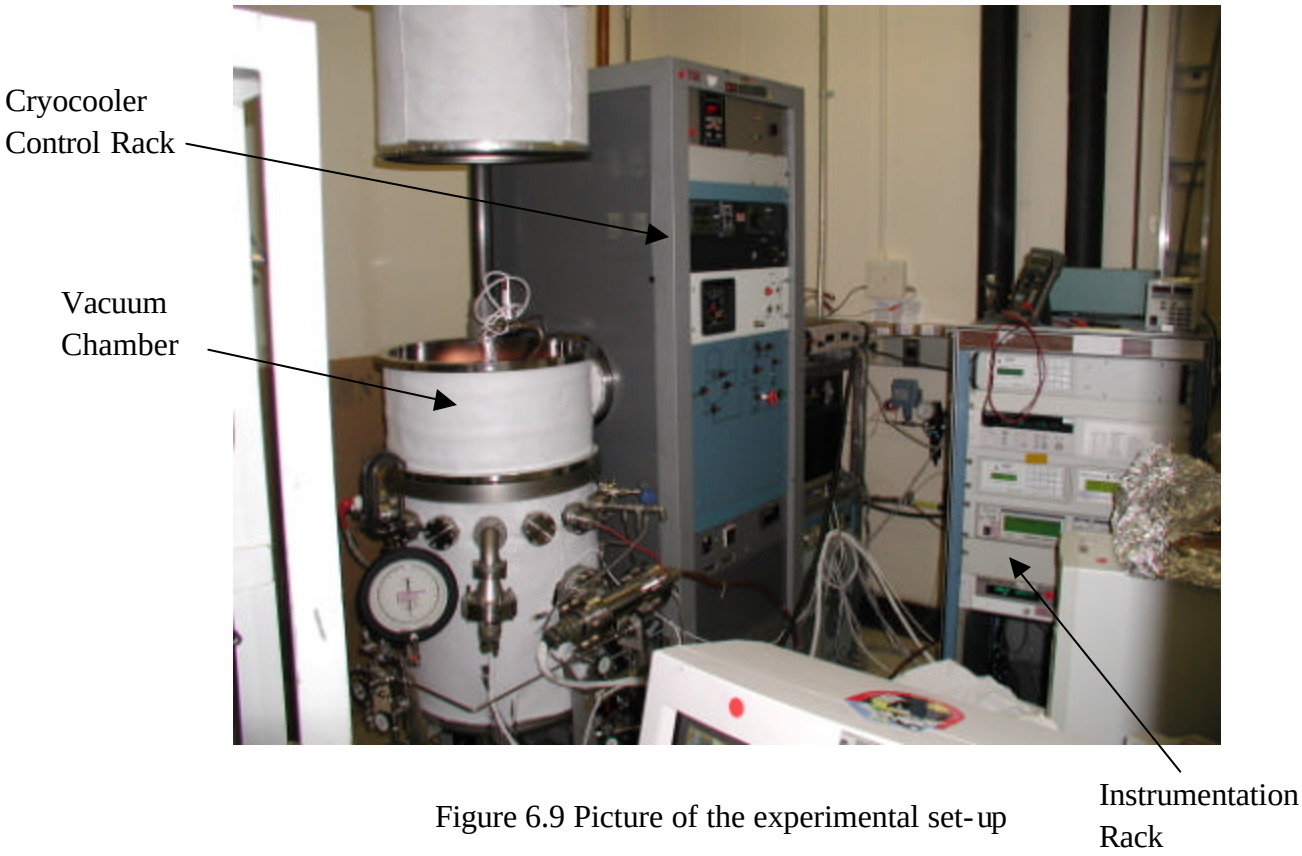

Figure 6.9 Picture of the experimental set-up

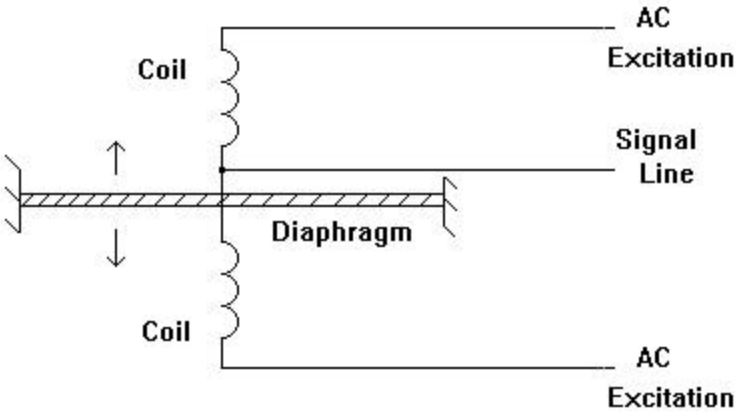

Figure 6.10 Variable reluctance pressure transducer schematic

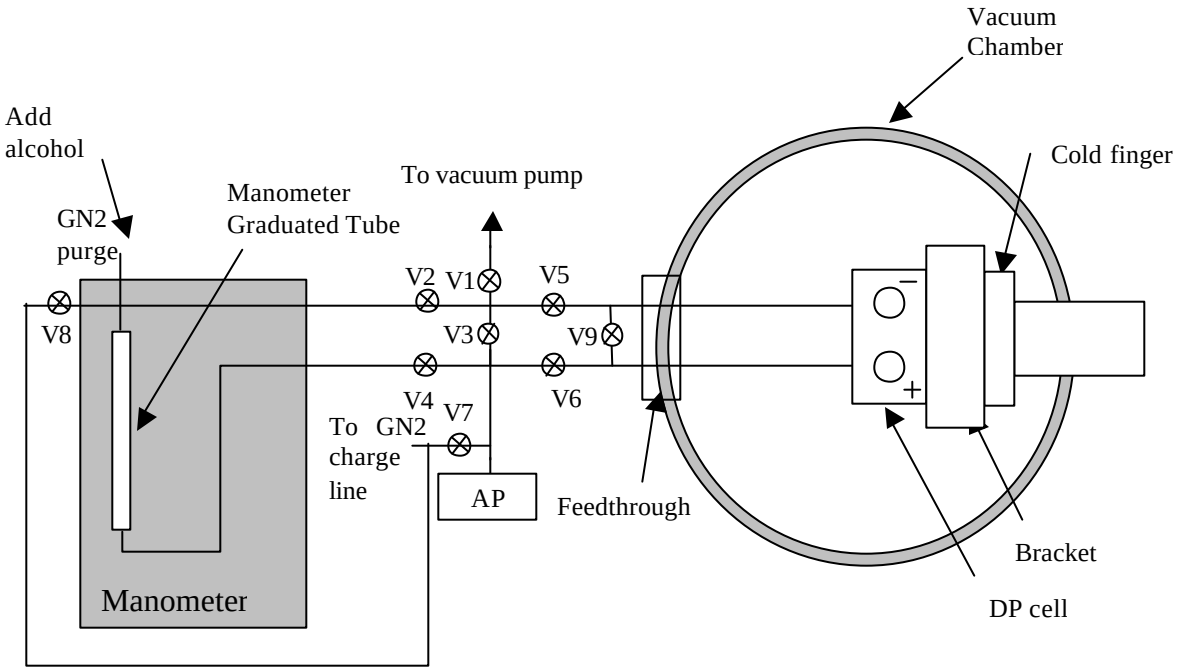

Figure 6.11 Schematic of the pressure transducer calibration set-up using liquid nitrogen

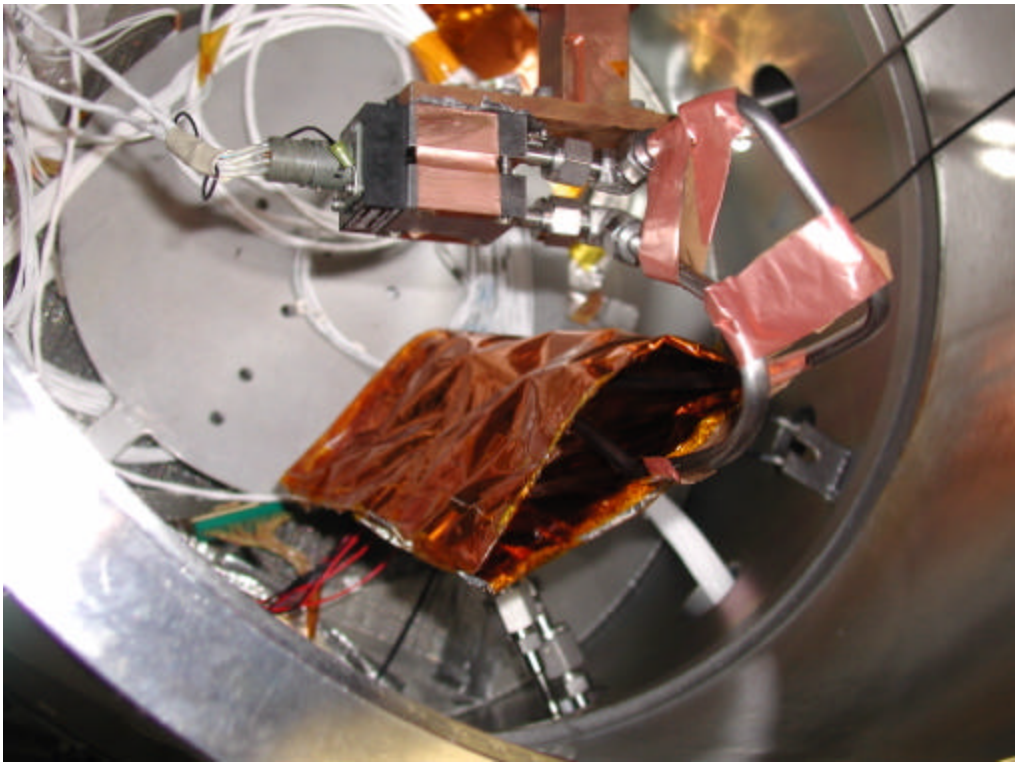

Figure 6.12 Picture of the pressure transducer mounting inside the cryogenic chamber during the calibration tests

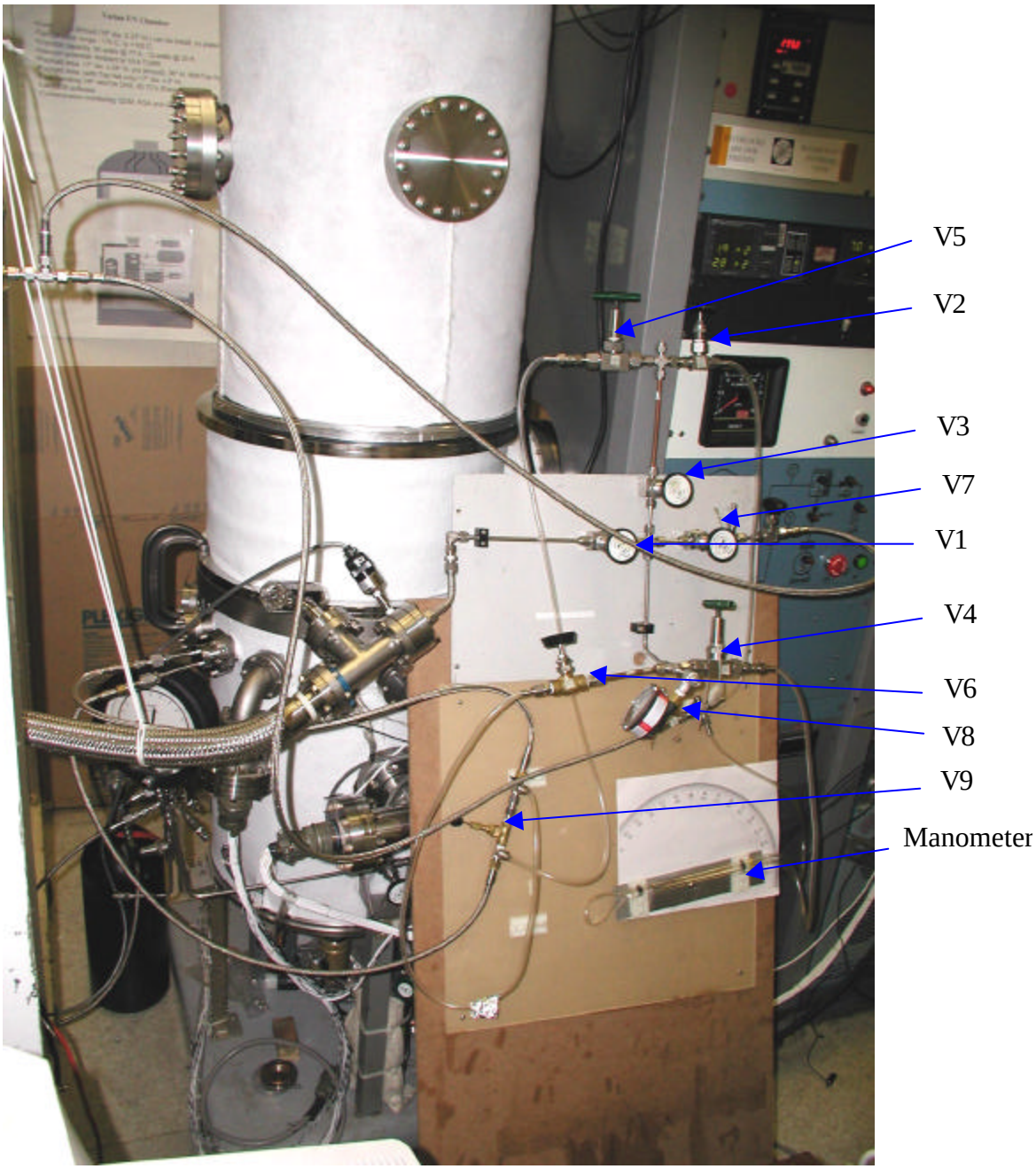

Figure 6.13 Picture of the pressure transducer calibration set-up using liquid nitrogen

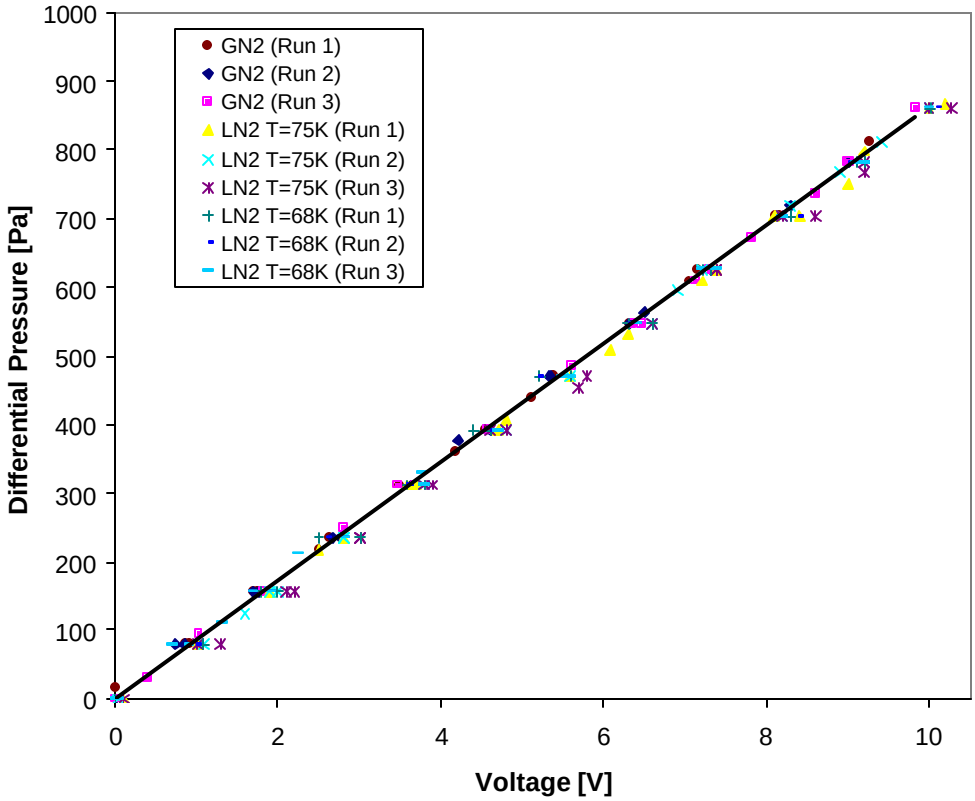

Figure 6.14 The calibration curve for the pressure transducer obtained during the liquid nitrogen tests

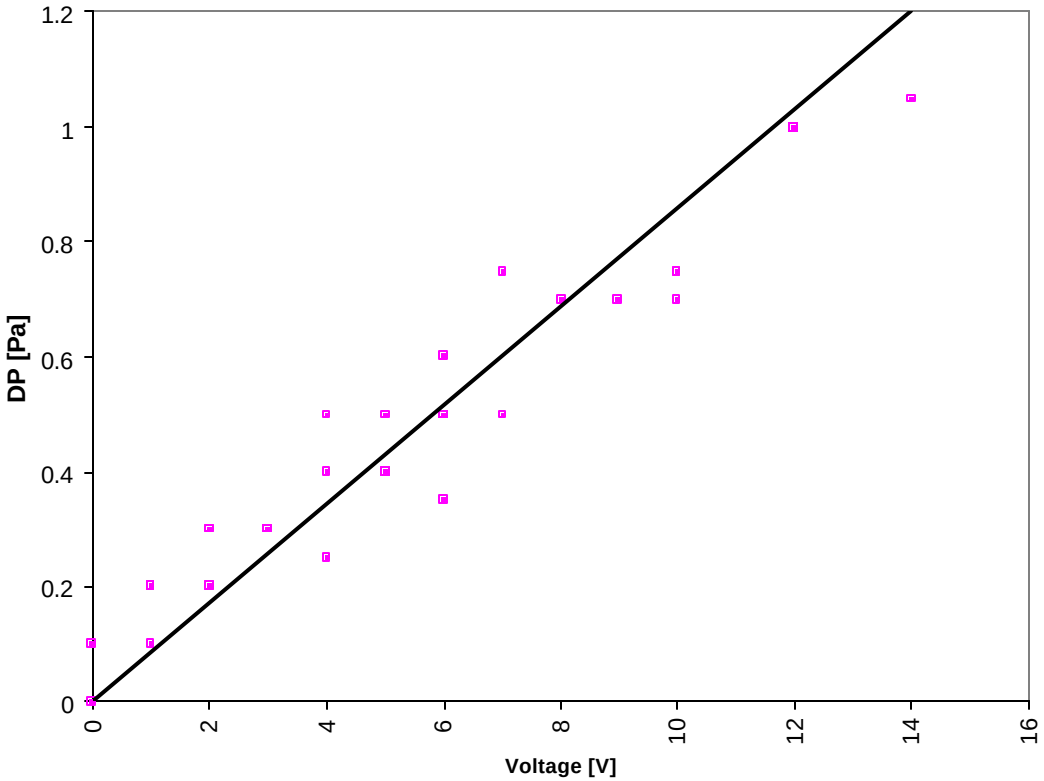

Figure 6.15 The low range calibration curve

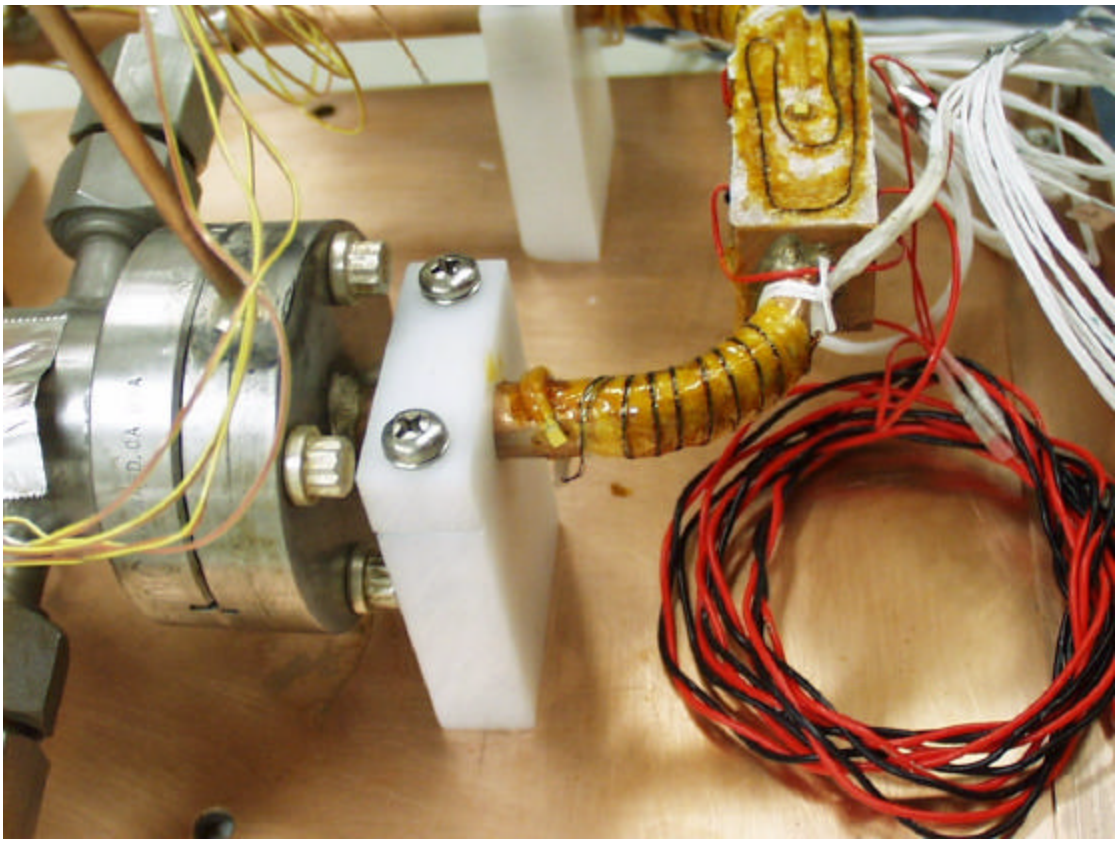

Figure 6.16 Picture illustrating the location and installation of two silicone diodes

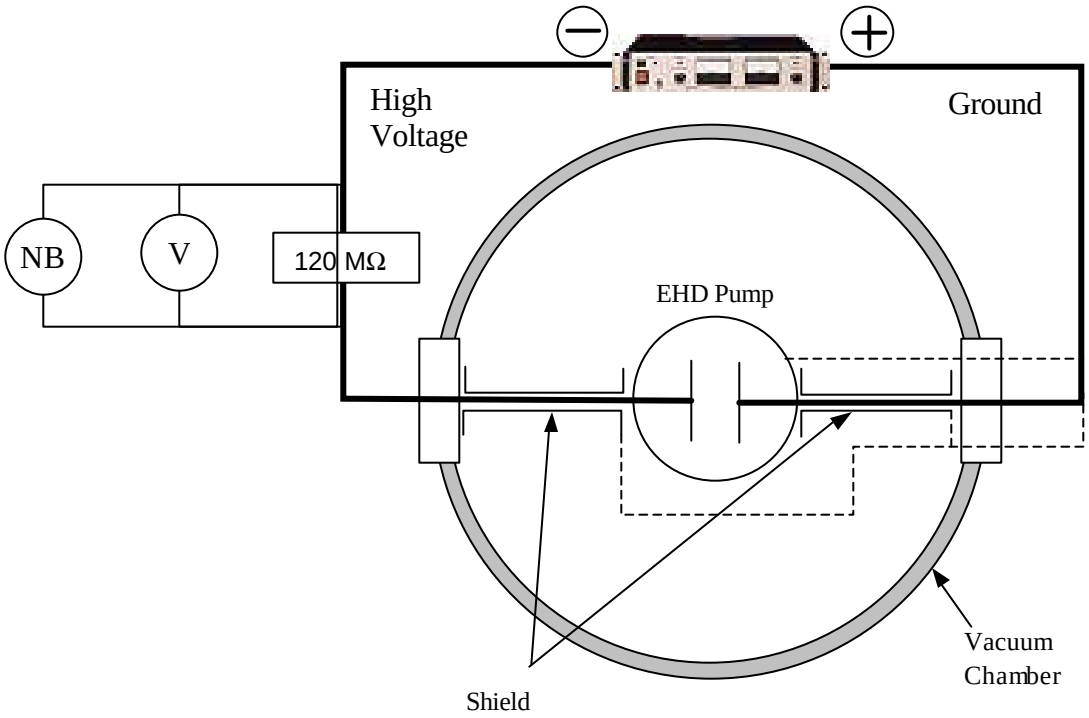

Figure 6.17 The electrical scheme of the set-up (V – voltmeter, NB – neon bulb)

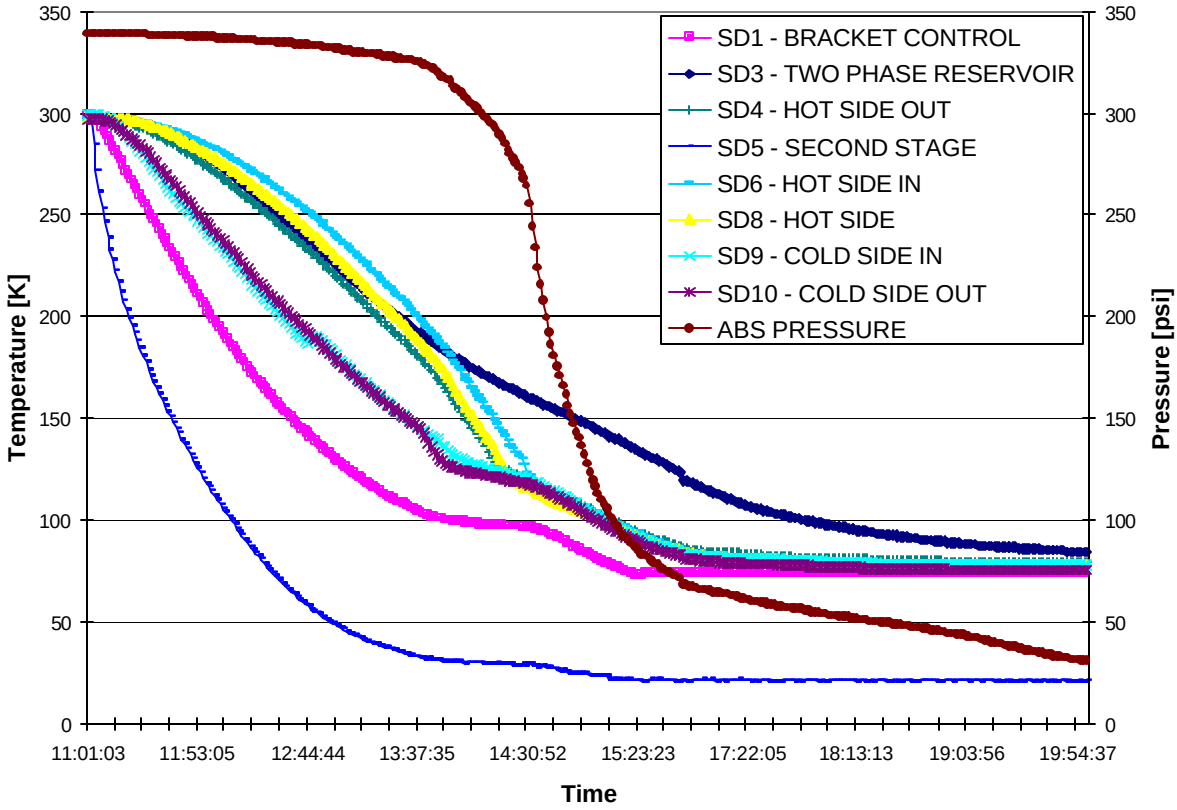

Figure 6.18 The temperature and pressure history during cooling

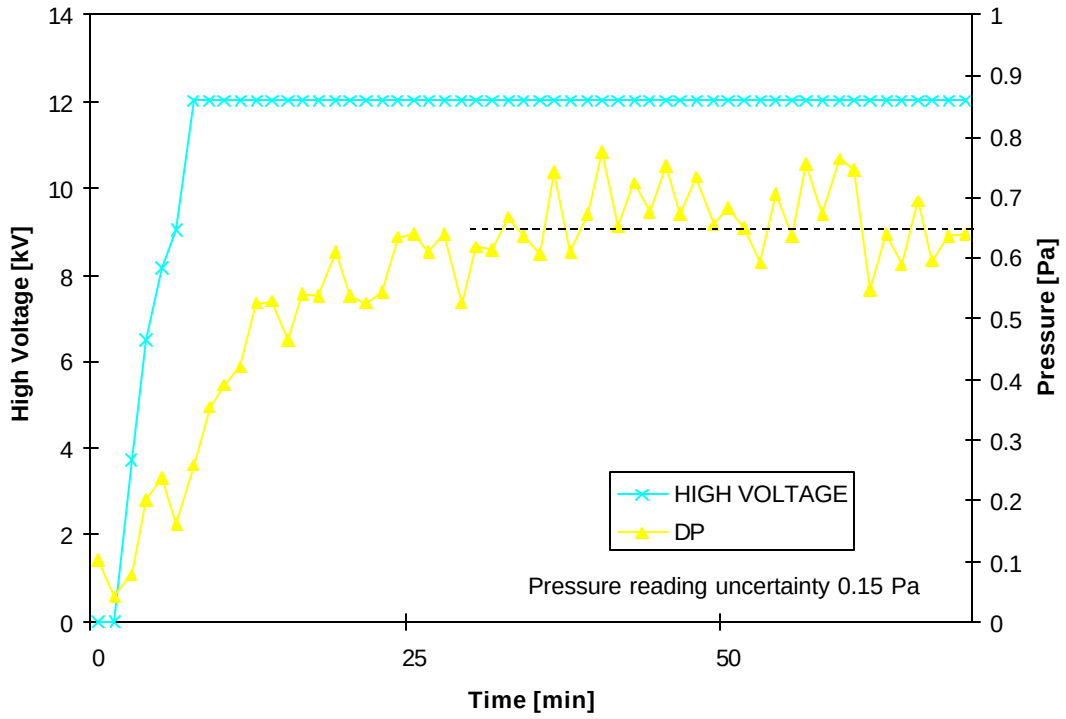

Figure 6.19 The differential pressure and voltage history during a typical EHD pumping test (Applied voltage: 12kV)

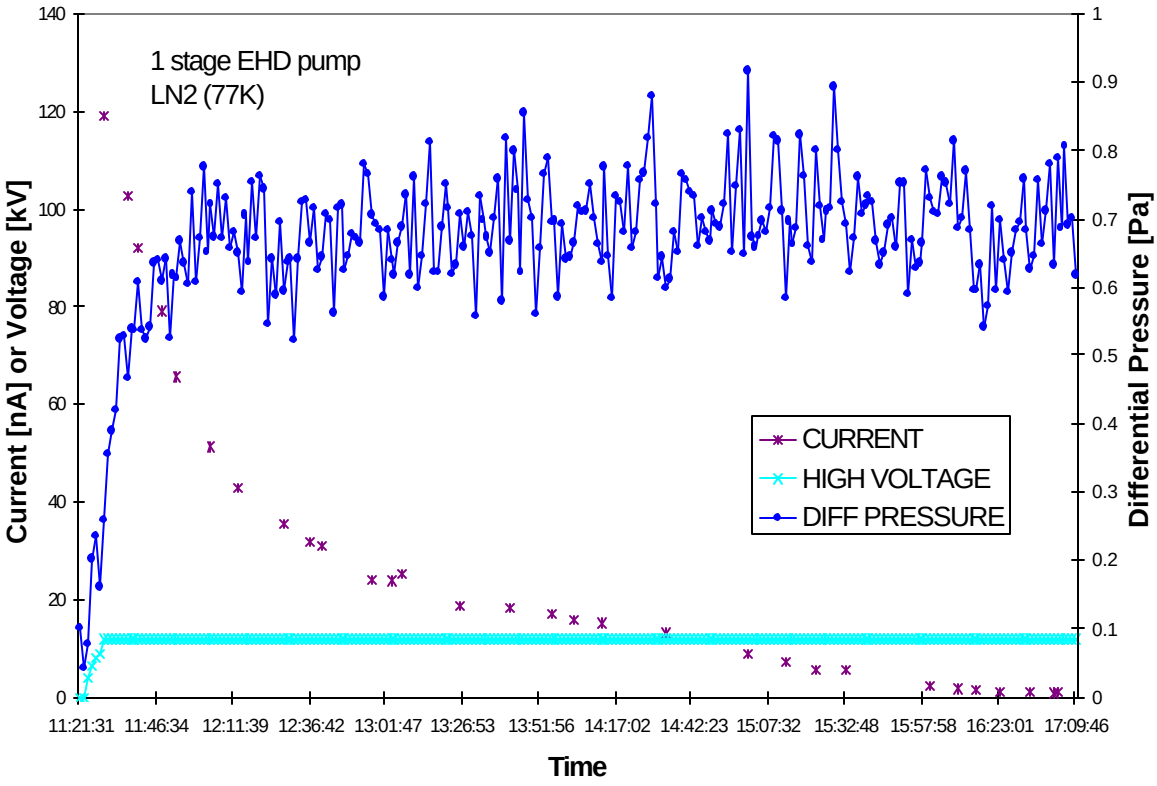

Figure 6.20 The high voltage, current and pressure evolution in time for liquid nitrogen EHD pumping test (applied voltage: 14kV)

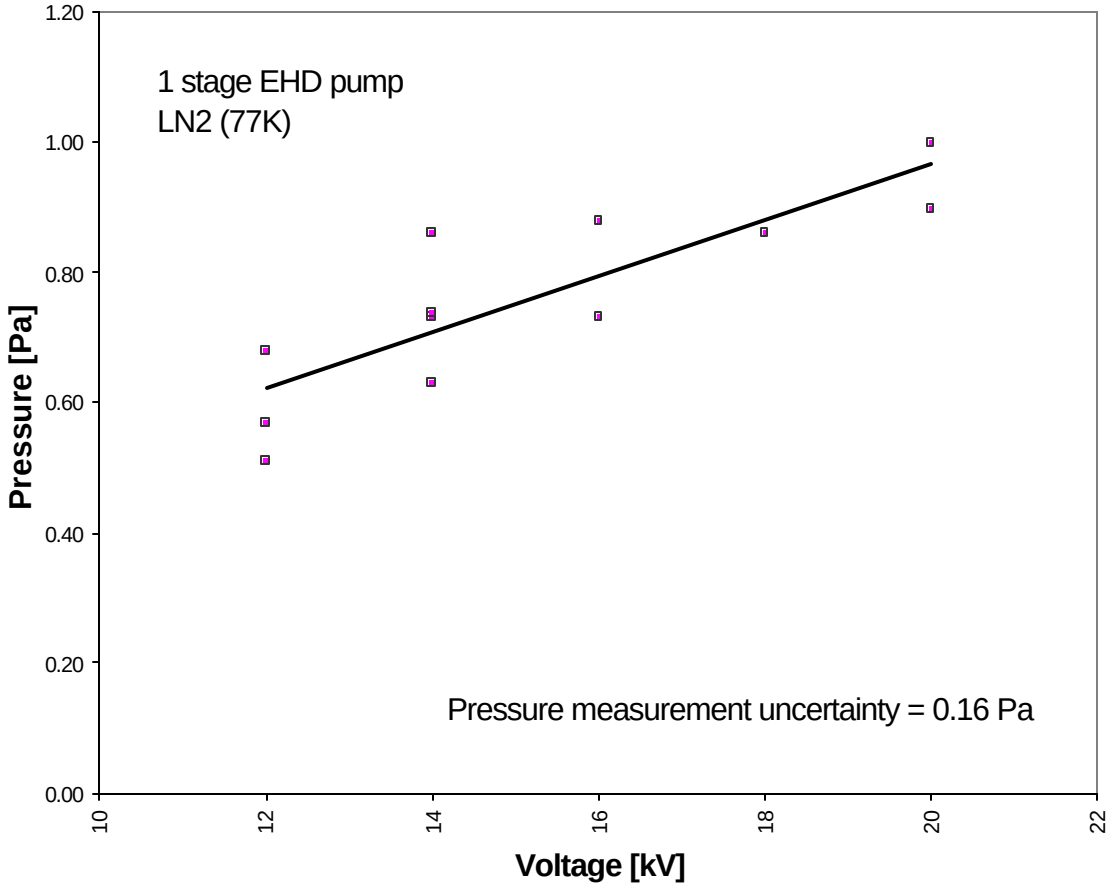

Figure 6.21 The pressure generation vs. applied voltage for the liquid nitrogen EHD pumping tests

CHAPTER 7 NUMERICAL SIMULATIONS OF LIQUID NITROGEN EHD PUMPING

7.1 INTRODUCTION

I have used the methodology for EHD pumping simulations developed by Amir Shooshtari in 2002 to determine the EHD pumping performance numerically. I have used the numerical modeling and simulation results to better understand the liquid nitrogen EHD pumping phenomenon and to improve the pumping performance. A complete analysis of the EHD pumping mechanism requires the solution of both the electric field and charge density distributions, given by a set of two coupled equations (Melcher, 1981):

$$\nabla^2\phi = -\frac{q}{\varepsilon} \tag{7.1}$$

$$\frac{\partial q}{\partial t} + \nabla[Kq\nabla\phi] = 0 \tag{7.2}$$

where ϕ denotes the applied field potential, q the charge density, ε the electrical permittivity of the medium, K the charge mobility and t the time. The first equation shows how the electric field is disturbed by the existence of charges inside the fluid, and the second represents the charge transport equation in electric field.

Besides its complexity, the solution to the system of equations is further complicated by the absence of an obvious boundary condition for the charge density. One common approach is to use the electric current obtained from the experimental *i-V* curve as the input for the charge density, but this still requires several assumptions regarding the ionization region at the emitter and the charge behavior inside the computational domain. The solution strategy employed in this modeling computes the charge distribution due to

the electric field's effect inside the computational domain assuming that there is no significant interaction between the flow field and the charge transport. This assumption proves reasonable for a space charge limited system. The first step in the computational solution is to compute the charge density distribution under the applied electric field. Then, a Navier-Stokes solver is used to solve the flow equations in which a source term, the EHD body force, is added. The code necessary to solve this problem was written as a User Defined Function in FLUENT^{TM}, which ensures both flexibility and computational power to solve complex, three-dimensional problems.

7.2 ONE STAGE PUMP SIMULATIONS

7.2.1 Problem Set-up

The EHD flow problem was solved for the EHD pump configuration (Figure 7.1) used in the experiments. In choosing the length of the computational domain, sufficient space was provided for the flow to develop, thus avoiding any entrance or exit effects that would affect the pumping region. The properties used in the numerical modeling are given in the Table 7.1.

Table 7.1: Thermophysical properties of the working fluid tested

Thermophysical Property	Liquid Nitrogen	Source
Boiling Point at 1 atm (K)	77	(Denat, 2002)
Liquid density (kg/m^3)	808.6	(Denat, 2002)
Dynamic viscosity (kg/m·s)	0.000169	(Denat, 2002)
Ion mobility (m^2/V·s)	2.5×10^{-5}	(Ramanan, 1987)
Dielectric constant	1.45	(Denat, 2002)
Dielectric strength (kV/mm)	>10	See Section 3.4.1

Due to difficulties in implementing an axi-symmetric solution, a three-dimensional problem set-up was used.

The computational domain consisted of a cylindrical channel inside which the emitter and collector were placed (Figure 7.1). The total length of the simulation domain was 36mm, and the pumping stage was placed in the middle. The emitter was 15 mm from the inlet and 2.5mm apart from the collector. The distance from the collector to the outlet was 13mm. A very important aspect of the electric field simulation was the tip radius. The emitter presents a series of very sharp regions, which, for the solution to converge, must have a finite dimension. Based on measurements done using an optical microscope, we could determine that the emitter tip radius of curvature was in the order of 10μm. To accommodate this fact, the geometry of the emitter tips for the 3D simulation set-up was modified to have a 10μm radius of curvature.

The grid generation was a real challenge since the aspect ratios involved in the problem are very large. Regions with a radius of curvature of 10 μm at the emitter tip and relatively narrow openings at the base of the emitter teeth had to be captured by the grid together with large openings represented by the flow channel of about 7mm. The grid was generated using a series of advanced features of Gambit. These functions allowed an outwardly increasing, radial mesh generation. Using these functions a fine enough mesh was generated around the emitter tips and the emitter teeth bases, and progressively larger elements were generated further from these points. In most of the cases meshes with more than 100,000 nodes were used, which rendered the computational efforts relatively important.

The boundary conditions for the electric field problem were:

- insulated walls for the inlet, outlet, and the channel walls ($\nabla\phi = 0$ at the wall);

- constant voltage for the emitter (ϕ = ct.). The emitter voltage was set to the respective voltage value and the collector to zero.
- The charge density boundary condition was set to zero gradient in the insulated regions and was set to a constant value for the emitter.

The charge density on the emitter was set according to the current experimental data. During the experiments current levels in the order of 2nA were obtained. An estimate of the charge density on the emitter based on the experimental data was obtained using the electrical current expression

$$I = \int_S qK\vec{E} \cdot \vec{n} dA = K \int_S q\vec{E} \cdot \vec{n} dA \tag{7.3}$$

where q is the charge density (C/m^3) going through the surface dA, I is the electrical current flowing between the emitter and collector, $\vec{E}$ the average electric field on the surface dA, K the ion-mobility, $\vec{n}$ the normal to the surface dA, and S the current flow area, which is taken as the mid-distance between the emitter and collector area.

Using a very rough estimation of the average for the electric field as voltage divided by the gap,

$$E = \frac{V_E - V_C}{d} \tag{7.4}$$

and with constant charge density we get:

$$I = KqEA_{cr} = KqA_{cr} \frac{V_E - V_C}{d} \tag{7.5}$$

where A_{cr} is the cross-sectional area, V_E and V_C the voltages at the emitter and collector, and d the gap.

Thus, a first estimate for the charge density at the emitter is given by:

$$q = \frac{Id}{KA_c(V_E - V_C)} \tag{7.6}$$

where A_c is taken as the collector surface area.

An iterative procedure was further used to determine the value of the charge density used in the numerical simulations. The first step was to use the above determined charge density value on the emitter and to calculate numerically the current corresponding to this charge density value. Then, using a trial and error procedure the charge density on the emitter was varied such that the numerically obtained current matched the experimental current.

Following this procedure a charge density value of 8×10^{-5} C was obtained for the emitter.

7.2.2 Solution Procedure

Using the problem set-up described above, the following computational procedure was employed to determine the charge density and electric field distribution as well as the flow parameters of velocity, pressure, and mass flow rate inside the EHD pump computational domain.

The solution procedure consisted of three computational steps:

1. charge density distribution solution
2. confined-channel flow
3. open-channel flow solution

The first step solves the electric field problem with charge injection from the emitter but no flow. The second step calculates the flow field inside the EHD pump using the forced EHD-coupled Navier-Stokes system equations when the channel is confined. The last step determines the flow solution using an open channel configuration. The main assumption in this simulation is that the electric field and flow problem can be decoupled

such that the electric problem is solved first and the flow solution is subsequently obtained.

7.2.2.1 The Charge Density Distribution Solution

The first step in the solution procedure was to obtain the charge distribution in the computational domain. The geometry and grid generation are presented in Section 7.2.1 (see Figure 7.1). The boundary conditions are given in Table 7.2.

Table 7.2 The charge density solution boundary conditions

Boundary	Charge density boundary condition	Voltage boundary condition
Inlet	No Flux	No Flux
Outlet	No Flux	No Flux
Wall	No Flux	No Flux
Emitter	0	Constant
Collector	0	No Flux

The solution was converged when the residuals dropped at least three orders of magnitude.

The solution for the case of an applied voltage of 16kV and no charge density on the emitter is presented in Figure 7.2. The electric field magnitude distribution in mid-plane between the emitter and collector is shown. The electric field value range was restricted to the one presented in the image for contrast purposes. The values are in V/m. The maximum electric field location was at the tip of the emitter and had a value of 320MV/m, while the minimum value was around 150V/m and was located around the channel axis region and in the region outside the pumping stage. The average electric field in the region between the emitter and collector was about 3.7MV/m.

The same case was considered again but with a charge density on the emitter. A comparison between the electric field values in the two cases is presented in Table 7.3.

The maximum value was located in both cases, as expected, at the tip of the emitter teeth, since this was the point with the highest curvature. As can be seen, the presence of the charge density on the emitter did not disturb the electric field distribution in a significant manner (less than 7%). This is explained by the relatively small value of the charge density on the emitter. Also, the average electric field value was minimally affected. The calculated electric field value (Eq. 6.3) is very much off. This is to be expected, since Eq. 6.3 is valid for uniform distributed voltage, while in our case important voltage gradients were present.

Table 7.3 The electric field values

Charge density on emitter [C]	Electric Field [MV/m]			
	Maximum	Minimum	Average	Calculated (Eq. 6.3)
0	320	0.00154	3.724	6400
8×10^{-5}	300	0.00002	3.720	-

The above considerations show that the presence of the changes on the emitter does not significantly change the electric field distribution between the emitter and collector.

The numerical solution for 16 kV and a charge density on the emitter of 80 μC is presented in Figure 7.3 and Figure 7.4. The voltage distribution inside the computational domain is presented in Figure 7.3. The voltage decreased from the value of the applied voltage on the emitter to zero on the grounded collector. The charge distribution solution is presented in Figure 7.4. The maximum charge density was found on the emitter, as expected, and the charge density decreased towards the collector. The charge filled the space between the emitter and collector almost uniformly, suggesting that the EHD body force acts on the volume occupied by the charges between the electrodes.

7.2.2.2 The Confined Channel Flow Solution

For the flow solution, the EHD body force was determined using the solution from the previous step. In this step only the flow solution with a body force was considered. The flow boundary conditions are presented in Table 7.4.

Table 7.4 The confined channel flow solution boundary conditions

Boundary	Boundary Condition
Inlet	Solid Wall
Outlet	Solid Wall
Wall	Solid Wall
Emitter	Solid Wall
Collector	Solid Wall

The confined channel solution allowed us to determine the maximum pressure generation of the EHD pump according to the numerical simulation.

The velocity and pressure solutions are shown in Figure 7.5 and Figure 7.6. The velocity vectors were directed from the tip of the emitter, where the field emission takes place, to the collector surface. The charges were accelerated towards the collector, where the maximum velocity was reached. A back flow along the channel axis was observed because the channel was confined. The pressure solution, as can be seen from Figure 7.6, increased along the channel from values close to zero at the emitter to about 1 Pa close to the exit section. The pressure generation of the pump was considered to be the difference between the average pressure on two cross-sections located 0.5mm from the inlet and outlet. Thus, in this case the maximum pressure generation obtained was 1.08Pa.

7.2.2.3 The Open Channel Flow Solution

In the second case a solution for the zero pressure drop across the computational length was considered to obtain the maximum mass flow rate of the EHD pump. The boundary conditions used are presented in Table 7.

Table 7. The open channel flow solution boundary conditions

Boundary	Boundary Condition
Inlet	Inlet pressure = 0
Outlet	Outlet pressure = 0
Wall	Solid Wall
Emitter	Solid Wall
Collector	Solid Wall

The solution for this case is presented in Figure 7.7 and Figure 7.8. The velocity vectors are shown in Figure 7.7. The velocity entered the pumping section with a laminar parabolic profile and was accelerated by the body force in the region between the emitter and collector. The maximum velocity was reached in the vicinity of the emitter tips and had a value of about 5cm/s. The pressure distribution is presented in Figure 7.8. The pressure variation was very small due to the imposed boundary condition. The maximum mass flow rate was determined to be 0.95 g/s, which represents a volumetric flow rate of about 70.65 ml/min.

7.2.3 Simulation Results

The single-stage EHD pump simulation was run for different applied voltages. The maximum, minimum and average electric fields are presented in Table 7.5 and Figure 7.9.

Table 7.5 The electric field results for the single-stage EHD pump

Voltage [kV]	Electric Field		
	Maximum [MV/m]	Minimum [V/m]	Average [MV/m]
12	224.54	1.45	2.83
14	262.16	0.74	3.31
16	299.89	0.87	3.78
18	337.45	2.46	4.25

As the voltage was increased from 12 to 18 kV, the maximum electric field, located at the tip of the emitter where the field emission occurred, increased from about 225MV/m to about 340MV/m. The average electric field was determined by taking the average of the electric field in a cross-section located at the middle between the emitter and collector. The minimum electric field occurred in the region outside the space between the electrodes.

The flow solution results for different voltages applied are presented in Table 7.6 and Figure 7.10.

Table 7.6 The maximum pressure head and mass flow rate for the single-stage EHD pump

Voltage [kV]	DP [Pa]	Mass Flow Rate [g/s]	Re
12	0.81	0.80	778
14	0.94	0.88	860
16	1.08	0.95	926
18	1.22	1.02	992

The flow numerical simulation allowed us to determine the pressure head and mass flow rate for the simulated configuration. The flow Reynolds number is calculated from the mass flow rate using:

$$\mathrm{Re} = \frac{4 \cdot \dot{m}}{\pi D \mu} = 972.53 \frac{s}{kg} \cdot \dot{m} \tag{7.7}$$

where the EHD pump geometry and liquid nitrogen properties were used.

A maximum pressure head of about 0.81 Pa was obtained at 12kV, while at 18kV the maximum pressure head reached 1.22Pa. The maximum mass flow rate increased from 0.8g/s to about 1.03g/s. The Reynolds numbers range between 780 to 1000 which correspond to a laminar flow regime.

7.3 THREE STAGE PUMP SIMULATIONS

The numerical simulation for a three-stage pump was considered to determine how multiple stages interact with each other and how electrical and flow parameter varies. The geometrical parameters and fluid properties were the same.

7.3.1 Problem Set-Up

The problem set-up and geometry are presented in Figure 7.11. The three stages were equally spaced at a distance about three times the electrode gap. The electrode gap of 2.5mm was the same as the single-stage simulations and the experimental tests. The inlet and outlet channel length was 15mm. The grid generation procedure was similar to the one used for the single-stage pump. The number of elements in this case was larger than 300,000. A voltage of 16kV and a charge density of 8×10^{-5} C were used on each emitter.

7.3.2 Simulation Results

The electric field problem solution is presented in Figure 7.12 and Figure 7.13. Figure 7.12 presents the electric field distribution. The results show relatively limited interaction between the stages. The maximum electric field gradient was located between the electrodes. The maximum electric field was 528MV/m, located at the tips of the emitters. The higher electric field with respect to the single-stage simulation is explained by the total current being three times larger and by the interaction between stages. The minimum electric field was 2.06 V/m and was located in the regions outside the region between the electrodes. The charge density distribution is presented in Figure 7.13. A relatively inefficient charge collection was evident, since the charge emitted by the first stage reached the second stage. The simulation showed a charge interaction between stages. The amount of charge present in the region between the electrodes increased upstream.

The flow solution is presented in Figure 7.14 to Figure 7.16. First, the confined channel pressure head distribution is shown in Figure 7.14. The maximum pressure head obtained by the three-stage EHD pump in this configuration was about 1.09Pa, which is similar to the single-stage pump. The pressure distribution for the open channel is presented in Figure 7.15. An additional pressure drop with respect to the single-stage pump, can be observed, which is due to the pressure drop imposed (filtering effect) by the multiple emitters as well as to the electrical interaction between the stages. This was illustrated by the higher static pressure after the first stage compared with the other pressures. Similarly, after the second stage the pressure was higher than the average pressure in the channel. This filtering effect is relatively significant since it represents up to 50% of the total pressure head generated by the multi-stage pump. The channel length caused another additional pressure drop since it was longer compared with the single-stage case. The velocity contours for the three-stage EHD pump simulation are presented in Figure 7.16. The maximum velocity about 3.6cm/s was reached in the regions of highest electric field located around the emitter tips. The fluid accelerated in those regions and then transferred its momentum to the surrounding molecules. The maximum mass flow rate was 0.68g/s, which is lower than the single stage case, although the current was higher. These results suggest that an optimization study is necessary to determine an optimum configuration for the multistage pump.

7.4 EHD PUMP OPTIMIZATION STUDY

Improving the charge collection and reducing stage interaction should improve pumping performance. To address these issues an optimization study was performed. The

optimization consisted of a parametric study on the effect of different design parameters on the pumping performance.

7.4.1 Parametric Study

A parametric study was undertaken to determine the main design changes that would improve the pumping performance. The parametric study consisted of simulating different design configurations and comparing the results. First, a series of simulations for a single-stage pump was considered. The following parameters were chosen:

- Distance between the electrodes – the electrode gap
- Collector length
- Collector geometry

The applied voltage was 16kV and the emitter charge density 8×10^{-5}C. The maximum pressure head and mass flow rate were determined using the procedure described in the previous section.

The base case parameters were the ones used in the experiments and single-stage simulations: collector length was 2mm, electrode gap 2.5mm, and a ring shape collector was used. The distance between the collector and emitter was varied between 1.5mm to 4.5mm, with all the other parameters kept constant. A set of simulations was considered with different collector lengths while the electrode gap was maintained at 2.5mm, similar to the base case.

In another set of simulations the effect of the collector geometry was analyzed. A pin shape collector having a cylindrical shape with 1mm diameter was considered. The pin length, the distance to the emitter, and the collector length were varied. The pin length was between 1mm to 8mm, while the gap was varied between 1.5 to 4.5 mm. Finally,

two- and three-stage pumps were considered with different collector lengths and electrode gaps which corresponded to the best performance for the single-stage pumps.

7.4.2 Simulation Results

The simulation results for the single-stage pump are presented in Table 7.7. The first four lines show the simulation results for different electrode gaps. The collector length and shape were the same as the base case (grayed line in the table). The next set of 3 simulations present the results for the collector length variations. The gap was maintained at 2.5mm. Next, the collector shape was considered. The next set of eight simulations shows the effect of the electrode gap and collector length variation on the pumping head and mass flow rate performance for the pin shape collector. First, the electrode length was varied from 1mm to 8mm while the gap was maintained at 2.5mm. Next, the electrode gap effect was obtained by considering gaps from 1.5 to 4.5mm with a pin shape collector length of 4mm. The last case run was a combined pin and ring collector with a gap of 3.5mm. The pin length was 6mm. The ring shape collector was 4mm long.

Table 7.7 The parametric study results for the single-stage pump

Collector [mm]	Gap [mm]	DP [Pa]	M [g/s]	q [ml/min]
Gap effect				
2	1.5	1.05	0.99	73
2	2.5	1.08	0.95	71
2	3.5	1.11	0.97	72
2	4.5	1.02	0.92	68
Collector length effect				
6	2.5	1.21	1.01	75
4	2.5	1.15	0.99	73
1	2.5	0.87	0.84	62
Pin (r=1 mm) collector				
1	2.5	0.39	0.50	37
2	2.5	0.58	0.64	47
4	2.5	0.93	0.85	63
6	2.5	1.07	0.92	68
8	2.5	1.14	0.95	58
4	1.5	0.88	0.81	60
4	3.5	0.96	0.87	65
4	4.5	0.99	0.89	66
Pin (r=1mm and 6 mm long) and collector				
4	3.5	1.23	0.94	70

7.4.2.1 The Gap Effect

The simulation results for the gap variation are presented in Figure 7.17. As the gap was varied from 1.5mm to 3.5mm the mass flow rate remained about the same (0.95g/s), while the pressure head increased from 1.05 to 1.11 Pa. For the 4.5mm gap the pressure head and the mass flow rate decreased in performance. The simulation results show that an optimum gap may be between 3.5mm and 4.5mm.

The gap distance can affect the performance because the electric field increases with the gap decrease. Although the electric field decreased as the gap was increased, the volume between the electrodes where active charges are located also increased, and thus a higher electric force may be obtained for a charge limited regime. Also, the direction of the jets

leaving the emitter tips towards the collector had a higher angle with respect to the vertical (cross-flow) direction, which decreased the amount of momentum transferred to the wall and increased the amount of momentum transferred to the fluid. These two considerations explain why initially the performance increased with the gap distance. When a threshold value was reached the electric field decreased such that the total force applied on the charges present inside the fluid decreased, becoming the dominant factor, and a decrease in the performance was observed.

7.4.2.2 The Collector Length Effect

Figure 7.18 shows the simulation results for the collector length variation parametric study. Four collector lengths were considered, from 1 to 6 mm. The figure shows that the pressure head and mass flow rate increased with the collector length. This trend is explained by the fact that a better charge collection is obtained as the collector length increases. This confirms also the assertion made at the beginning of this section that one way to improve the pumping performance is to improve the charge collection.

7.4.2.3 The Collector Geometry Effect

Further insight into the charge collection improvement can be obtained by considering a new geometry for the collector. The collector shape analyzed was a cylindrical pin with a 1mm radius. This design directed the charges towards the middle of the channel, which minimized the jet momentum exchanged with the wall. At the same time, the charge jets acted in a region where the flow velocity was higher according to the laminar profile. Figure 7.19 shows a performance increase with the pin collector length. Still, the pumping performance obtained from a pin shape collector was relatively lower than the one obtained from the ring shape collector, which shows that for better performance the

charge jets should be directed towards the wall to act in the regions where the fluid velocity is lower and thus transfer their momentum more efficiently.

A last case was considered with both collector geometries in place. The gap and collector length parameters were chosen such that to obtain the best performance. As seen in the last line of Table 8.8, this geometry provided a better performance than the other, reaching a pressure head of 1.23P and a mass flow rate of 0.95Pa.

This last case shows that design modifications can provide a performance increase of about 25% with respect to the base case tested.

7.4.2.4 The Multiple Stage Parametric Study

The last set of simulations considered was for the multistage parametric study. The parameters considered were the number of stages, the collector length and the stage gap.

The first case considered (shown in the first line of Table 7.8) was a two-stage EHD pump with the base case parameters. The stage gap was 12mm. The results show an increase in the performance with respect to the single–stage case of about 18%. The effect of the stage gap variation was determined from the next two cases considered where the number of stages was 2, the collector length was 6mm, the electrode gap 2.5mm, and the stage gaps 5 and 8mm. The best pumping performance was obtained at a stage gap of 8mm. In this case the pressure head was 1.39 Pa, and the mass flow rate reached 0.8g/s.

The three-stage simulation showed improved performance with respect to the single-stage case but no net improvement with respect to the two-stage case. Still, the internal pressure drop for the multi-stage cases increased with the number of stages.

The above results show that clusters of two-stage pumps would provide best performance for the EHD pumping of liquid nitrogen.

Table 7.8 The parametric study results for the single-the three-stage pump

Stages	Collector [mm]	Electrode Gap [mm]	Stage Gap [mm]	DP [Pa]	m [g/s]	q [ml/min]
2	2	2.5	12	1.12	0.75	56
2	6	2.5	5	1.22	0.80	59
2	6	2.5	8	1.39	0.79	58
3	2	2.5	8	1.09	0.63	47

7.5 SUMMARY

This chapter presents the simulation of single- and multiple-stage EHD pumping using liquid nitrogen. First the problem set-up is presented. Then the simulation procedure and results for a single-stage and a three-stage EHD pump are presented. The electric field and flow solutions are given. For a single-stage pump the maximum electric field where the charge emission takes place ranged from 220MV/m to 340MV/m when the applied voltage was varied between 12 to 18kV. The average electric field remained about the same. For the three-stage pump the maximum electric field had a relatively higher value of about 530MV/m.

The flow solution shows that the pressure head and mass flow rates obtained using a single-stage pump range between 0.8 to 1.22Pa and 0.8 to 1.02 g/s when the applied voltage ranges between 12-18kV. The three-stage pump presented in section 7.3 shows a very small improvement in performance.

A parametric study was used to determine which design parameters changes would result in a better pumping performance. The parametric study shows that using a longer collector as well as placing a pin shape collector axially could provide better charge collection. This way the pumping performance may be improved by about 25%. Further improvement can be obtained using a multi-stage design. The simulations show that a two-stage arrangement presents the optimum configuration.

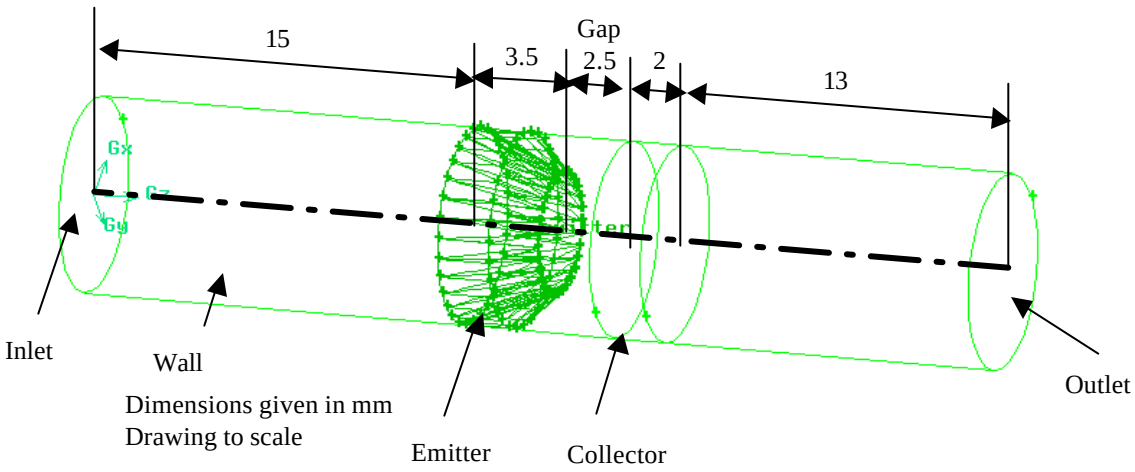

Figure 7.1 The numerical problem set-up for the single-stage EHD pump

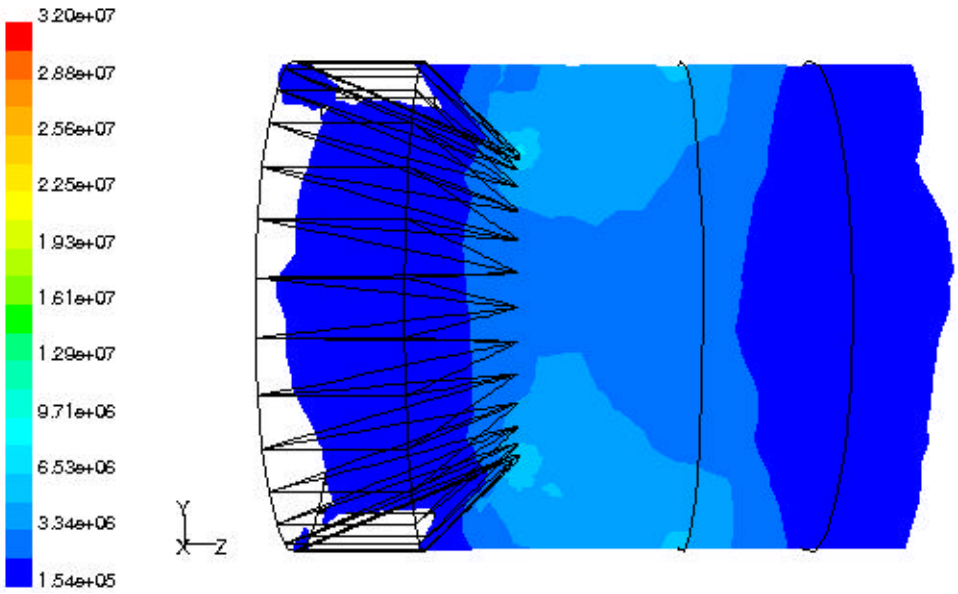

Figure 7.2 The electric field distribution (in V/m) for an applied voltage of 16kV and no charge density on the emitter (single-stage)

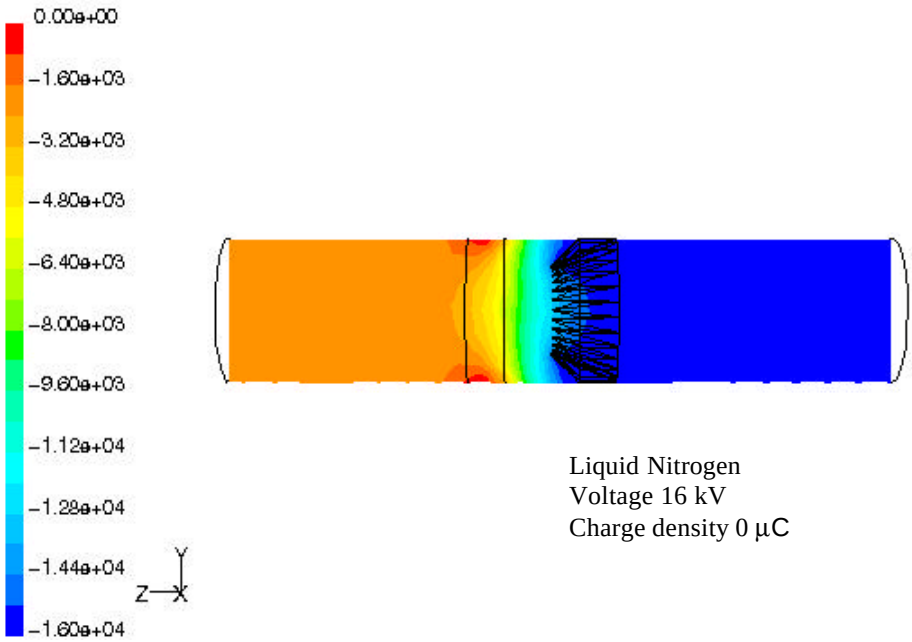

Figure 7.3 The voltage field distribution (in V) for the single-stage EHD pump

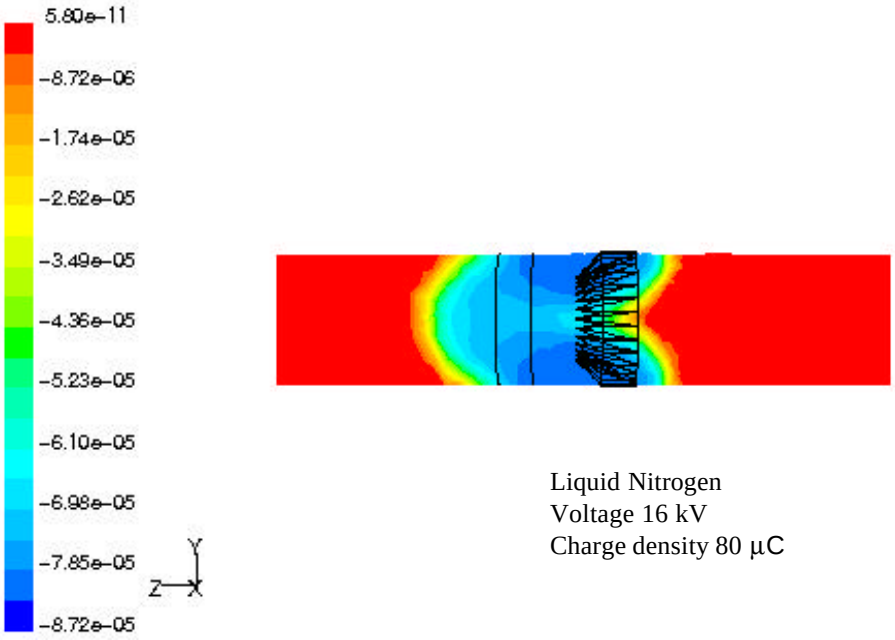

Figure 7.4 The charge density distribution (in C) for the single-stage EHD pump

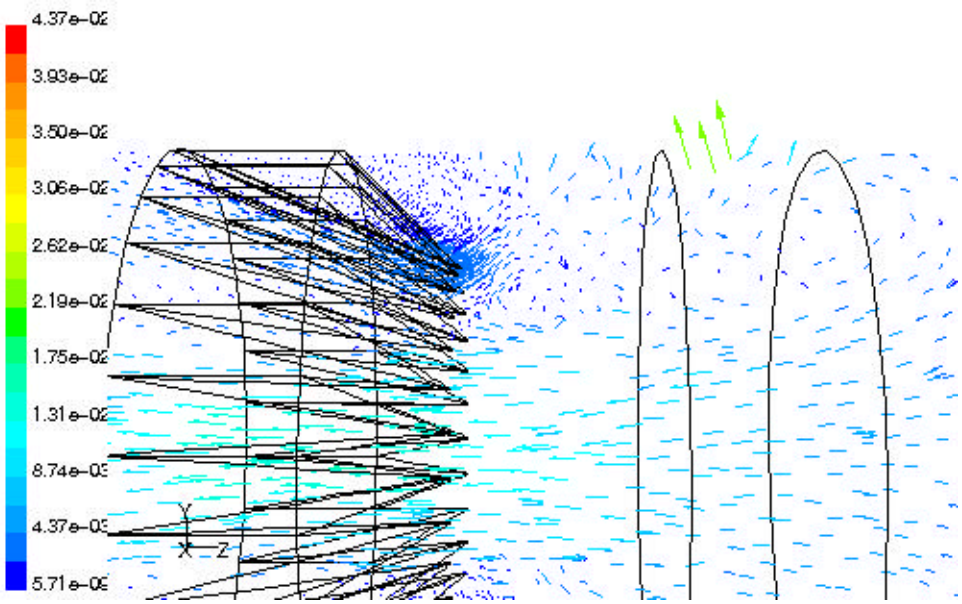

Figure 7.5 The velocity vectors (in m/s) for the confined channel flow solution (single-stage)

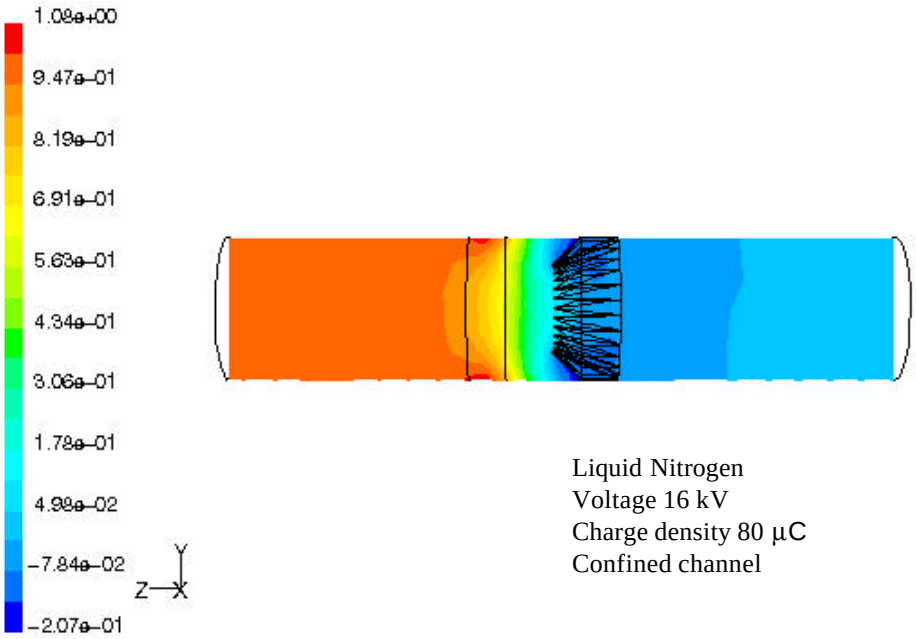

Figure 7.6 The pressure distribution (in Pa) for the single-stage EHD pump

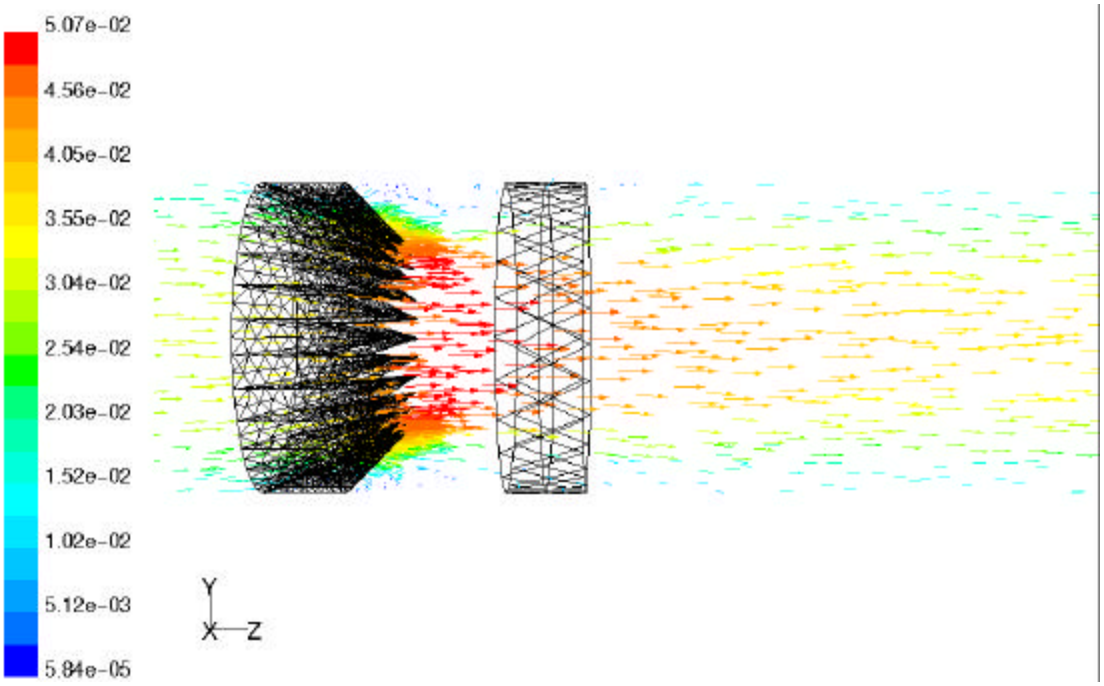

Figure 7.7 The velocity vectors (in m/s) for the open channel flow solution (single-stage)

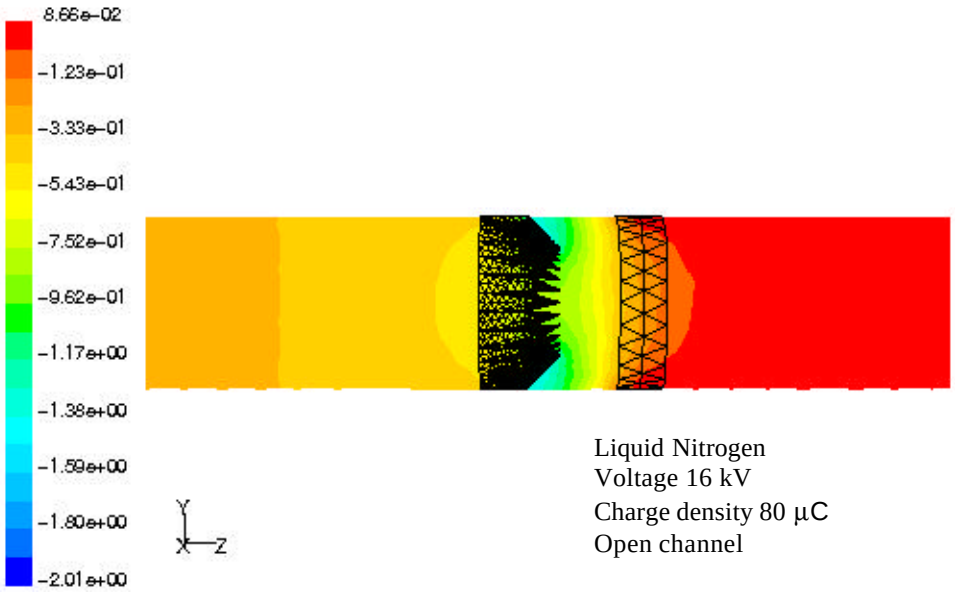

Figure 7.8 The pressure distribution (in Pa) for the single-stage EHD pump

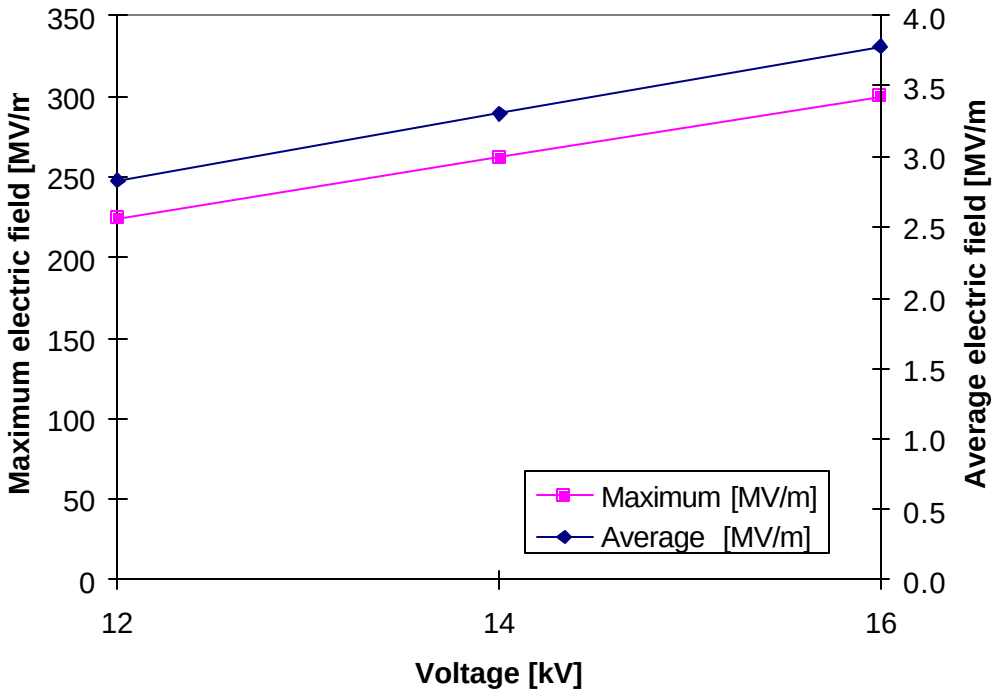

Figure 7.9 The maximum and average electric field intensity for the single-stage EHD pump

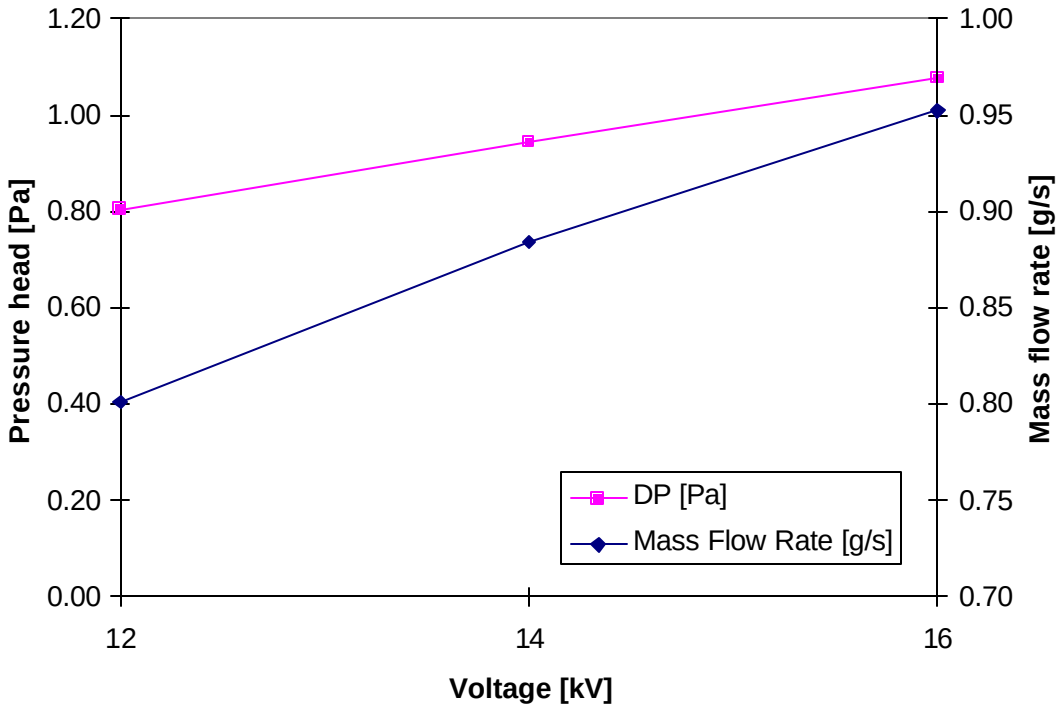

Figure 7.10 The maximum pressure head and the mass flow rate for the single-stage EHD pump

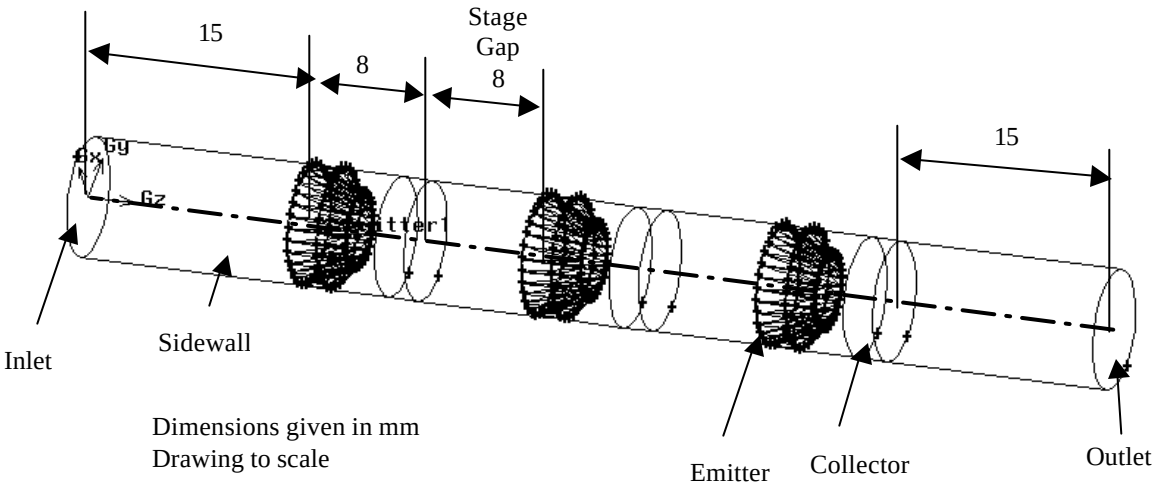

Figure 7.11 The three-stage EHD pump numerical set-up

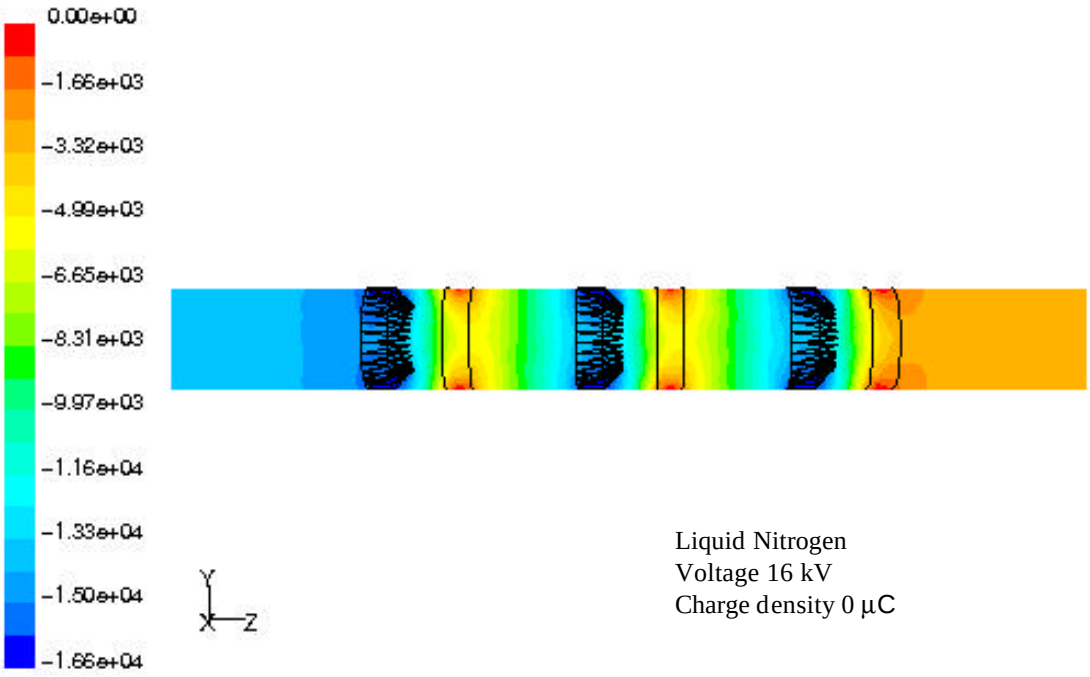

Figure 7.12 The voltage distribution (in V) for the three-stage EHD pump

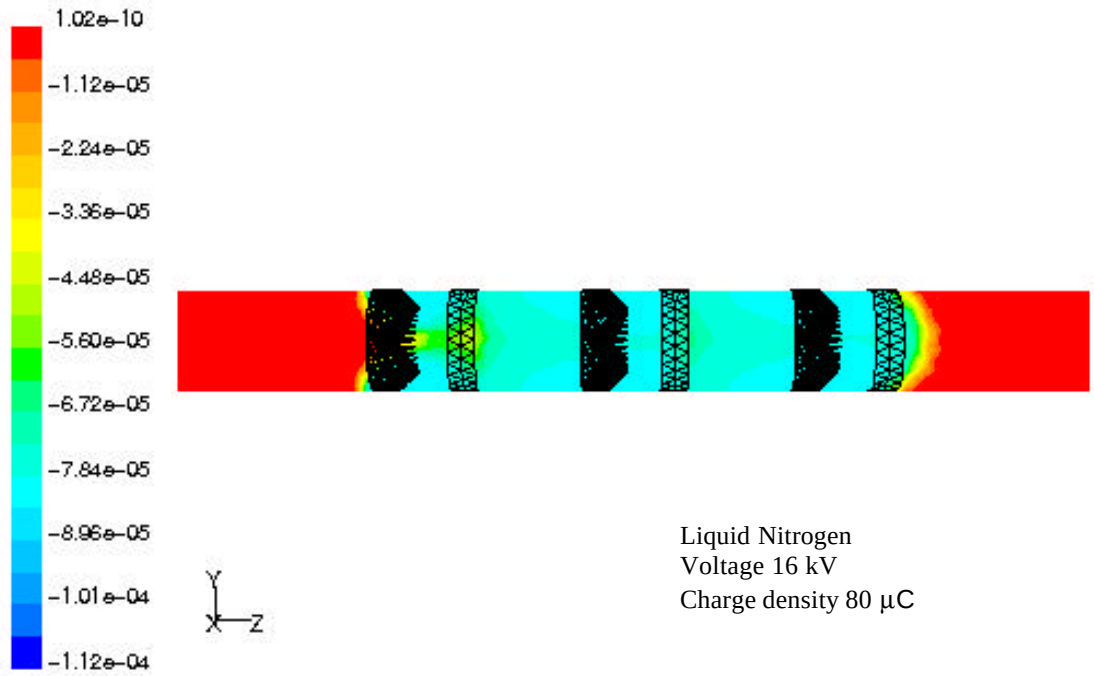

Figure 7.13 The charge density distribution (in C) for the three-stage EHD pump

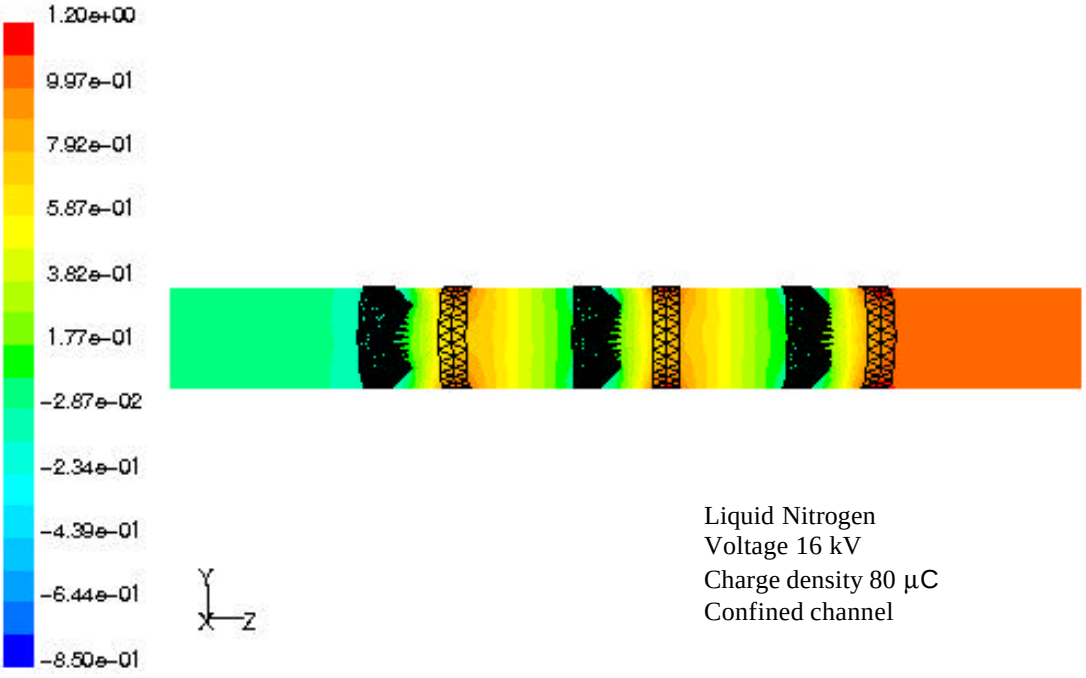

Figure 7.14 The pressure distribution (in Pa) for the three-stage EHD pump

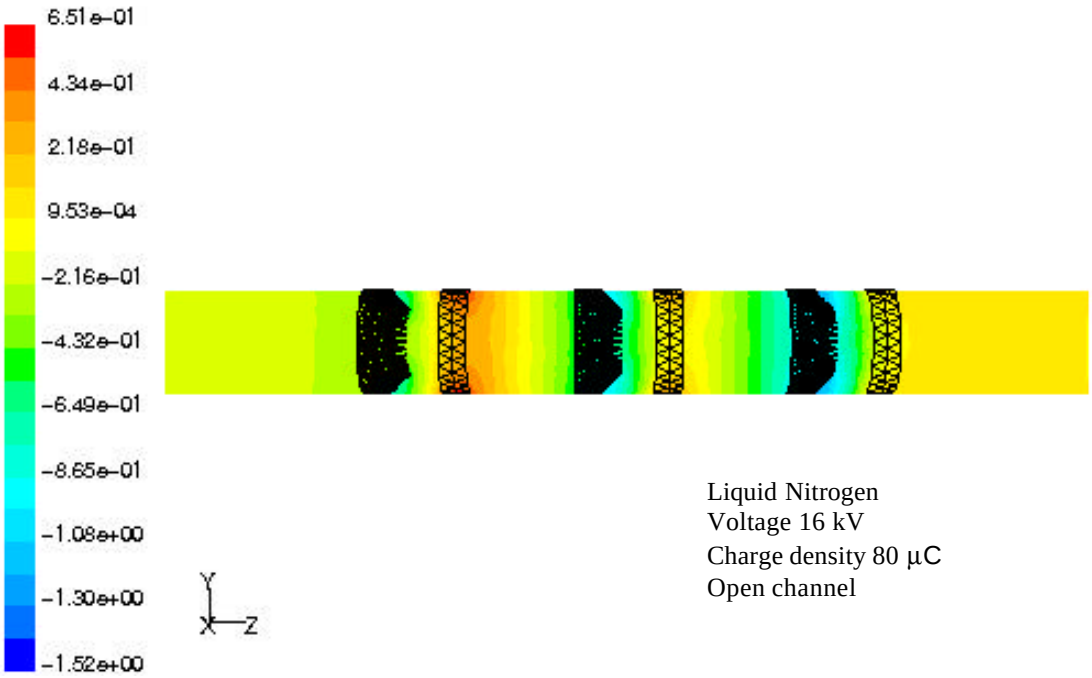

Figure 7.15 The pressure distribution (in Pa) for the three-stage EHD pump

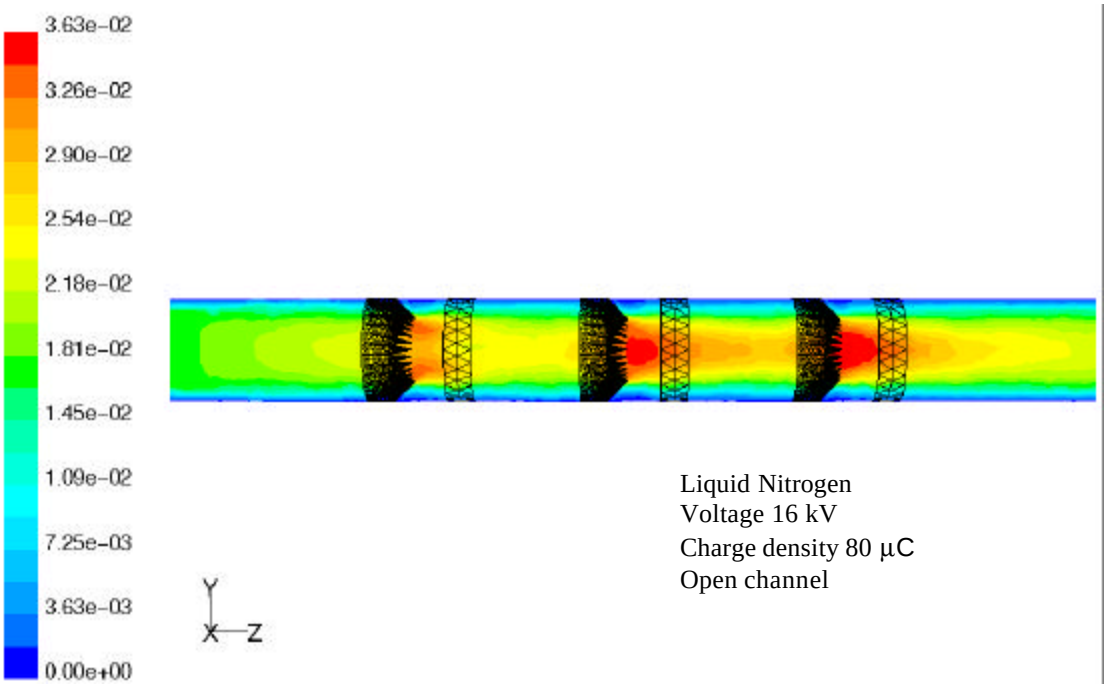

Figure 7.16 The velocity contours (in m/s) for the three-stage EHD pump

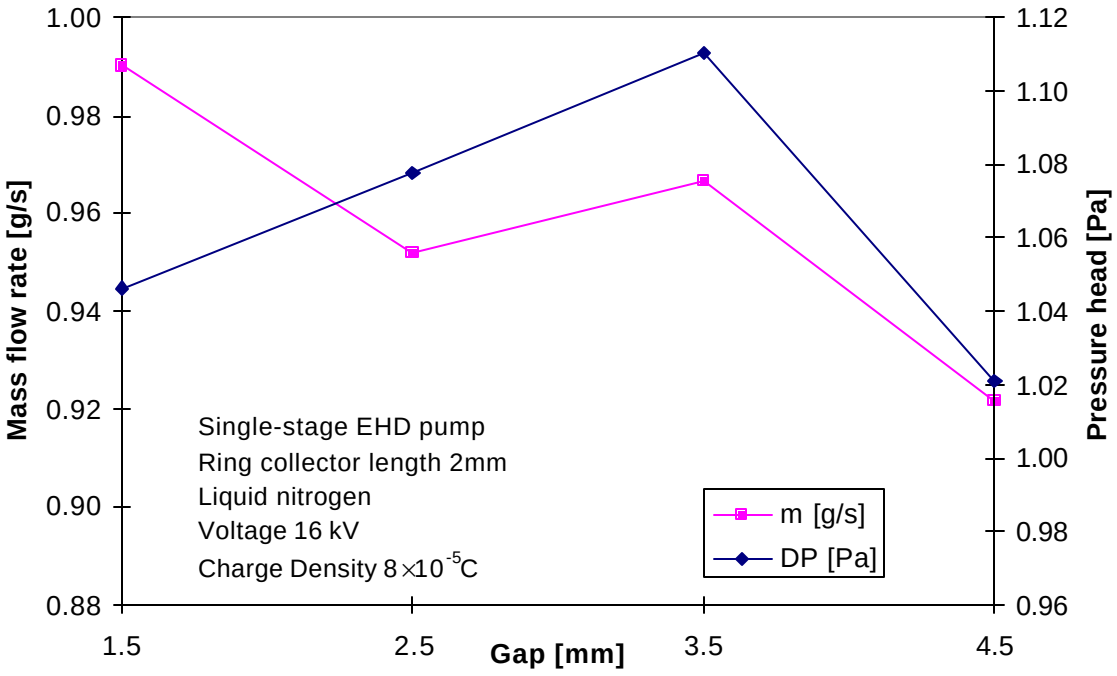

Figure 7.17 The mass flow rate and pressure head for different electrode gaps

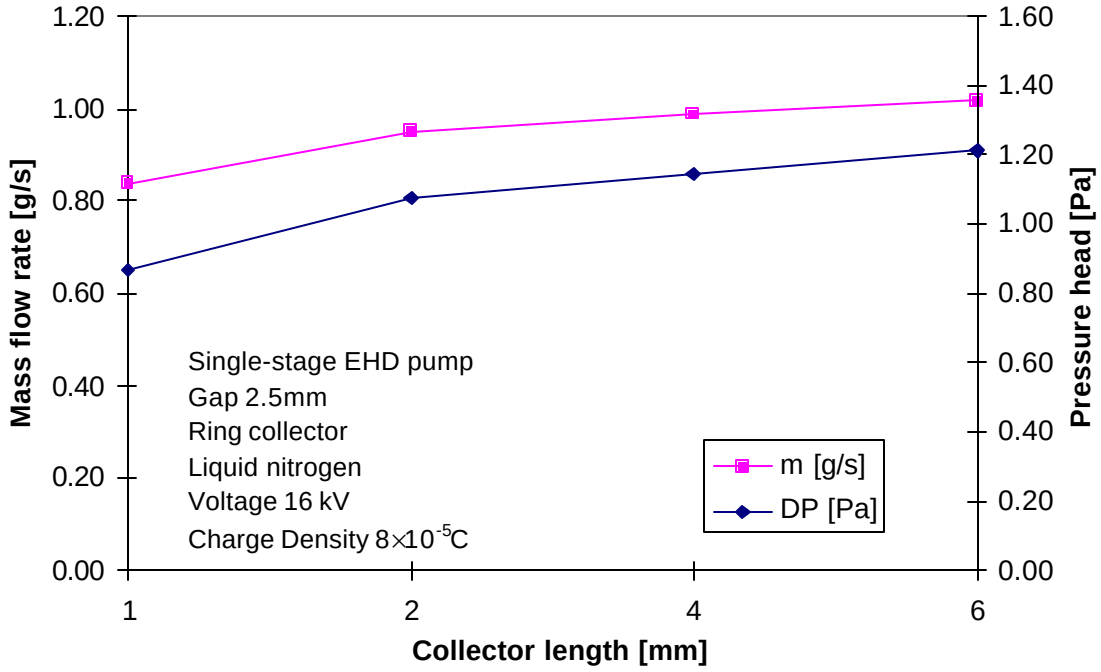

Figure 7.18 The mass flow rate and pressure head for different collector length

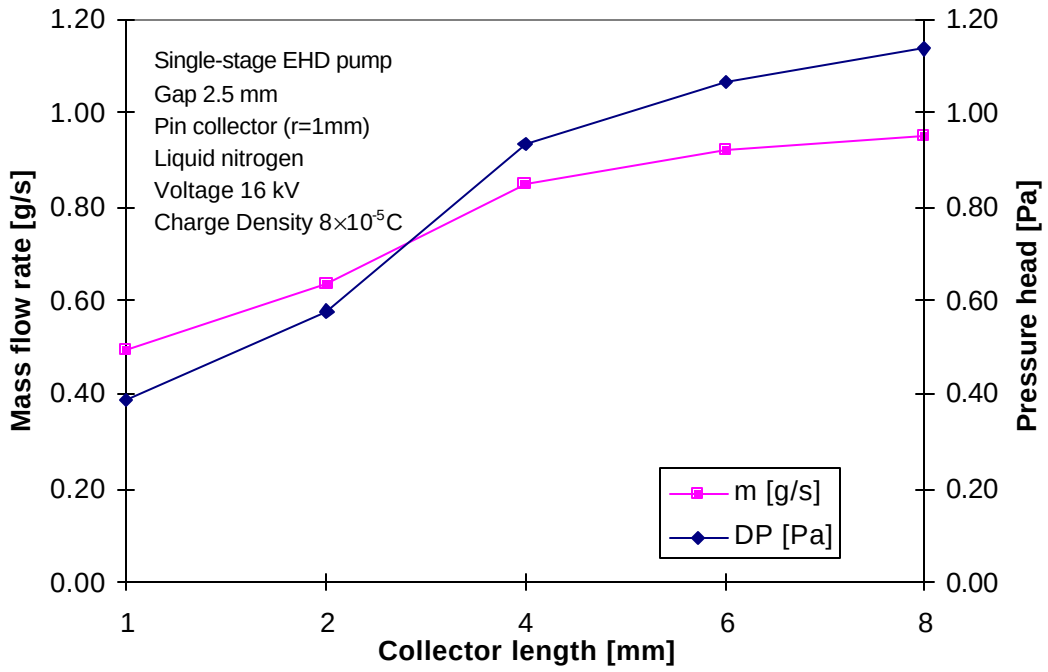

Figure 7.19 The mass flow rate and pressure head for different collector lengths (pin shape collector)

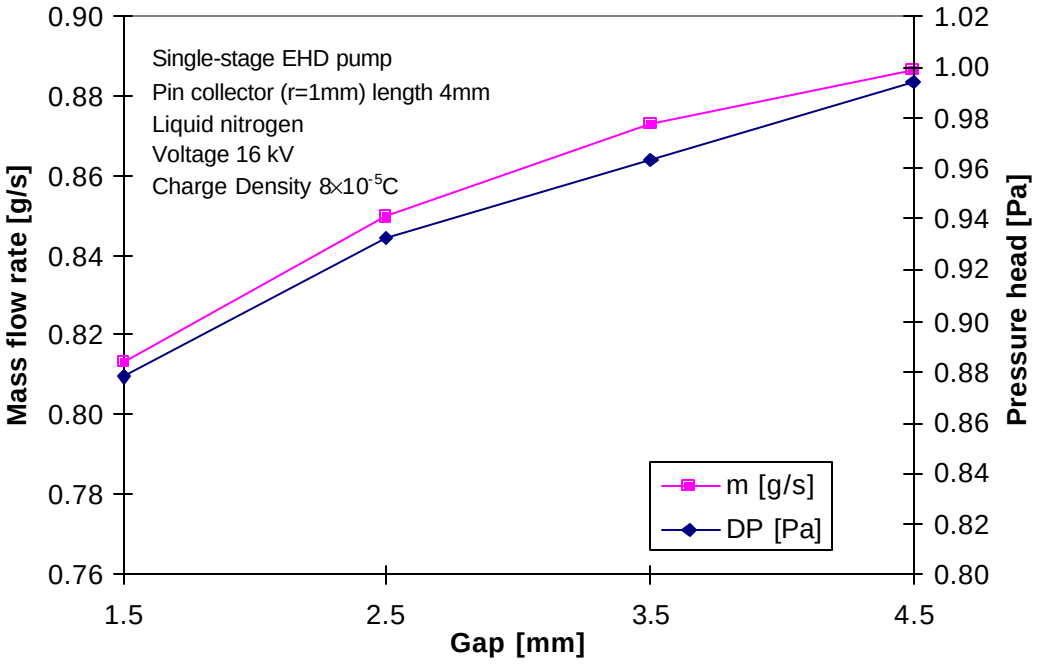

Figure 7.20 The mass flow rate and pressure head for different electrode gaps (pin collector)

CHAPTER 8 THEORETICAL ANALYSIS OF EHD PUMPING OF LIQUID NITROGEN

8.1 INTRODUCTION

The previous two chapters presented experimental and numerical results for EHD pumping of liquid nitrogen. In this chapter an analysis of the experimental and numerical results is presented. A pumping curve for the single stage pump is obtained such that a cooling system design can be made using it. First the electric parameters for the EHD pumping of liquid nitrogen are analyzed. The experimental electric field estimation is compared with the numerical one and a threshold electric field value for the charge emissions is determined. Next the fluid flow experimental and numerical results are presented and compared against each other. Finally, a series of pumping curves are determined from the available data.

8.2 ELECTRIC FIELD ANALYSIS

The maximum electric field intensity is obtained at the tips of the emitter. The threshold value at which charge emissions occur is important from a design point of view. Having a good estimate for the threshold voltage gives us an important design criterion for a given application.

8.2.1 Theoretical Estimation of Tip Electric Field

Coelho and Debeau (1971) proposed a theoretical estimation of the electric field distribution around the tip in a point-plane geometry. The hyperboloid approximation is used for the tip, which uses the following two equations to generate the tip:

$$x = a \sin \zeta \cosh \eta \tag{8.1}$$

$$y = a \cos\zeta \sinh\eta \tag{8.2}$$

where a is the distance between the focal point of the hyperbola and the plane, and ζ and η are the independent parameters defining the hyperboloid. It has been shown that if two of the generated hyperbolas are equipotential, then all of them are equipotential. Also, the voltage and the electric field have the following expressions:

$$\begin{aligned} V(\zeta) &= C \ln\tan(\zeta/2 + \pi/4) \\ E(\zeta,\eta) &= \frac{C}{a\cos\zeta(a\cosh^2\eta - \sin^2\zeta)^{1/2}} \end{aligned} \tag{8.3}$$

where the origin of the potential is taken at the plane x=0 (ζ = 0) and C is a constant depending on the applied voltage V. If the constant C is estimated, the following expression is obtained for the voltage field:

$$V(\zeta) \cong V\frac{\ln\tan(\zeta/2 + \pi/4)}{\ln(2/\varepsilon)} \tag{8.4}$$

The electric field on the tip axis (η=0), between the tip and the plane is given by:

$$\begin{aligned} E(X) &= \frac{aC}{X(2a - X) + (a - X)r} \\ \text{where } C &= \frac{V}{\ln\{2(a/r)^{1/2}\}} \end{aligned} \tag{8.5}$$

and X is the coordinate along the tip axis, a is the focal distance with respect to the plane, and r is the tip radius.

Thus, finally, the tip and plane electric field are:

$$\begin{aligned} E(0) &= \frac{C}{r} = \frac{V}{r\ln\{2(a/r)^{1/2}\}} \\ E_p(a - r/2) &= \frac{C}{a} = \frac{V}{a\ln\{2(a/r)^{1/2}\}} \end{aligned} \tag{8.6}$$

The area of the tip surface where the field is higher than a given value $E > E_0$ is obtained using:

$$A(E) = \frac{2}{3}\pi r^2 \left(\frac{E_0^3}{E^3} - 1 \right) \tag{8.7}$$

Figure 8.1 shows the above function variation for a tip radius of 10μm. The region around the tip where the electric field is 90% of the tip electric field, which is the maximum electric field, is very small (about $80\mu m^2$). This considerations support the assertion that the ion generation takes place at the tip of the emitter.

8.2.2 Liquid Nitrogen Threshold Electric Field

The presented model can be used to approximate the electric field at the tip if the pump is used in the liquid nitrogen EHD pumping experiments. The microscopic measurement of the emitter tips showed a radius of curvature of about 10 μm. The distance between the emitter tips and the collector was about 2.5mm.

In the experimental tests the voltage at which loop pumping of liquid nitrogen was observed was about 12kV.

Thus, the estimated critical tip electric field (see Equation 8.6) is given as:

$$E_{th} = \frac{V}{r \ln\{2(a/r)^{1/2}\}} = \frac{12kV}{10\mu m \ln\{2(2.5mm/10\mu m)^{1/2}\}} = 347\frac{MV}{m} = 347\frac{kV}{mm} \tag{8.8}$$

The above considerations allow us to determine that the threshold electric field for EHD pumping to be initiated is about 350kV/mm. This electric field corresponds to a charge emission high enough to produce fluid flow motion between the electrodes.

An injection law can be obtained from the assumption (Higuera, 2000) that the space charge, at distances of the order of magnitude of the tip radius of curvature, is of the order:

$$q_c = O(\varepsilon E_c / r_0) \tag{8.9}$$

where q_c and E_c are the orders of magnitude of the electric field and charge density at distances of O (r_0) from the tip of the electrode, r_0 is the radius of curvature of the electrode and ε the permittivity of the liquid. Thus, our first approximation is that the charge emission is proportional to the electric field strength. This is why as the voltage is increased the charge generation increases and eventually Coulomb forces acting on the charges will produce an ordered motion. Equation 8.6 shows a linear dependence of the electric field on the voltage, which shows that the charge emission also will vary linearly with the voltage, which produces a linear variation of the pumping with the voltage, as seen in the experimental tests (Figure 6.21) or in the numerical results (Figure 7.10).

The above results assume that there are no charges present between the emitter and collector and that the EHD pump geometry can be modeled with a tip-to-plane geometry. More accurate results are obtained from the numerical simulation of the electric field between the electrodes, which account for the presence of static charges and our specific geometry.

The numerical results for the electric field are presented in Figure 7.9. The maximum electric field for 12 kV is about 225 kV/mm. As can be seen in the figure, the presence of charges and the different geometry make the field smaller than in the case of a tip-plane geometry. Thus, we conclude that the threshold voltage for the charge emission in liquid nitrogen to produce EHD pumping in the tested configuration is 225 kV/mm.

Table 8.1 presents the maximum electric field for different voltages obtained from the tip-plane approximation and from the numerical simulations and the estimated tip area on which the charge emission takes place (where the electric field is higher than the

threshold voltage of 225KV/mm). As the voltage is increased, the maximum electric field increases and the charge emission area increases.

Table 8.1 The electric field parameters synthesis

Voltage [kV]	E tip-plane model [KV/mm]	E numerical [KV/mm]	$A(E_{th})$ [μm^2]
12	347	225	562
14	405	262	1015
16	463	300	1618
18	521	337	2393
20	579	375	3361

The literature shows that only a few authors have studied the threshold voltage for onset voltage in liquid nitrogen. A notable exception is Hernandez-Avila (1994), who determines experimentally the onset voltage for liquid argon and nitrogen using a point-plane geometry. The onset voltage, calculated using the tip-plane configuration model, is determined to be about 350 kV/mm for liquid nitrogen for a $x_i/r_p \sim 1$ where x_i is the avalanche length (length on which electrode avalanches are sustained) and r_p is the tip radius of curvature. He used a tip radius of curvature between 2-12μm. These results agree with our estimations.

8.3 PUMPING CURVE

Using the numerical simulations results, a pumping curve can be obtained for the liquid nitrogen loop EHD pumping tests. The pumping curve provides information on mass flow rate obtainable at a certain pressure drop imposed by the flow loop. The numerical simulation results for the two limiting cases for the single-stage EHD pumping of liquid nitrogen were presented in the Table 7.7.

Figure 8.2 presents the pumping curves obtained from the numerical simulations for the single-stage EHD pump at different applied voltages. The maximum pressure drop occurs

when no flow is present in the channel and thus is obtained from the numerical simulation results for the closed channel. The maximum mass flow rate occurs at no pressure drop between the inlet and outlet and corresponds to the numerical simulation case when the inlet and outlet pressures were imposed to be equal. The pumping capability of the EHD pump increases with the voltage.

For a specified voltage the operating point of the loop during the experiments is obtained by determining the pressure loss/generation during running. Then the pumping curve allows us to estimate the mass flow rate in the loop.

The specifically simulated configuration provides up to 1.36 g/s (1.34ml/s) or 1.08 Pa at an applied voltage of 20kV.

8.3.1 Loop Pressure Losses

The loop external pressure losses corresponding to the pressure drop occurring in the loop outside the pumping section between the two pressure ports is obtained by estimating the local and distributed pressure losses.

The laminar flow pressure losses in a pipe are given by:

$$\Delta p = \frac{64}{Re}\frac{L}{D}\frac{\rho V^2}{2} \qquad (8.10)$$

where Δp is pressure drop in the pipe, L and D are the pipe length and diameter, ρ and V are the density and the average velocity of the fluid, and Re is the Reynolds number. Using:

$$Re = \frac{\rho VD}{\mu} = \frac{4\dot{m}}{\pi D\mu} \text{ and } \dot{m} = \rho V\frac{\pi D^2}{4} \qquad (8.11)$$

we get the pressure drop function of the mass flow rate as:

$$\Delta p = 128 \frac{\mu}{\rho} \frac{L}{\pi D^4} \dot{m} \qquad (8.12)$$

The above equation shows a linear variation of the pressure drop with the mass flow rate for laminar flow.

To account for the distributed and local pressure drop an equivalent length is used:

$$L_e = L_d + L_l \qquad (8.13)$$

where L_d is the length which gives the distributed pressure drop due to the fluid friction with the pipe wall, and L_l is the length which gives the local pressure drops due to the pipe turns or cross-section variations. The first length is equal to the pipe length between the two pressure ports (0.496 m). Thus,

$$L_d = 0.496\,\text{m} \qquad (8.14)$$

and the local pressure drop can be estimated as (Perry & Chilton, 1973):

$$L_l = 9D \qquad (8.15)$$

For the liquid nitrogen loop this becomes:

$$\Delta p = 128 \frac{\mu}{\rho} \frac{L_e}{\pi D^4} \dot{m} = 128 \frac{0.000169\,\text{kg/ms}}{880\,\text{kg/m}^3} \frac{(0.496 + 9 \cdot 0.0077)\text{m}}{\pi (0.0077\text{m})^4} \dot{m} = 1246 \frac{1}{\text{m} \cdot \text{s}} \dot{m}$$

Table 8.2 presents the experimental mass flow rate obtained using the experimentally measured pressure drop. The values are close to the ones obtained in the numerical calculations. A comparison between the experimental and numerical results is presented in the next section.

Table 8.2 Liquid nitrogen EHD pumping mass flow rate based on the experimental pressure head

Voltage [kV]	DP [Pa]	Mass flow rate [g/s]
12	0.68	0.546
12	0.51	0.409
12	0.57	0.457
14	0.73	0.586
14	0.63	0.506
14	0.74	0.594
14	0.86	0.690
16	0.88	0.706
16	0.73	0.586
18	0.86	0.690
20	0.9	0.722
20	1	0.803

8.3.2 Comparison Between the Numerical and Experimental Results

To compare the experimental and numerical results we need to take into account the length differences between the two cases occurring in the pressure drop calculations. The numerical solution was obtained for a section with a length of about L_n = 36mm. The distance between the pressure ports during the experiments was about L_{exp} = 73mm. Therefore, in comparing mass flow rate results between the two cases we need to account for the additional pressure drop imposed by the distance between the pressure ports and the limits of the computational domain. To do this, the experimental pressure drop must be corrected with the pressure drop due to the additional length. So:

$$\Delta P_{extrapolated} = \Delta P_{exp} + \Delta P_{corr} \qquad (8.16)$$

where the $\Delta P_{extrapolated}$ is the extrapolated experimental pressure drop for the comparison, ΔP_{exp} is the experimental pressure drop, and ΔP_{corr} is the correction pressure drop, which is given by:

$$\Delta P_{corr} = 128 \frac{\mu}{\rho} \frac{L_{exp} - L_n}{\pi D^4} \dot{m} \qquad (8.17)$$

Using the experimental mass flow rate, we can find the corrected experimental pressure drop (Table 8.3 column 4) and compare it with the numerical pressure drop corresponding to the same mass flow rate obtained from the numerical pumping curve (Table 8.3 column 5). The error is estimated as follows:

$$\text{Error}\,\% = \frac{\Delta P_{exp} - \Delta P_{num}}{\Delta P_{exp}} \cdot 100$$

Table 8.3 presents the comparison between the numerical and experimental results for the pressure drops at the same mass flow rate.

Table 8.3 Comparison between the numerical and experimental pressure drop (DP) results

Voltage	Mass flow rate experimental	DP experimental	DP exp. extrapolated	DP numerical corr. for exper. mass flow rate	Error
[kV]	[g/s]	[Pa]	[Pa]	[Pa]	%
12	0.55	0.68	0.69	0.56	18
12	0.41	0.51	0.52	0.42	18
12	0.46	0.57	0.58	0.47	18
14	0.59	0.73	0.74	0.63	14
14	0.51	0.63	0.64	0.55	14
14	0.60	0.74	0.75	0.64	14
14	0.70	0.86	0.87	0.75	14
16	0.72	0.88	0.89	0.81	8
16	0.59	0.73	0.74	0.68	8
18	0.70	0.86	0.87	0.84	4
20	0.73	0.9	0.91	0.92	-1
20	0.81	1	1.01	1.02	-1

The numerical and experimental results agree within a maximum of 18 %. In most cases the numerical results are smaller that the experimental values because the numerical simulation does not take into account the inertial effect during charge transport. These effects are more important at lower voltages. Still, the experimental pressure drop measurement has an uncertainty of about 15%, which should be taken into account when comparing the results.

Figure 8.3 shows the comparison between the numerical and experimental pressure drops. The figure shows a good agreement between the experimental and numerical results.

8.3.3 Liquid Nitrogen EHD Pumping Curve

The above considerations suggest that the numerically obtained pumping curves presented in Figure 8.2 represent the pumping curves for the single-stage EHD pumping loop tested experimentally and allow us to predict with an accuracy of about 15-20% the liquid nitrogen mass flow rates for an imposed pressure drop in the loop. Figure 8.4 presents the pumping curve for the case when the loop was run at 16kV and the corrected pressure head was about 0.9Pa. From the pumping curve we obtain that the mass flow rate in the system was 0.7 g/s and the volumetric flow rate about 0.9 ml/s.

8.4 OPTIMUM PUMP DESIGN

In Chapter 8 a parametric study was presented which allowed us to construct a set of design optimizations. In this section these design optimizations will be used to present an optimum single-stage EHD pump configuration.

The optimized EHD pump design is presented in Figure 8.5. The pump design is similar to the one used in the experiments and presented in Chapters 6 and 7. Two bolted flanges connect the pump casing to the copper 3/8" pipe. The electrodes are separated from the casing by three Teflon parts. The main design differences are found in the collector design and the distance between electrodes.

As concluded in the previous chapter, one of the main directions in improving the pumping performance was the efficient collection of the charges. To obtain a much better charge collection the length of the collector was increased. Most importantly the shape of

the collector was also changed to increase the charge collecting capacity, which at the same time provided a low flow resistance. To the initial ring design a conical wire network was added. The new collector design is presented in Figure 8.6. The conical wire network was made from a very thin wire (1 mm diameter). The two circles composing the conical part had diameters of 7.7mm (internal diameter of 3/8" pipe) and 3 mm and were connected by 8 straight wires placed at even distances along the circles. The distance between the circles was about 10mm.

Figure 8.7 presents the single-stage optimized EHD pump drawing. Two of the most important distances are given. The first dimension is the collector length, which was increased to about 12mm. The second dimension gives the electrode gap, which was increased to about 3.5mm. These distances were selected based on the parametric study result. The presented design should provide considerably improved pumping performance since it is based on optimization of some of the most important design parameters.

8.5 SUMMARY

This chapter presented some of the most important conclusions regarding the EHD pumping of liquid nitrogen. First, it was found that the minimum electric field required for the charge emissions in liquid nitrogen to occur is around 225kV/mm. Next, based on the comparison between the numerical and experimental results, an EHD pumping curve for liquid nitrogen was presented. These results allow us to design an EHD pumped liquid nitrogen cooling system. Finally, a better design for a liquid nitrogen EHD pump was proposed. This design was optimized based on a parametric study and will allow significantly improved pumping performance.

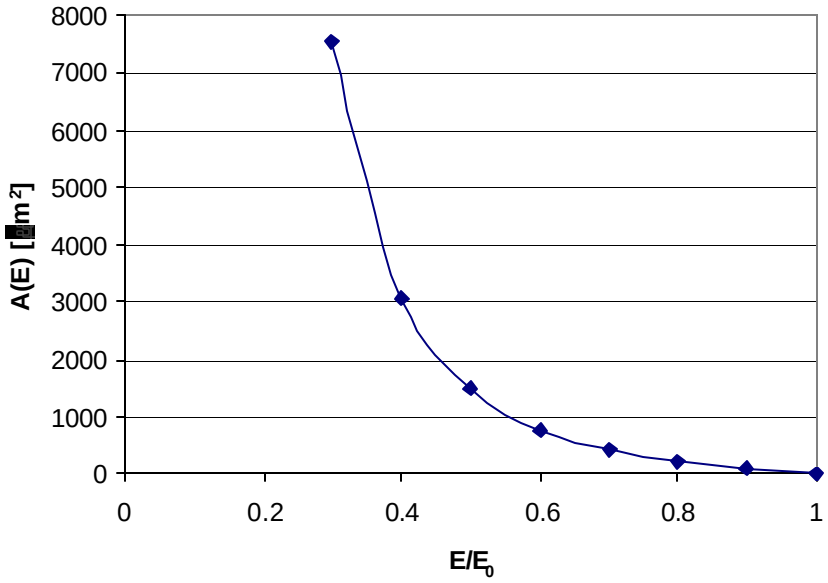

Figure 8.1 The tip area having the electric field higher than the E/E_0 value (E_0 – tip electric field, tip radius r = 10μm).

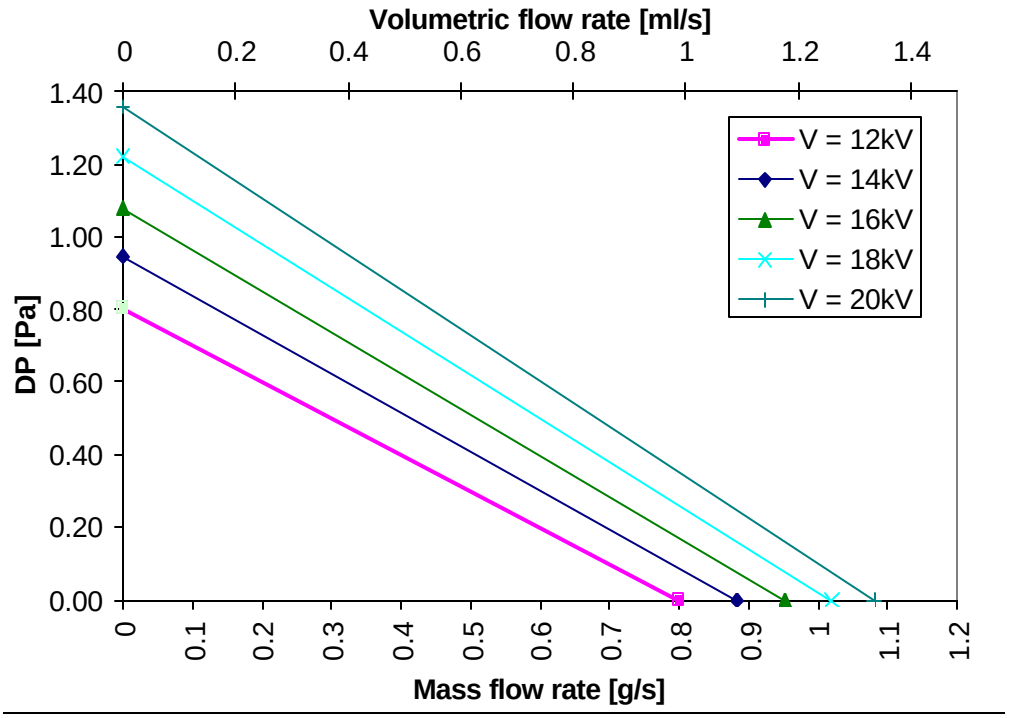

Figure 8.2 Pumping curves obtained from the numerical simulations for the single-stage EHD pump

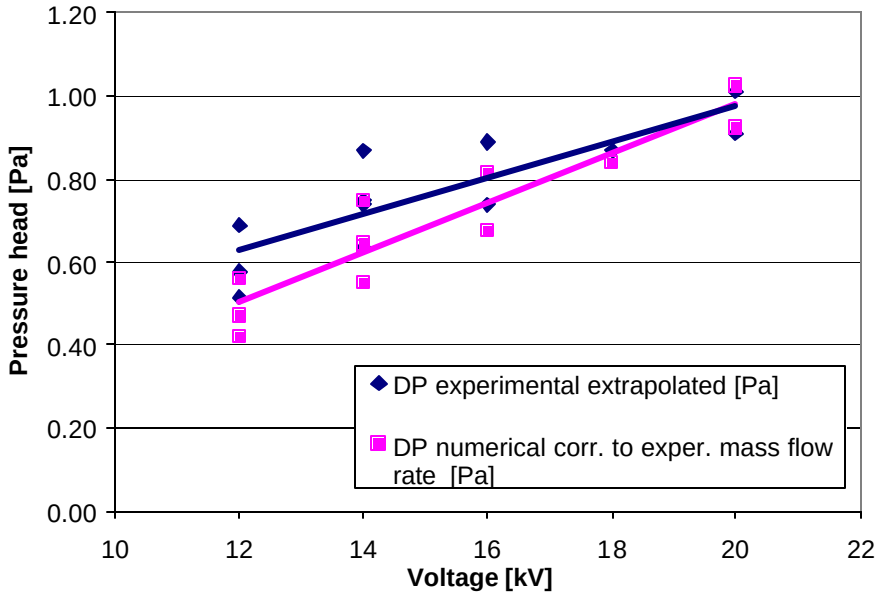

Figure 8.3 Comparison between the numerical and experimental results

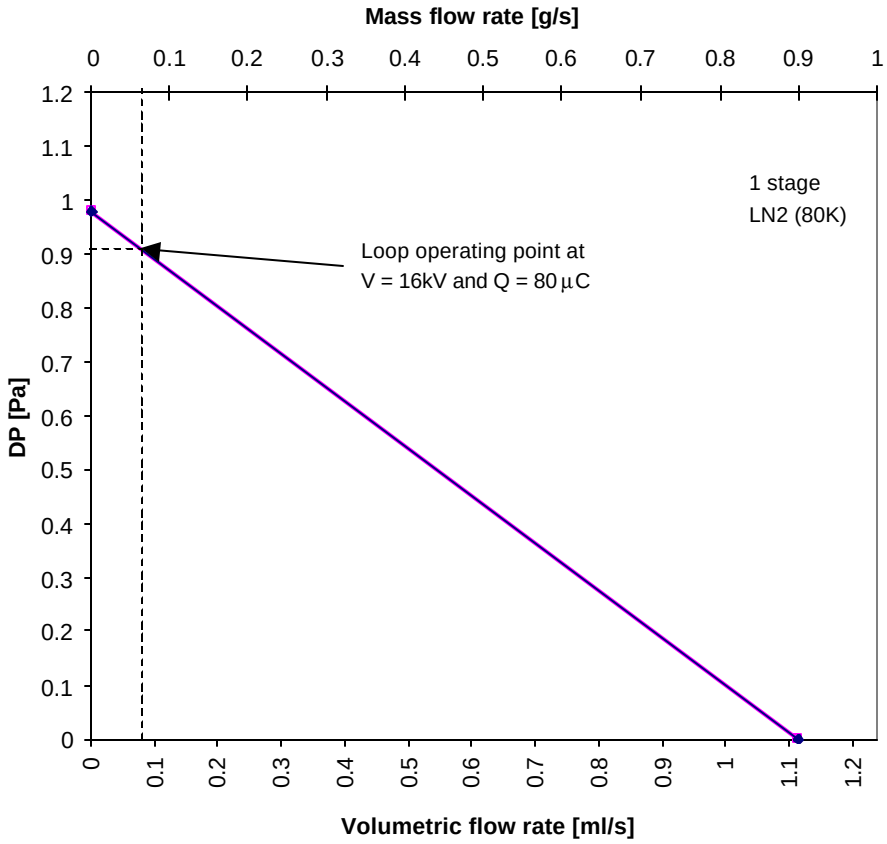

Figure 8.4 Pumping curve for the EHD pump and the operating point during the experiments (numerical simulation)

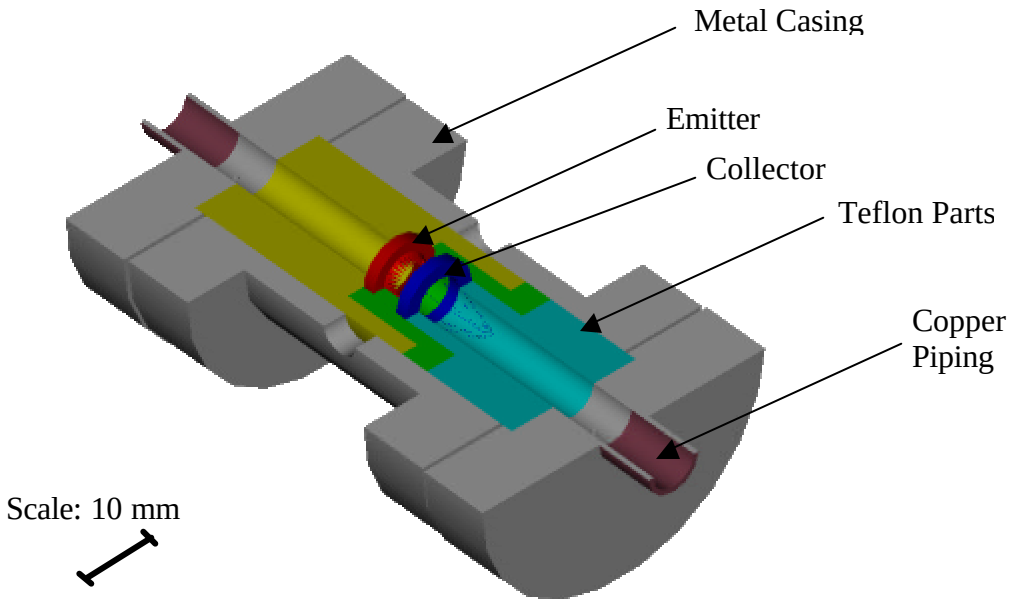

Figure 8.5 Optimized single-stage EHD pump (drawing to scale)

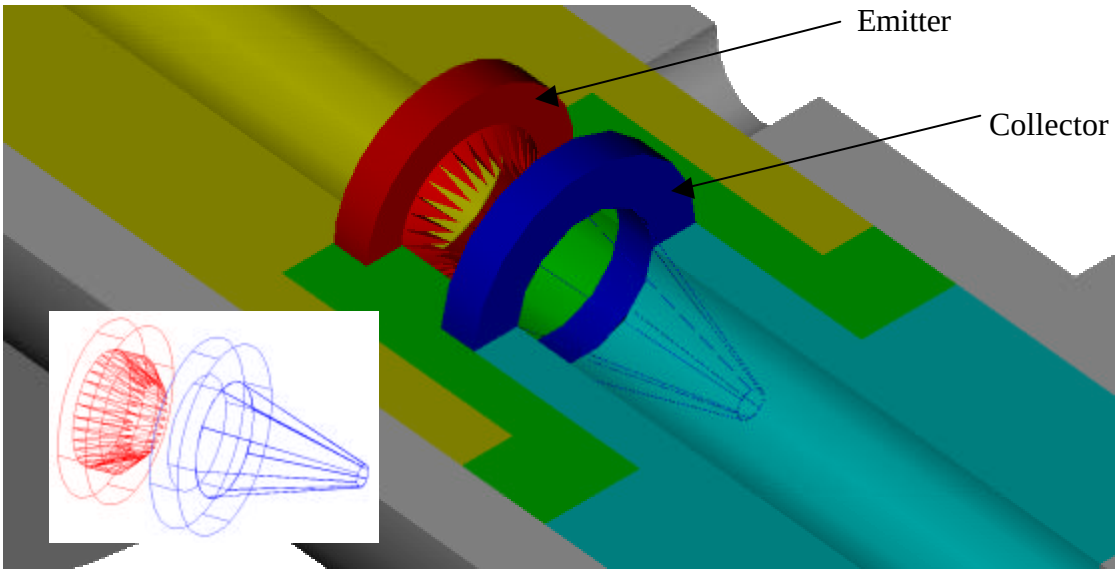

Figure 8.6 Optimized single-stage EHD pump (detail)

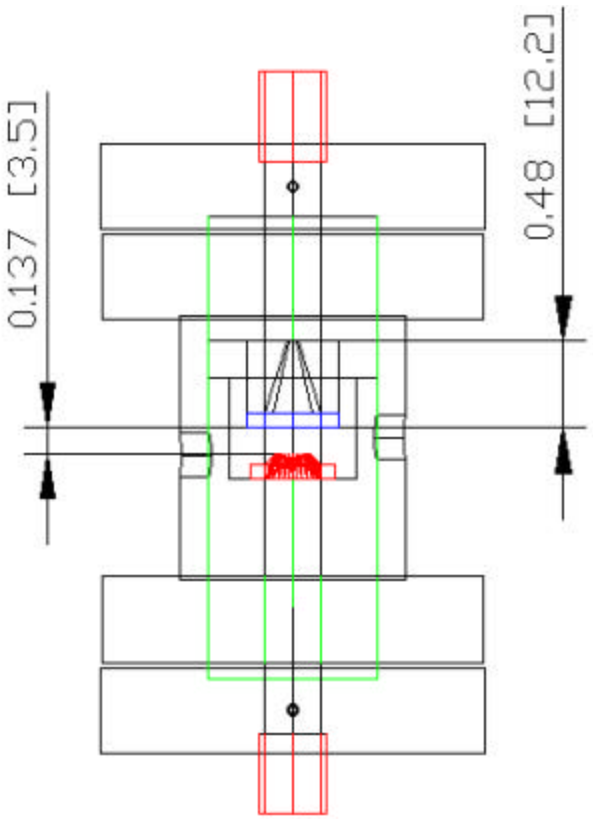

Figure 8.7 Single-stage optimized EHD pump drawing (dimensions in inches [mm])

CHAPTER 9 OVERVIEW AND RECOMMENDATIONS FOR FUTURE WORK

9.1 INTRODUCTION

In this study the applicability of the EHD technique for the cryogenic liquids pumping has been investigated for the first time. It is also the first of its kind to address the feasibility of combining EHD pumping technology with the cryogenic heat transfer to develop a cooling device for cryogenic spot cooling of electronics. Utilization of cryogenic liquid EHD pumping, which provides a controllable, low temperature, and very efficient means of heat removal, has a proven potential to be applied in various pumping applications including miniaturized cooling systems, mass transfer or flow management systems. Using this technique can substantially increase the cooling capacity controllability and potentially lead to substantial weight/volume reduction in many cryogenic thermal management systems. The overall findings of this research work include the experimental investigations at meso-scale for a cryogenic EHD pumping system followed by a numerical analysis, both of which contribute to a better understanding of the EHD pumping mechanism while representing a useful simulation tool for design and prediction of such systems.

9.2 OVERVIEW AND CONCLUSIONS

The first objective of this project was primarily to investigate the feasibility of an EHD micropump and to determine the main geometrical parameters that affect its pumping performance. To reach this aim a series of different micropumps were designed, constructed and tested. Based on the experimental results a better understanding of the EHD pumping at microscale was achieved, and a series of design recommendations was

developed. The second objective of the project involved a new and promising technique to provide cryogenic liquid pumping using EHD. The second setup involved a meso-scale EHD pumping unit, used initially to evaluate its pumping capability in a series of room temperature experiments in vertical and loop configurations. A series of cryogenic EHD pumping tests were further performed. The pumping performance of the device is the first reported systematic study of EHD cryogenic pumping. The results for the first time verified the feasibility of a cryogenic EHD pumping system. The experiments showed pumping capabilities significantly lower than the room temperature liquids, as expected. Still, the pumping performance obtained is sufficient for most of the cryogenic cooling applications, thus presenting a very strong potential for spot cooling of certain electronics. To facilitate understanding of the EHD pumping mechanism as well as for performance prediction and design/optimization purposes, a numerical model was used to analyze the EHD fluid flow and electric field parameters. This analysis has produced a series of recommendations for better designs, which would improve the pumping performance of the EHD pumping device. The field state of the art has been critically reviewed, and a comprehensive survey of the open literature has been provided. An overview of the results for each of the specific areas studied is given in the sections that follow.

9.2.1 EHD Micropumping Results

The focus of the first part of this study was to quantify the pumping capability of an EHD micropump that could be used in cooling of select electronics such as superconducting devices with applications to sensors and detectors and to determine the main design parameters influencing its performance. The main objective was to get a better

characterization of the microscale EHD pumping phenomenon and to develop understanding to improve its performance. Four different configurations were designed, fabricated, and successfully tested in the vertical pumping orientation. The optimal geometric parameters were identified and analyzed for each design and the fundamental EHD pumping mechanism are now better understood.

The base case (straight electrode design) experimental results were compared with the open literature, and good agreement was found. The comparison verified our setup and test methodologies. Three new electrode configurations were proposed for the first time, and they showed important performance enhancement with respect to the results reported in the literature and with respect to the base case. Based on the results, the following remarks can be made:

- As expected, the planar design (base case – similar to the designs proposed in the literature) presents the lowest performance.
- The first non-base case design uses a saw-tooth geometry for the emitter. The pumping head for the straight electrodes configuration is 600Pa at about 900V, while in the case of a saw-tooth configuration only about 200 V are needed to obtain the same pumping head. This improved behavior can be explained by the enhanced ion injection efficiency associated with the saw-tooth electrode design. In the planar configuration the ion injection sites are located at the tip of the planar electrode edge irregularities, while in the case of the saw-tooth geometry individualized and evenly distributed injection locations are provided.
- A bumped saw-tooth configuration was also proposed. The pumping head results obtained with this design show that the presence of the 3D bump structures could

significantly improve the pumping performance. It was observed that for the no-bump geometry, a pumping head of 500 Pa was obtained at a voltage of 1000V, whereas this same pumping head could be obtained for the bump geometry at less than 500 V for the same gap.

- The third, and seemingly the most optimized one, represented a combination of saw tooth emitter and a 3-D solder-bumps structure. Using a 3M fluid the micropump with a gap of 100 μm and a saw-tooth emitter configuration with bumps at an applied voltage of about 500V provided a pumping head of 750 Pa.

The results of the experiments successfully validated the new concepts, showing that adding a saw-tooth electrode geometry combined with 3-D structures provides a significant increase in the pumping performance. The results successfully confirmed that reducing the electrode gap, which allows also increasing the number of pumping stages, could significantly improve the pumping capability. Based on the results of this study optimum configurations can be designed depending on the application requirements.

9.2.2 Mesoscale EHD Pumping Results

An experimental investigation was undertaken in this study to determine the feasibility of applying the EHD pumping technique to the cryogenic liquid pumping. The results of the experiments successfully validated the concept, and a liquid nitrogen EHD pumping curve was determined. First, a new design mesoscale pump suitable for cryogenic liquids EHD pumping tests was designed and build. This pump was placed in a cryogenic pumping loop. Setting up the cryogenic testing system and its successful operation was in itself a major challenge and required innovative design strategies and several month of work. The preliminary tests of the pump involved room temperature liquids. Vertical and

loop tests were performed with two room temperature liquids (R-134a and HFE 1500). The results showed the significant pumping capability of the pump in room. In addition, a complex set-up and procedure were designed to allow cryogenic tests of EHD pumping to be performed. These tests proved the cryogenic pumping capability of the EHD pump. Pumping heads of up to 1 Pa with mass flow rates of 0.8g/s were achieved. Although the pressure head results seem relatively small, the corresponding liquid nitrogen mass flow rate meets the targeted heat removal requirements specific to superconducting sensors and detectors.

9.2.3 Numerical Modeling

A numerical model was used to simulate the electric and fluid flow characteristics of the cryogenic EHD pumping. The numerical model computes voltage, charge density and electric field strength distribution as well as the pressure and velocity fields for the EHD fluid flow. The agreement between the numerical modeling and experimental data is fairly good (within 18%), allowing us to validate the simulation procedure. The numerical simulations have also been used to perform a parametric study to determine the main ways to improve the pumping performance of our design. The numerical modeling procedure used in this study along with the experimental results will assist in further development and design optimization of cryogenic spot cooling devices.

9.3 RECOMMENDATIONS FOR FUTURE WORK

The future work recommendations will be divided in two parts according to the contributions presented in this work: (1) conventional (non-cryogenic) microscale EHD pumping and (2) cryogenic EHD pumping.

9.3.1 Non-cryogenic Microscale EHD Pumping Recommendations

Future work on the EHD micropumping will be further divided between basic and applied research.

In the area of the basic research a number of issues need to be addressed. These include conducting more fundamental studies to improve understanding of the mechanisms of electric field coupled fluid flows, quantifying the contributions of the various mechanisms, and developing a comprehensive computer simulation model with the aid of flow visualization studies. More specific directions the research might take could include theoretical estimation of the minimum and optimum gap, theoretical estimation of optimal electrode height, and radius of curvature.

In the field of the applied research, areas of interest that were determined during the course of this study and need further investigation are presented in the order of their importance:

- Investigation of the possibility of increasing the pumping performance by decreasing the electrode gap is another area that needs further research. Although this is a very attractive option, an optimum gap is expected below which the pumping performance will degrade; therefore an optimum electrode gap should exist. The electrode EHD jet momentum transfer as well as the electric characteristics (breakdown) could be affected by the gap decrease such that this optimum is expected to exist.
- Investigation of use of an optimum EHD pumping fluid which would combine very good heat transfer properties with favorable electrical properties to achieve higher EHD pumping performance.
- Improvement of packaging solutions by:

- designing in-line ports which would decrease the pressure losses due to the actual turns;
- using substrate materials with excellent conductivity to allow for a better heat transfer to the cooling surface;
- developing packaging solutions that will allow the use of active pumping substrates on both faces of the cold plate module package, which should allow a significant improvement in the pumping performance.

- Integration of the EHD micropump in a liquid cooling device used in electronic cooling. Of interest are:
  - The effect of any electromagnetic interference induced by the electric field on the global performance of the cooled electronic device.
  - The limitations encountered when this cooling device is integrated into an actual electronic device.
- Characterization of the long-term operation of the micropump: a series of studies addressing the effect of impurities on the fluid properties and on the electrodes would be very useful for developing industrial applications of EHD micropumps.

9.3.2 Cryogenic EHD Pumping Recommendations

Future work recommendations for cryogenic EHD pumping can again be divided in two categories, one regarding basic research and the other applied research. In the area of the basic research the following issues need to be addressed:

- Fundamental study of the EHD pumping mechanism of cryogenic liquids. This would include:
  - Ion generation in cryogenic liquids;

- Metal/liquid interface phenomena;
- Ion behavior inside cryogenic liquids under the effect of strong electric fields.

➢ Fundamental studies on short term and long term effects of the electric field on cryogenic liquids.

In the area of applied research, the following are the future work directions listed in the order of their expected impact on the liquid nitrogen EHD pumping performance:

- Investigation of the effects of the working fluid properties. Working fluids with higher conductivities than liquid nitrogen are expected to have better pumping performance. These fluids can be obtained using mixtures of suitable, EHD friendly, cryogenic liquids.
- A study of the possibility of increasing the pumping performance by multistage pumping.
- Development of new EHD pump designs, which would allow better performance. In Chapter 8 a possible configuration was suggested.
- Further exploitations of the numerical simulation tools used in this study to develop and design pump configurations with better performance.

REFERENCES

Ahn, S. H., and Y. K. Kim, 1997, "Fabrication and Experiment of Planar Micro Ion Drag Pump," Proc. Transducers 97, 373-6.

Arii K, Schmidt W. F. “Current injection and light emission in liquid argon and xenon in a divergent electric field”, IEEE Transactions on Electrical Insulation Vol. EI-19 No. 1, p. 16-23, 1984

Asano K. and Yatsuzuka K., 1999, “Fundamental study of EHD pump with needle-cylinder electrodes”, 1999 Conference on Electrical Insulation and Dielectric Phenomena, p 785-788.

Atten, P, 1996, “Electrohydrodynamic Instability and Motion Induced by Injected Space Charge in Insulating Liquids”, IEEE Transactions on Dielectrics and Electrical Insulation, Vol. 3, No. 1

Atten P., B Malraison, and Zahn, M., 1997, “Electrohydrodynamic plumes in point – plane Geometry”, IEEE Transactions on Dielectrics and Electrical Insulation, Vol. 4, No. 6, p.710-718

Atrazhev V.M., Dmitriev E.G. and Iakubov I.T., “The Impact Ionization and Electrical Breakdown Strength for Atomic and Molecular Liquids”, IEEE Transactions on Electrical Insulation Vol. 26, No. 4, p.586-591, August 1991

ter Barke, H.J.M, Burger, J.F and Rogalla H., “Microcooling of low temperature electronics”, Proceedings of the 16th ICEC/ICMC, Japan, 20-24 May 1996

Bart S. F., L. S. Tavrow, M. Mehregany, and J. H. Lang, 1990, "Microfabricated Electrohydrodynamic Pumps," Sensors and Actuators A, A21, 193-7.

Barbini G., Coletti G., 1995, "Influence of Electrode Geometry on Ion-drag Pump Static Pressure", IEEE Transactions on Dielectric and Electrical Insulation, Vol. 2 No. 6, p. 1100-5

Bonifaci N., Denat A., Atrahev V. M., "Work Function for a HV Cathode in Nonpolar Liquids", IEEE Transactions on Dielectric and Electrical Insulation, Vol. 1, No. 4, p. 657, August 1994

Bonifaci N, Denat A. "Transport Phenomena in Point-Plane Geometry in Liquid Argon", International Conference on Conduction and Breakdown in Dielectric Liquids ICDL '96, Roma, Italy, p 37-40, 15-19 July 1996

Bryan, J.E., 1990, "An Experimental Study of Ion-drag Pumping in a Vertical Axisymmetric Configuration," Master's Thesis, Texas A&M Univ, College Station, TX.

Bryan, J.E and Seyed-Yagoobi, J., 1990, "Ion-drag Electrohydrodynamic Pumping Selecting an Optimum Working Fluid," Tenth International Conference on Conduction and Breakdown in Dielectric Liquids (Cat. No.90CH2812-6), p. 603, 316-22

Bryan, J.E and Seyed-Yagoobi, J., 1992, "An Experimental Investigation on Ion-drag Pump in a Vertical and Axisymmetric Configuration," IEEE Transactions on Industry Applications, v. 28, p. 310-16

Bryan, J.E and Seyed-Yagoobi, J., 1994, "Analysis of 2-dimensional Flow Fields Generated by a 1-Electrode-pair Ion-drag Pump," IEEE Transactions on Dielectric and Electrical Insulation, vol. 1, No. 3, p. 459-467

Castaneda J. A. and Seyed-Yagoobi J., 1991, “Electrohydrodynamic pumping of refrigerant 11”, 1991, IEEE Industry Applications Society Annual Meeting, vol.1, p. 500-3

Castellanos, A., 1998, *Electrohydrodynamics*, CISM Courses and Lectures no. 380, Springer, New York

Choi J. W. and Y. K. Kim, 1995, "Micro Electrohydrodynamic Pump Driven by Traveling Electric Fields," Proc. IEEE IAS, 2, 1480-4.

Coelho R. and Debeau J., 1971, “Properties of the tip-plane configuration”, Journal of Physics D: Applied Physiscs, 4, 1266-1280

Denat A., Jomni F., Aitken F., Bonifaci N., “Thermally and Electrically Induced Bubbles in Liquid Argon and Nitrogen”, IEEE Transactions on Dielectric and Electrical Insulation, Vol. 9, No. 1, p. 17, February 2002

Frayssines P.E., Lesaint O., Bonifaci N., Denat A., Devaux F., “Prebreakdown and Breakdown Phenomena Under Uniform Field in Liquid Nitrogen”, Proceedings of 14th International Conference on Dielectric Liquids (ICDL ’02), Graz (Austria), p. 139-142, July 7-12, 2002

Fuhr G., R. Hagedorn, T. Muller, and W. Benecke, 1992, "Microfabricated Electrohydrodynamic (EHD) Pumps for Liquids of Higher Conductivity," JMEMS, 1(3), 141-6.

Fuhr G., T. Schnelle, and B. Wagner, 1994, "Traveling Wave-driven Microfabricated Electrohydrodynamic Pumps for Liquids," IEEE JMEMS, 4(4), 217-26.

Gee N., Floriano A. M., Toshinori W., Huang S. S.-S. and Freeman G.R., 1985, "Ion and electron mobilities in cryogenic liquids: Argon, nitrogen, methane, and ethane", J. Appl. Phys. Vol. 57 (4) p. 1097,

Gerhold J., Hubmann M., Tesler E., "DC Breakdown strength of Liquid Nitrogen under different Voltage Ramp Conditions", Proceedings of 13th International Conference on Dielectric Liquids (ICDL '99), Nara (Japan), p. 445-448, July 20-25, 1999

Halpern B. and Gomer R, "Field emissions in liquids", Journal of Chemistry and Physiscs, Vol. 51, p 1048-1056, 1969

Hara M., Suehiro J., Matsumoto H., Kaneko T., "Breakdown characteristics of cryogenic gaseous Nitrogen and Estimation of its Electrical Insulation Properties", IEEE Transactions on Electrical Insulation Vol. 24, No. 4, August 1989

Hara M., Suehiro J., Maeda H., Nakashima H., "DC Pre-Breakdown Phenomena and Breakdown Characteristics in the Presence of Conducting Particles in Liquid Nitrogen", IEEE Transactions on Dielectric and Electrical Insulation, Vol. 9 No. 1, p. 23-30, February 2002

Hayakawa N., Sahakibara H., Goshima H., Hikita M., Okubo H., "Breakdown Mecahnism of Liquid Nitrogen Viewed from Area and Volume Effects", IEEE Transactions on Dielectric and Electrical Insulation, Vol. 4 No. 1, p. 127-134, February 1997

Hernandez-Avila J.L., Bonifaci N. and Denat A. "Hot electron Phenomena in Liquid and Gaseous Ar and N_2 in Divergent Electric Fields", IEEE Transactions on Dielectric and Electrical Insulation Vol. 1, No. 3 p. 412-418, 1994

Hernandez-Avila, J. L., Bonifaci N., Denat A., and Atrazhev V. M., 1994, "Corona discharge inception as a function of pressure in gaseous and liquid nitrogen", IEEE International Symposium on Electrical Insulation, Pittsburgh, PA USA, June 5-8, p. 493

Higuera F. J., 2000, "Electrohydrodynamic flow of a dielectric liquid around a blade electrode", Physics of fluids, Vol. 12, No 11, pp. 2732-2742

Holland H.J., Burger J.F., Boersma N., ter Barke H.J.M. and Rogalla M., "Miniature 10-150mW Linde-Hampson cooler with glass-tube heat exchanger operating with nitrogen", Cryogenics, vol, 38, p.407-410, 1998

Husain E., Mohsin M.M., Naqvi S.R.S., "Insulating materials for super-conductors, their characteristics at cryogenic temperature", 1998 International Conference on Conduction and Breakdown in Solids Dielectrics, Vasteras, Sweden, p361-364, June 22-25 1998

Kadowaki K., Nishimoto S., Kitani I. "Initial Images of Complete Breakdown of Liquid Nitrogen/Polymer Film", IEEE Transactions on Dielectric and Electrical Insulation, Vol. 9 No. 1, p. 48-55, February 2002

Kimura T., Sakai. Y., Tagashira H., Nakamura S., "Fast and Slow Electrons in Liquid Ar and N_2 Mixtures", IEEE Transactions on Dielectric and Electrical Insulation, Vol. 1, No. 4, p. 644, August 1994

Kojevnikov, I. V., Motorin O. V., Bologa M. K. and Kozhukhar, I. A, 2001, "The effect of electrical field parameters, medium properties and interelectrode gap geometry on the EHD pump characteristics", 2001 Annual Report Conference on Electrical Insulation and Dielectric Phenomena

Lacroix, J.C. and Atten, P, 1975, "The influence of induced motion on unipolar charge transport", Proceedings of International Conference on Conduction and Breakdown in Dielectric Liquids, p. 127-130.

Lewis T. J., "Basic Electrical Processes in Dielectric Liquids", IEEE Transactions on Dielectric and Electrical Insulation, Vol. 1, No. 4, p. 630, August 1994

Loveland R. J., Le Comber P. G. and Spear W. E., "Charge Transport in the Diatomic Molecular Solids and Liquids: N_2, O_2 and CO", Physical Review B Vol. 6, No. 8 p. 3121-3127, 1972

Malakhov, A.V., 1999, "The Effect of Time Factor upon the Stability of Output Parameters of Electrohydrodynamic Converters", Proceedings of 13th International Conference on Dielectric Liquids (ICDL '99), Nara Japan, July 20-25

Melcher J. R., 1981, "Continuum Electromechanics," The MIT Press

Murooka Y., Hirashima Y., Kubo M., "Optical studies on hopping-transport mechanism of excess electrons in liquid nitrogen", J Appl. Phys., 53(7), p. 4987-4994, July 1982

Ohyama, R. Watson. A. and Chang J. S., 2000, "Polarity Effect on Electrical Conduction and Electrohydrodynamically Induced Fluid Flow in a AW Type EHD Pump", 2000 Conference on Electrical Insulation and Dielectric Phenomena, p62-64

Ostapemko A. A and Stishkov Y. K., 1999, "Kinematics and dynamics of EHD flows", 1999 Conference on Electrical Insulation and Dielectric Phenomena, p 773-776

Perry R.H. and Chilton C. H., "Chemical Engineer' Handbook", 5th Edition, McGraw Hill, New York, 1973, p. 5.36

Pickard W. F., , "Ion Drag Pumping," Journal of Applied Physics, Vol.34, pp.246, 1963

Ramanan G. and Freeman G.R., “Electron thermalization distances and free ion yield in liquid nitrogen from 77K to near T_c”, J. Chem. Phys, Vol. 87 No. 1, p.319-324, 1 July 1987

Richter A., A. Plettner, K. A. Hofmann, and H. Sandmaier, , “A Micromachined Electrohydrodynamic(EHD) Pump,” Sensors and Actuators, Vol. 29, pp. 159-168, 1991

Schmidt W. F., “Electrons, Holes and Ions in Non-Polar Dielectric Liquids”, Proceedings of 13th International Conference on Dielectric Liquids (ICDL ‘99), Nara, Japan, p. 1-8, July 20-25, 1999

Schmidt W. F., “Liquid State Electronics of Insulating Liquids”, Boca Raton: CRC Press, 1997

Stuetzer O., , "Ion Drag Pressure Generation,” Journal of Applied Physics, Vol.30, No.7, pp.984-994, 1959

Sharbaugh, H. A., Walker, G. W., 1985, “The Design and Evaluation of an Ion-drag Dielectric Pump to Enhance Cooling in a Small Oil-filled Transformer,” IEEE Transactions on Industry Applications, vol. 21, p. 950-5

Takashima T., Hanaoka R., Ishibashi R., Ohtsubo A, 1988, “I-V Characteristics and Liquid Motion in Needle-to-Plane and Razor Blade-to-Plane Configuration in Transformer Oil and Liquid Nitrogen”, IEEE Transactions on Electrical Insulation Vol. 23, No. 4

Takahashi Y. and Ohtsuka K., “Corona discharges and bubbling in liquid nitrogen”, Journal of Physics D: Applied Physics, Vol. 8, p.165-169, 1975

Ueda A., Ohyame R., Watson A and Chang J. S., 2001, “Image Analysis of Internal Fluid Flow in an AW Type EHD Pump”, 2001 Annual Report Conference on Electrical Insulation and Dielectric Phenomena, p512-515.

Werner F. Schmidt, “Electrons in Non-polar Dielectric Liquids”, IEEE Transactions on Electrical Insulation Vol. 26, No. 4, p. 560-567, August 1991

Zhakin, A.I. and Lunev S. A., 1999, “Theory of net-EHD pumping”, Proceedings of 13th International Conference on Dielectric Liquids (ICDL ‘99), Nara Japan, July 20-25

Y. Zhao, P. Foroughi, J. Lawler, and M. Ohadi, “Development of an electrohydrodynamic (EHD) micro pump for LN2 spot cooling”, Proceedings of IECEC'03, November 15–21, 2003, Washington, DC